

Final Performance Report for
Experimental Study and Numerical Modeling
of Gas Flow in Microchannels and Micronozzles
May 2003 to September 2005

Prepared Under
Grant Award No. F49620-03-1-0314

Submitted to
Dr. Thomas Beutner
Program Manager
Aerospace and Materials Sciences Directorate
Air Force Office of Scientific Research
801 North Randolph Street
Arlington, VA 22203
Phone: (703) 696-6961
Fax: (703) 696-8451
E-mail: thomas.beutner@afosr.af.mil

Submitted by
C. X. Lin, Ph.D.
Hemispheric Center for Environmental Technology
Florida International University
10555 West Flagler Street, EC 2100
Miami, FL 33174
Phone: (305) 348-1596
Fax: (305) 348-1852
E-mail: lin@hcet.fiu.edu

Team Members
P. V. Skudarnov, Ph.D.
H. L. Mo, Ph.D.
G. P. Philippidis, Ph.D.

DISTRIBUTION STATEMENT A
Approved for Public Release
Distribution Unlimited

December 2005

REPORT DOCUMENTATION PAGE

AFRL-SR-AR-TR-06-0039

Public reporting burden for this collection of information is estimated to average 1 hour per response, including the time for reviewing instru data needed, and completing and reviewing this collection of information. Send comments regarding this burden estimate or any other as this burden to Department of Defense, Washington Headquarters Services, Directorate for Information Operations and Reports (0704-018 4302. Respondents should be aware that notwithstanding any other provision of law, no person shall be subject to any penalty for failing to valid OMB control number. PLEASE DO NOT RETURN YOUR FORM TO THE ABOVE ADDRESS.

1. REPORT DATE (DD-MM-YYYY)		2. REPORT TYPE		3. DATES COVERED (From - To)	
29-12-2005		final		May 2003 - September 2005	
4. TITLE AND SUBTITLE				5a. CONTRACT NUMBER	
Experimental Study and Numerical Modeling of Gas Flow in Microchannels and Micronozzles				F49620-03-1-0314	
6. AUTHOR(S)				5b. GRANT NUMBER	
Lin, C. X.; Skudarnov, Peter, V.					
7. PERFORMING ORGANIZATION NAME(S) AND ADDRESS(ES)				5c. PROGRAM ELEMENT NUMBER	
Florida International University		11200 SW 8 th Street University Park, Controllers Office Miami, FL 33199		5d. PROJECT NUMBER	
				HCET-2003-M018-001-04	
9. SPONSORING / MONITORING AGENCY NAME(S) AND ADDRESS(ES)				8. PERFORMING ORGANIZATION REPORT NUMBER	
USAF, AFRL AF Office of Scientific Research 4015 Wilson Blvd Room 713 Arlington, VA 22203-1954		NA		10. SPONSOR/MONITOR'S ACRONYM(S)	
				11. SPONSOR/MONITOR'S REPORT NUMBER(S)	
12. DISTRIBUTION / AVAILABILITY STATEMENT					
Approved for public release; distribution is unlimited					
13. SUPPLEMENTARY NOTES					
14. ABSTRACT During the course of this research effort gas flows in microchannels and micronozzles were studied both experimentally and numerically. For the experimental study a flow visualization system was built and used to study gas flows in microscale. Gas velocity measurements in microscale were conducted using both Laser Induced Fluorescence technique in conjunction with Image Correlation Velocimetry and Molecular Tagging Velocimetry technique. For the numerical study three different approaches were utilized. Continuum computational fluid dynamics was first used to study gas flows in microchannels and micronozzles. For micronozzles, effects of geometrical scaling down and different gas propellants were studied. For microchannels, slip versus no-slip boundary condition and compressibility and rarefaction effects were studied. Secondly, Direct simulation Monte Carlo (DSMC) method was used to study low Reynolds number flows in a conical micronozzle. The DSMC simulations were compared with the continuum model and available experimental data, and also used to study propellant gas temperature effect on the generated thrust. Thirdly, a Unified Flow Solver that utilizes hybrid approach using deterministic Boltzmann solver for highly non-equilibrium flows at high Knudsen number and continuum solvers for low Knudsen numbers was tested and demonstrated for gas flows in microscale. Tested cases included gas flows in both microchannels and micronozzles.					
15. SUBJECT TERMS Gas Flow, Microchannels, Micronozzles					
16. SECURITY CLASSIFICATION OF:			17. LIMITATION OF ABSTRACT	18. NUMBER OF PAGES	19a. NAME OF RESPONSIBLE PERSON
a. REPORT	b. ABSTRACT	c. THIS PAGE			19b. TELEPHONE NUMBER (include area code)
				110	

Table of Contents

1.0 Executive Summary	5
1.1 Personnel involved in the research effort.....	7
1.2 Publications stemming from the research effort	8
2.0 Introduction.....	10
3.0 Research Results	12
3.1 Experimental Study.....	12
3.1.1 Experimental Set-up.....	12
3.1.2 Micro Gas LIF System.....	17
3.1.3 Image Correlation Velocimetry	18
3.1.4 Flow Velocity Measurements using ICV technique	23
3.1.2 Molecular Tagging Velocimetry.....	28
3.1.3 Gas Mass Flow Rate Through Micronozzle	32
3.2 Numerical Modeling	34
3.2.1 Modeling of Gas Flows in a DeLaval Nozzle Using Continuum Model.....	34
3.2.2 Modeling of Three-dimensional Compressible Gas Flow in Microchannels Using Continuum Model.....	47
3.2.3 DSMC Simulations of Axisymmetric Gas Flow in Conical Micronozzles	74
3.2.4 Modeling using Unified Flow Solver	81
3.3 Summary and Conclusions	91
4.0 Nomenclature.....	95
5.0 References.....	95
6.0 Appendix.....	101

Acknowledgements

Team members of this project are very grateful to the Air Force Office of Scientific Research (AFOSR) for supporting this work via Grant No. F49620-03-1-0314.

1.0 Executive Summary

The U.S. Air Force is interested in advanced micropropulsion systems for nanosatellite applications. One of the challenging areas in the development of micropropulsion systems is the design of micronozzles. Such micronozzles are needed to generate very small thrusts to enable microsatellites to counteract the disturbances produced by solar pressure, drag, or the distortion in the gravity field as well as to reposition microsatellite instruments according to mission requirements. Thus, both experimental studies and modeling are needed for the successful design of micronozzles.

During the course of this research effort gas flows in microchannels and micronozzles were studied both experimentally and numerically. For the experimental study a flow visualization system was built and used to study gas flows in microscale. Gas velocity measurements in microscale were conducted using both Laser Induced Fluorescence technique (LIF) in conjunction with Image Correlation Velocimetry (ICV) and Molecular Tagging Velocimetry (MTV) technique. Maximum deviation of experimentally measured average velocity via LIF-ICV technique from estimation based on the gas mass flow rate was 12.4%.

Three different approaches were utilized in the numerical study. Continuum computational fluid dynamics was used to study gas flows in microchannels and micronozzles. For flows in micronozzles, effects of geometrical scaling down and different gas propellants were studied. A correlation for specific impulse involving throat diameter and throat Reynolds number was developed. For flows in microchannels, utilization of slip versus no-slip boundary condition, compressibility and rarefaction, and aspect ratio effects were studied. An analytical correlation was developed to predict the

normalized friction factor variation with change in pressure ratio for both incompressible and compressible slip flows. For compressible flow in a microchannel, assumption of the flow to be two dimensional was found to result in prediction of 15% - 45% higher velocities and 7% -12% lower normalized friction factor, than the corresponding three dimensional solution.

Direct simulation Monte Carlo (DSMC) method was used to study low Reynolds number flows in a conical micronozzle. The nozzle exit thrust simulated by DSMC showed good agreement with experimental data from open literature at throat Reynolds number larger than 10, where the flow is in slip regime. For throat Reynolds numbers below 10, the DSMC predicted larger thrust than the experimental data. The DSMC was also used to study propellant gas temperature effect on the generated thrust.

A Unified Flow Solver that utilizes hybrid approach using deterministic Boltzmann solver for highly non-equilibrium flows at high Knudsen number and continuum (Euler or Navier-Stokes) solvers for low Knudsen numbers was tested and demonstrated for gas flows in microscale. Test cases included both microcnannel and micronozzle flows in continuum, slip, transition, and free molecular flow regimes.

Six students were involved in this research effort. The outcome of this involvement was the production of Masters thesis by V. V. Gadepalli entitled "Numerical Simulation Of Gas Flows In A De-Laval Micro Nozzle." Production of a Ph.D. thesis by S. Gokaltun entitled "Particle-based Simulations for Rarefied Gas Flow in Microgeometries" is in progress. The expected outcomes of this thesis are adaptation of Lattice Boltzmann Method (LBM) for gas flows in microscale and development hybrid solver for modeling microscale gas flows that combines DSMC and LBM approaches.

Major conclusions from the thesis by V. V. Gadepalli are as follows: 1. Employed continuum model was able to simulate nozzle exit thrust which is in good agreement with the experimental data except at very low Reynolds number; 2. The model predicted closer values to the experimental data even for the flows in transitional flow regime at the nozzle exit. This indicates the model can also be used for transitional flows; 3. A correlation for specific impulse involving throat diameter and throat Reynolds number was developed as $I_{sp} = 29.54 \cdot Re^{\frac{1}{3}} D_t^{-2.04}$. The correlation can predict I_{sp} with a marginal error up to 10 % of the actual value; 4. In a study of gas propellants it was found that helium proved to be best among nitrogen, argon and carbon dioxide for throat Reynolds number varying from 5 to 2000 for the three throat diameters investigated. Nitrogen followed helium. The performance of argon and carbon dioxide varied depending on the throat diameter and the throat Reynolds number.

1.1 Personnel involved in the research effort

The cumulative lists of people involved in this research effort is shown below.

M.A. Ebadian, Ph.D.

G. P. Philippidis, Ph.D.

C. X. Lin, Ph.D.

P. V. Skudarnov, Ph.D.

H. L. Mo, Ph.D.

W. R. Youngblut, M.S.

L. Schneider

Students

N. Bhosrekar, graduate student (M.S.)
M. Mantrawadi, graduate student (M.S.)
V. V. Gadepalli, graduate student (M.S.)
S. Gokaltun, graduate student (Ph.D.)
A.K. Reyhanogularri, graduate student (Ph.D.)
K. Wilson, undergraduate student

1.2 Publications stemming from the research effort

- Jain, V. and Lin, C.X., "Numerical modeling of three-dimensional compressible gas flow in microchannel," *Journal of Micromechanics and Microengineering*, in press, 2005.
- Gokaltun, S., Skudarnov, P.V., and Lin, C., "Comparative numerical study of gas flow in conical micronozzle by DSMC and continuum methods," *J. Propulsion and Power*, to be submitted for publication, 2006.
- Skudarnov, P.V., and Lin, C., "Gas flow velocity measurements in microchannels and micronozzles," *Experiments in Fluids*, to be submitted for publication (in preparation), 2006.
- Jain, V. and Lin, C., "Numerical modeling of three-dimensional compressible gas flow in microchannels," *44th AIAA Aerospace Sciences Meeting and Exhibit*, accepted for publication, 2006.

- Jain, V. and Lin, C., "Effects of aspect ratio on compressible gas flow in microchannels," 36th AIAA Fluid Dynamics Conference, accepted for publication, 2006.
- Gadepalli, V.V.V. and Lin, C.X., "Navier-Stokes Modeling for Gas Flow in a De-Laval Micronozzle," J. Propulsion and Power, submitted for publication, 2005.
- Mo, H.L., Gadepalli, V.V., Skudarnov, P.V. and Lin C.X., "Continuum Modeling of Gas Flows in Micronozzles," Proceedings of Third International Conference on Microchannels and Minichannels, Paper No. ICMM2005-75043, 2005.
- Mo, H.L., Ye, C.M., Gadepalli, V.V., and Lin, C.X., "Numerical modeling of gas flow in square microchannels," Proceedings of Third International Conference on Microchannels and Minichannels, Paper No. ICMM2005 – 75047, 2005.
- Mo, H.L. and Lin, C.X., "Numerical Study of Axisymmetric Gas Flow in Conical Micronozzles by DSMC and Continuum Methods," 44th AIAA Aerospace Sciences Meeting and Exhibit, accepted for publication, 2005.
- Skudarnov, P.V., and Lin, C.X., "Gas Flow In Microchannels: An Experimental Study," Proceedings of FEDSM2005, 2005 ASME Fluids Engineering Division Summer Meeting and Exhibition, June 19-23, 2005, Houston, TX, USA.
- Gadepalli, V.V.V., "Numerical Simulation Of Gas Flows In A De-Laval Micro Nozzle," M.S. Thesis, Florida International University, 2005.
- Gokaltun, S., "Particle-based Simulations for Rarefied Gas Flow in Microgeometries," Ph.D. Thesis in progress, Florida International University, 2007.

2.0 Introduction

The U.S. Air Force is interested in advanced micropropulsion systems for nanosatellite applications. One of the challenging areas in the development of micropropulsion systems is the design of micronozzles. Such micronozzles are needed to generate very small thrusts to enable microsatellites to counteract the disturbances produced by solar pressure, drag, or the distortion in the gravity field as well as to reposition microsatellite instruments according to mission requirements. Thus, micronozzles should be capable of producing highly accurate impulses or steady-state thrust. Consequently, the design of micronozzles is very important. It has been shown that, in many instances, conventional fluid dynamics approaches are not valid in microscale. The fundamental flow processes in microscale are currently not well understood. Thus, both experimental studies and modeling are needed for the successful design of micronozzles.

The main objectives of this research effort were to develop and demonstrate a flow visualization technique capable of measuring gas flow velocities inside a micronozzle, to characterize flow inside a microchannel and several converging and diverging micronozzles, and to compare experimental flow measurements with the predictions of existing microscale flow models with the aim of validating and improving these models.

For experimental measurements, application of Image Correlation Velocimetry (ICV) technique to velocity measurements in microscale gas flow has been extended. Image correlation velocimetry is a spatial image correlation technique allowing

estimation of the displacement (and consequently velocity) vectors. This technique has been successfully used by Genderich and Koochesfahani (1999) and Fielding et al. (2001) among others, for velocity measurements in conventional scale.

Recently, Ayon et al. (2001) successfully demonstrated the deep reactive ion etching (DRIE) technique for fabrication of silicon supersonic micronozzles. They also tested the thrust performance of several nozzles. However, no detailed measurements of flow field inside or outside the nozzles were performed. For velocity profile measurements of gas jets produced by micronozzles, several velocity measurement techniques have been used, such as laser doppler anemometry (LDA), particle image velocimetry (PIV), molecular tagging velocimetry (MTV) (Lempert et al., 2002), and planar laser-induced fluorescence (PLIF) (Kato et al., 1991).

For velocity profile measurements inside a channel, Meinhart et al. (1999) applied the microscale particle image velocimetry (micro-PIV) technique. The same technique was applied by Wereley et al. (2002) to study flows inside a micronozzle. However, they used liquid to operate the micronozzle because of difficulties in seeding the gas flow. Because of the unavailability of suitable seeding, no PIV measurements in gas flow in a microchannel have been reported to date. MTV has also been used to measure velocity profiles in liquid flows in microchannels (Paul et al., 1998; Maynes and Webb, 2002; Thompson et al., 2002). To the best of the authors' knowledge, the application of ICV to gas flow in microchannels has not been attempted. This technique has the advantage of not requiring seeding particles to operate, and have been demonstrated for microscale flows applications in this report.

From the modeling standpoint, there have been a number of efforts to model fluid flow in microscale. Some of the recent relevant publications include Koplik et al., 1995; Gad-el-Hak, 1998; Beskok and Karniadakis, 1999; and Simek and Hadjiconstantinou, 2001. In summary, microscale flow regimes can be characterized by the Knudsen number (Kn):

- $Kn < 0.001$, continuum flow (the continuum model can be used reasonably);
- $0.001 < Kn < 0.1$, slip flow (the continuum model with slip boundary conditions can be used);
- $0.1 < Kn < 10$, transition flow (Direct Simulation Monte Carlo (DSMC) method can be used); and
- $Kn > 10$, free-molecule flow (DSMC method can be used).

In this report continuum, DSMC, and hybrid solvers were used to check their applicability to various flow regimes and perform parametric studies of gas flow in microscale to understand the physics of such flows.

3.0 Research Results

3.1 Experimental Study

3.1.1 Experimental Set-up

A schematic diagram of a test set-up for studying gas flows in microchannels and micronozzles used in this research effort is shown in Figure 1. The set-up consists of a gas supply cylinder, a mass flow controller, an acetone bubbler, a test cell, manometers, a dump tank, and a vacuum pump. The set-up operates as follows. The test cell is evacuated by the vacuum pump, which is connected to the cell through the dump tank/cold trap, the valve between the pump and the dump tank allows pumping rate regulation. The dump tank/cold trap is used to capture all acetone vapor from the working gas before it

enters the vacuum pump. The working gas is supplied from the gas cylinder, its flow rate is controlled by the mass flow controller. Seeding of the working gas with acetone (for LIF detection) is done in the acetone bubbler. The bubbler is placed into the water bath to allow temperature control and thus acetone concentration control. The bubbler can be bypassed, thus acetone concentration gradients could be introduced in the working gas. The bypass valve is the 3-way solenoid valve, with flow switching frequency controlled by a data acquisition system. Two absolute pressure transducers are monitoring pressure at the test section inlet (microchannel/micronozzle) and inside the test cell. One thermocouple is installed into the acetone bubbler and the other into the dump tank/cold trap for temperature monitoring of these devices. All test set-up instrumentation is connected to a data acquisition system, which facilitates control of the set-up operation and data collection via LabView code developed in house.

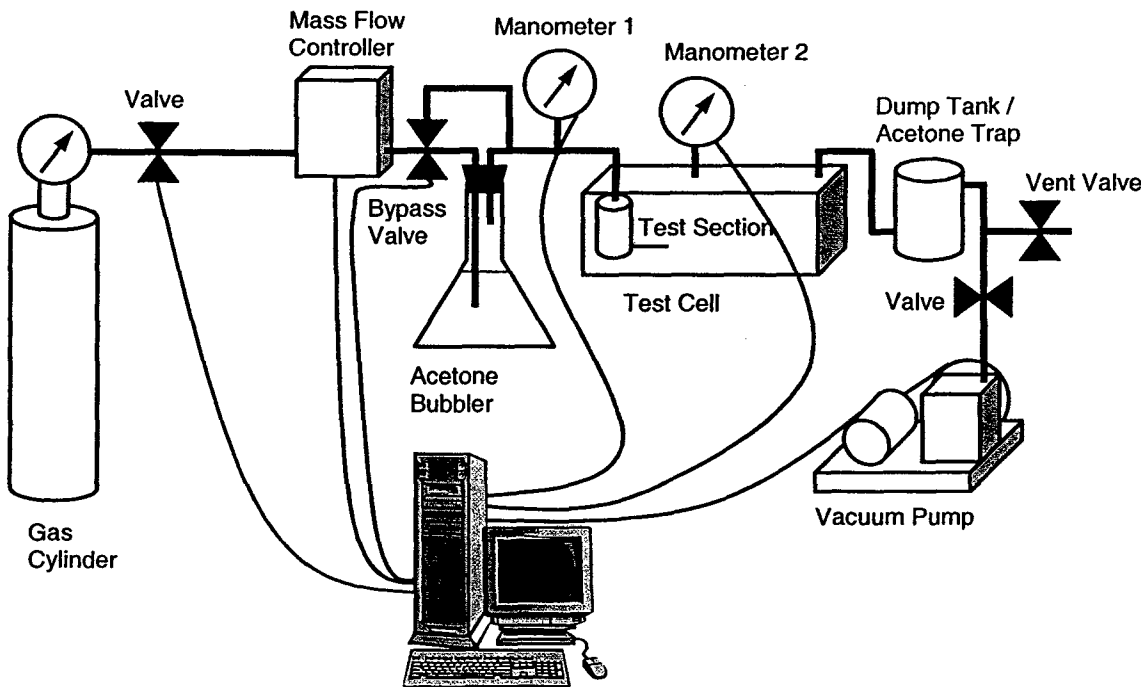


Figure 1. Schematic diagram of the experimental set-up.

The test cell is shown schematically on Figure 2. The test cell consists of the cell and the cover, which were machined out of aluminum alloy. The cover has three ports for gas inlet, pressure monitoring, and vacuum line. The cover is sealed onto the cell with the help of six bolts and an o-ring. The gas inlet port is connected to a cylindrical plenum that provides uniform flow condition at the microchannel inlet. For optical access the cell has three quartz windows, one on the bottom and two on the sides as shown on the photograph in Figure 3.

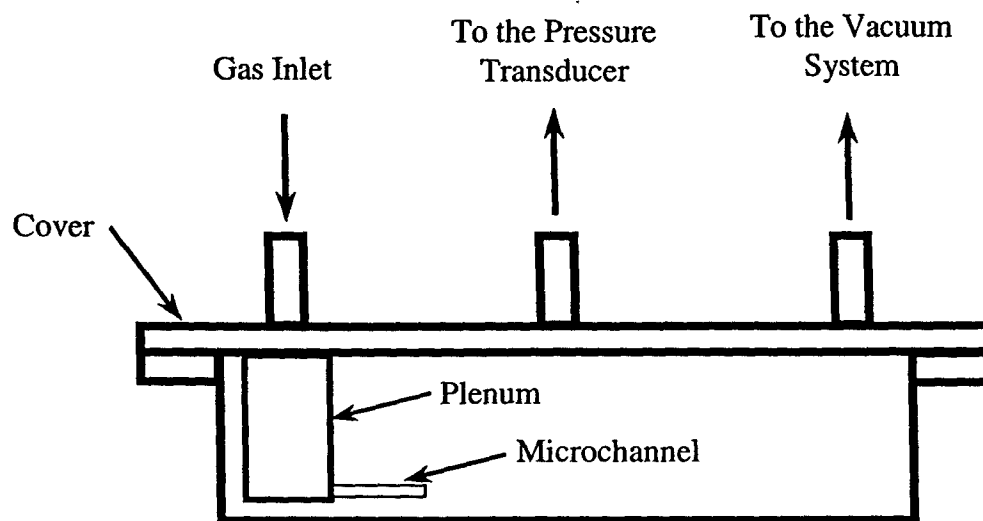


Figure 2. Schematic diagram of the test cell.

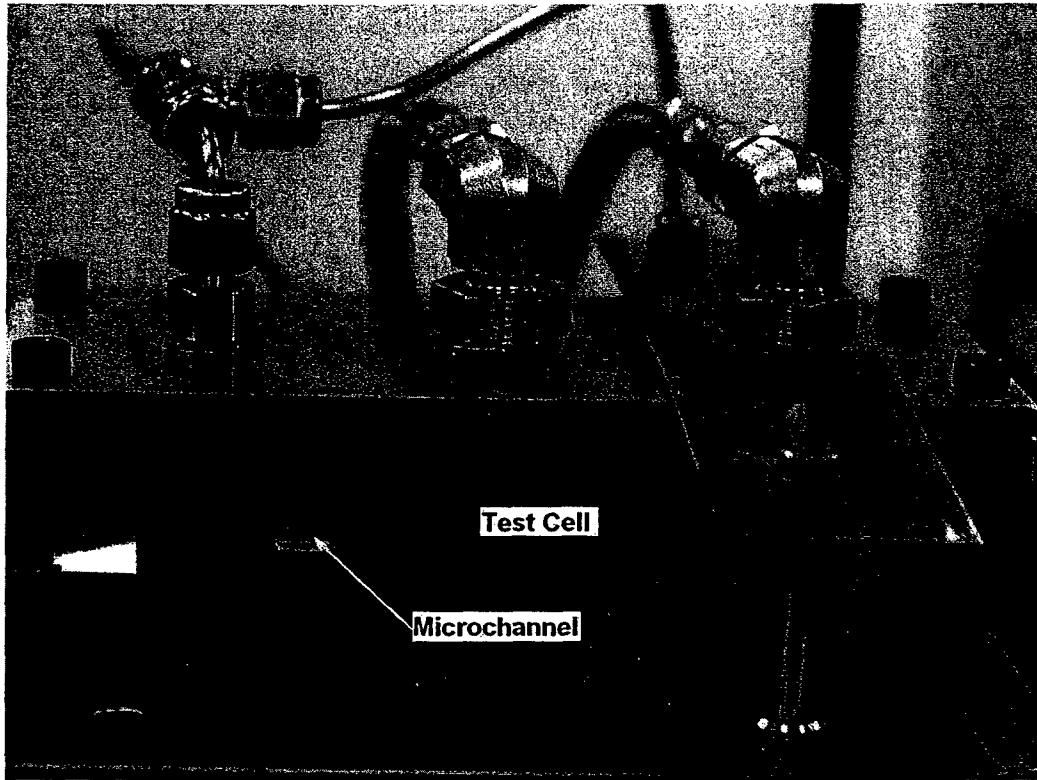


Figure 3. Test cell.

Test apparatus validation was performed by conducting flow tests with pure nitrogen. In these tests the pumping rate was adjusted with the valve between the dump tank and the vacuum pump, and then the gas flow rate was changed with the help of mass flow controller and pressures at the channel inlet and outlet were measured with manometers 1 and 2. Quartz microchannel with square cross section was used in the tests. The inside dimension of the channel is 500 μm , and the length of the channel is 12.7 mm. Reynolds number for conducted tests was in the range of 30 to 300, while Knudsen number was between 1×10^{-3} to 8×10^{-3} .

Measured pressure drops across the channel for different gas flow rates were compared with correlations for laminar flow in rectangular ducts (Shah and London

1978, Shah and Bhatti 1987). This comparison is possible because the flow in the channel is in continuum regime as indicated by low Kn number. Following correlations were used. For fully developed flow in a square duct:

$$f \text{ Re} = 14.227 \quad (1)$$

where $f = \frac{2\tau_w}{\rho U^2}$ is the Fanning friction factor, and Re is the Reynolds number.

The non-dimensional hydrodynamic entrance length for the square duct is $L_{hy}^+ = \frac{L_{hy}/D_h}{\text{Re}} = 0.090$, where D_h is the hydraulic diameter (equal to duct height or width for the square duct). In the entrance section of the square duct:

$$f_{app} \text{ Re} = 18 \quad (2)$$

The pressure drop from duct entrance to exit is:

$$\Delta p = \frac{2\mu U}{D_h^2} (f_{app} \text{ Re} \cdot L_{hy} + f \text{ Re} (L - L_{hy})) \quad (3)$$

where L is the length of the duct.

The comparison between the measurements in the square microchannel and square duct correlations is shown in Figure 4. Two duct hydraulic diameters of 500 μm and 550 μm were used in the correlations. Figure 4 shows that experimental data falls between the curves predicted by correlations. The discrepancy could be attributed to the fact that channel cross section has rounded corners as revealed by studying the channel under a microscope, while correlations were developed for a duct with perfect right angles. Also nonuniformity of the channel cross section along the channel length could

affect apparent hydraulic diameter, the manufacturer specifies channel wall tolerance of $\pm 150 \mu\text{m}$ for this channel with nominal wall thickness of $250 \mu\text{m}$.

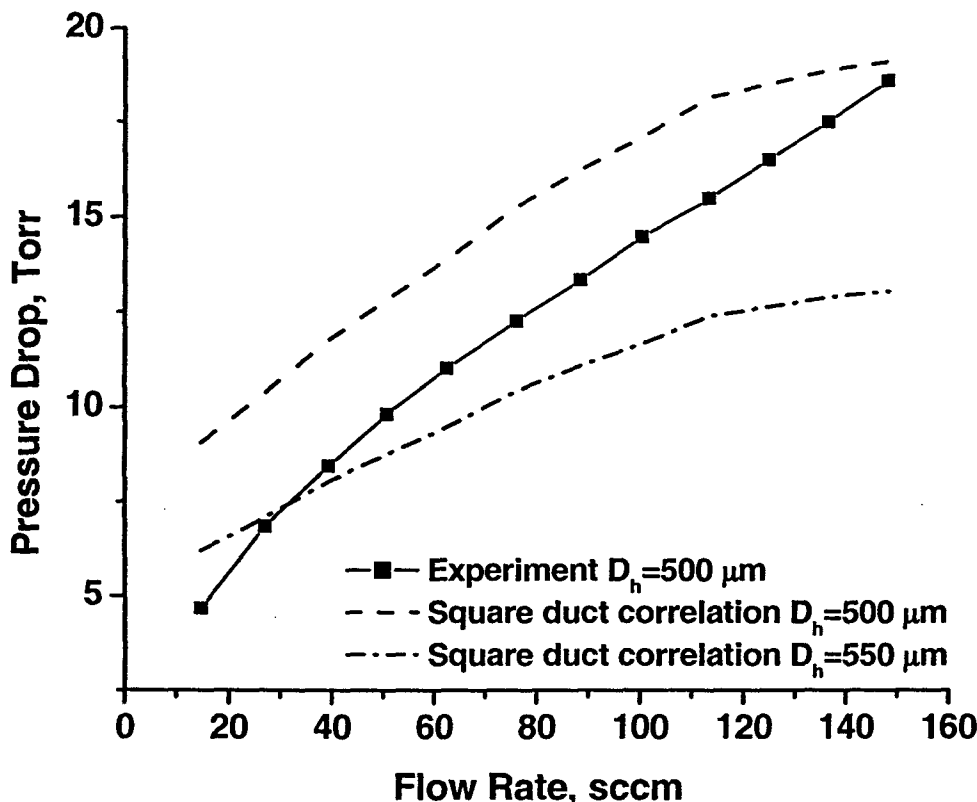


Figure 4. Comparison of experimental data with square duct correlations.

3.1.2 Micro Gas LIF System

Existing micro PIV system was upgraded and modified to enable this system to acquire LIF images in acetone seeded gaseous flows. The Nd:YAG Solo-120 PIV laser was upgraded to have ultraviolet (266 nm) output to allow acetone excitation. Proper filters were installed in the Nikon Eclipse TE2000 microscope to allow acetone fluorescence observation. An image intensifier and a synchronization unit were added to the system to allow LIF image acquisition by the CCD camera. LIF add-on software module was installed on the PC controlling the system to allow LIF image processing.

The diffraction limits of the microscope with 10x and 40x objectives were calculated as ($d = 2.44 \cdot M \frac{\lambda}{2 \cdot NA}$, Meinhart et al. 1999) 12.9 μm and 21.6 μm respectively, which corresponds to the point size projected onto CCD sensor. These point sizes are easily resolvable by our CCD camera with pixel size of 6.45 μm and pitch size of 6.45 μm . When these values are projected back into the flow they correspond to spatial resolution of 1.29 μm and 540 nm for 10x and 40x objectives respectively. When pixel binning is used the spatial resolution is limited by the CCD sensor pixel size. For 2 by 2 binning the spatial resolutions for 10x and 40x objectives are 2.58 μm and 645 nm respectively. For 4 by 4 binning the spatial resolutions are 5.16 μm and 1.29 μm again for 10x and 40x respectively.

3.1.3 Image Correlation Velocimetry

Image correlation velocimetry (ICV) procedure was developed using MatLab. The procedure uses algorithm of Gendrich and Koochesfahani (1996). The developed MatLab script will be used to analyze LIF images acquired by micro gas LIF system. Dantec's software, called Flow Manager, for gas LIF system acquisition and control, provides MatLab link so that custom image analysis procedures can be easily performed using MatLab scripts. The results of such custom image analysis are conveniently stored in the same database with originally acquired images simplifying analysis process and reducing possibility of human errors while working with large number of images.

Image correlation velocimetry is a spatial image correlation technique allowing estimation of the displacement (and consequently velocity) vectors. The fundamental assumptions of this technique are that fluid element travels short distance within short

time interval, and that the information carried by this fluid element is highly preserved. The displacement vector is determined by finding the highest correlation between two regions on two successive images of the flow. The technique works as follows. First, a small window called the source window is selected on the first image. Next, this source window is spatially correlated within a larger window on the second image called the roam window. The roam window is centered on the same location as the source window as shown in Figure 5.

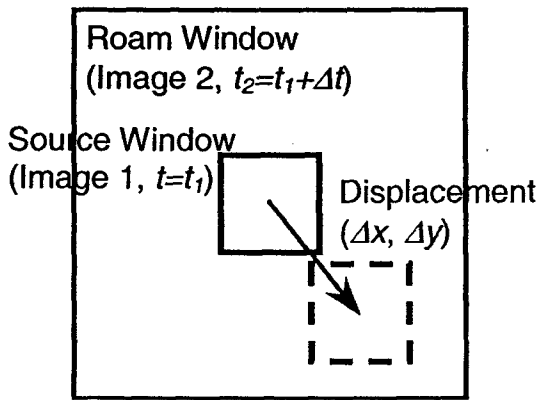


Figure 5. The source and the roam windows of the image correlation velocimetry technique.

Next, a spatial correlation coefficient $C(\Delta x, \Delta y)$ between the source window and all same size windows within the roam window is calculated as a function of the pixel displacement between the windows. The location of the maximum in the correlation coefficient defines the displacement vector with one pixel accuracy. The sub-pixel accuracy could be achieved via two-dimensional polynomial fit of the correlation coefficient function (Zheng and Klewicki, 2000). The equations for the correlation coefficient calculation are as follows:

$$C(\Delta x, \Delta y) = \frac{\overline{I_s I_r} - \bar{I}_s \cdot \bar{I}_r}{\sigma_s \sigma_r} \quad (4)$$

$$\overline{I_s I_r} = \frac{1}{MN} \sum_{i=1}^M \sum_{j=1}^N I_s(i, j) I_r(i + \Delta x, j + \Delta y) \quad (5)$$

$$\overline{I_s} = \frac{1}{MN} \sum_{i=1}^M \sum_{j=1}^N I_s(i, j) \quad (6)$$

$$\overline{I_r} = \frac{1}{MN} \sum_{i=1}^M \sum_{j=1}^N I_r(i + \Delta x, j + \Delta y) \quad (7)$$

$$\sigma_s = \left(\frac{1}{MN} \sum_{i=1}^M \sum_{j=1}^N (I_s(i, j) - \overline{I_s})^2 \right)^{1/2} \quad (8)$$

$$\sigma_r = \left(\frac{1}{MN} \sum_{i=1}^M \sum_{j=1}^N (I_r(i + \Delta x, j + \Delta y) - \overline{I_r})^2 \right)^{1/2} \quad (9)$$

Where I_s and I_r are intensity fields of source window and the displaced window inside the roam window, and $M \times N$ is the size of the source window (usually square window is selected so that $M = N$).

Before the ICV script was used for image analysis of actual microchannel flows it was tested with artificially designed image pairs. The first image in the test pair was an image acquired with our micro LIF system at the exit of the microchannel. The second test image was obtained from the first image by shifting all pixels according to a prescribed parabolic velocity profile. The ICV script was tested by running it with different sizes of the source window, as well as, analyzing image pairs with added random noise.

Figure 6 compares the profile used for shifting pixels on the second image of the test pair with the pixel shift profiles obtained by ICV script. The ICV pixel shift profiles were obtained with different sizes of the source window. It is seen from Figure 2 that for

all used source window sizes pixel shift profiles obtained by ICV script exactly follow the profile used for creating the second image.

Figure 7 shows velocity vector maps for the test image pair with random noise added to the second image. Test images were 8-bit gray scale images with 256 gray levels. Random noise of 5%, 7%, and 10% of 256 gray scale was added to each pixel of the second image. It is seen from Figure 3 that 5% random noise does not significantly affect the vector map with only few vectors detected incorrectly. For 7% noise the effect is much more significant, especially for small pixel shift (low velocity) areas. Finally for 10% noise the vector map is almost completely destroyed, with only small number of vectors detected correctly.

From performed ICV script testing one can conclude that the script works very accurately and even could tolerate up to 5% random noise in an image pair without significant deterioration of the resulting vector map. It was also noted that the effect of adding noise was more pronounced in the areas of small pixel shifts (low velocity).

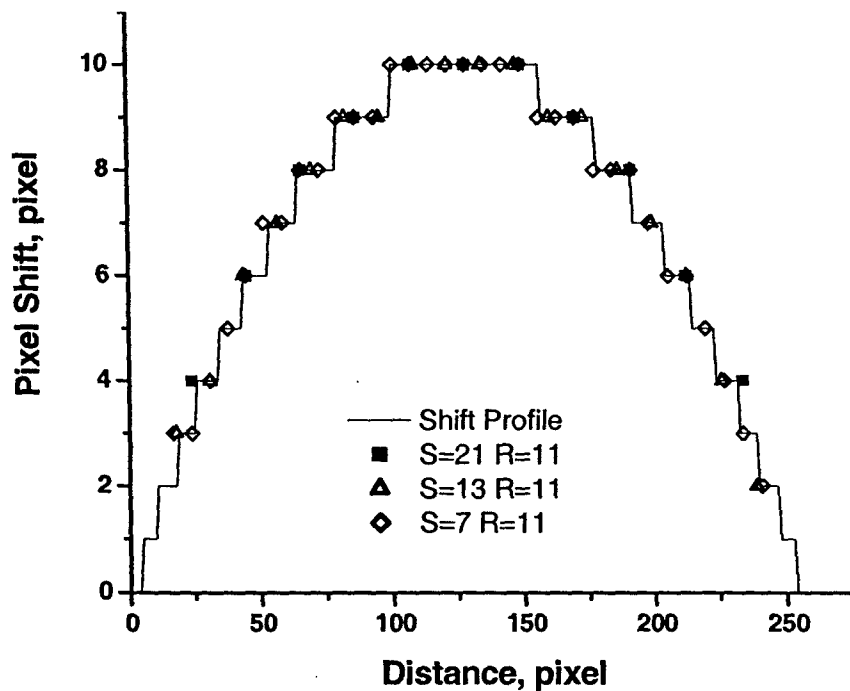


Figure 6. Comparison of the shifting profile with profiles obtained by the ICV script.

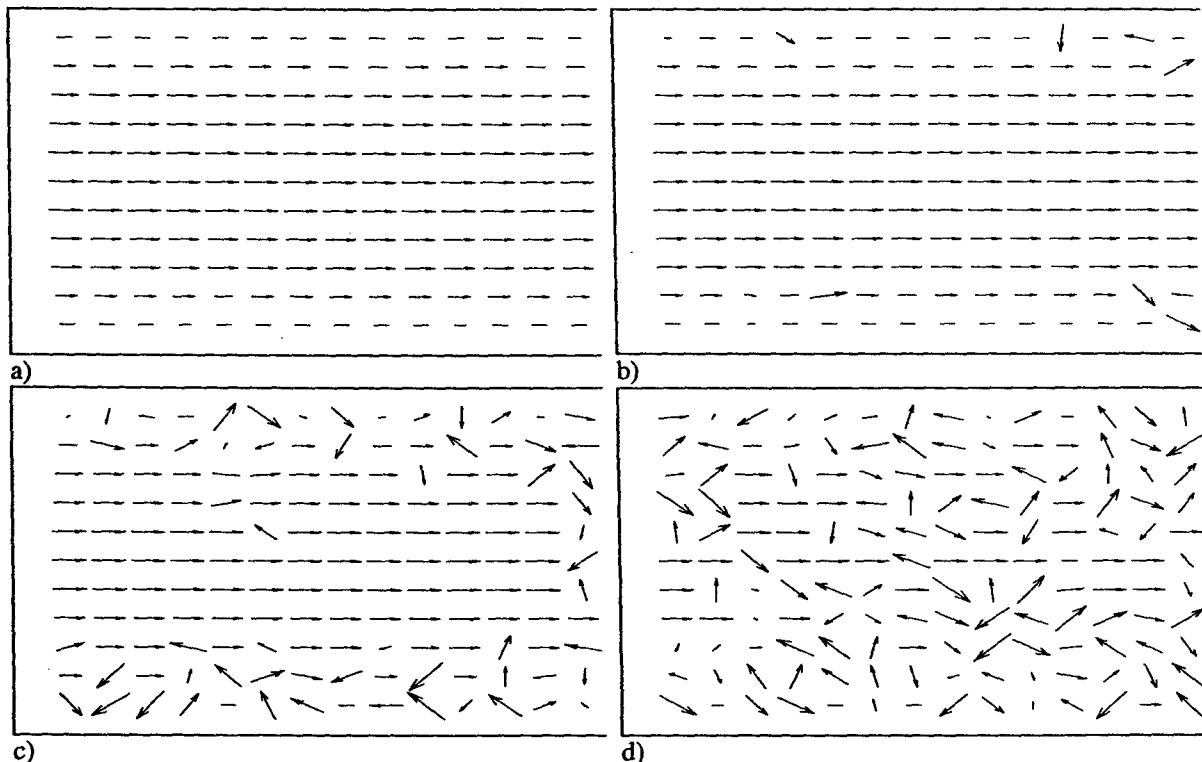


Figure 7. Velocity vector maps for test image pair with random noise added to the second image: a) no noise; b) 5% noise; c) 7% noise; d) 10% noise.

3.1.4 Flow Velocity Measurements using ICV technique

Upon successful testing with artificially designed image pairs, the ICV script was used for velocity field measurements for free jet flow exiting from the microchannel into air under normal room condition (without using the test cell). In order to create acetone concentration gradient for velocity detection by ICV the experimental run started with nitrogen gas flowing through the acetone bubbler. Then the flow was diverted to bypass the bubbler and simultaneously the flow rate of nitrogen was increased to supplement for acetone and keep total flow rate constant. Image acquisition was initiated simultaneously with flow diversion and a number of image pairs were acquired capturing the process of acetone concentration decreasing from its original value to zero. Selected pairs were subsequently analyzed using ICV script. Time interval between the images in one pair was selected based on the gas flow rate and desired displacement. For example, for nitrogen flow of 48 sccm average expected velocity is 2.25 m/s and for the desired displacement of 60 pixel the time interval between the images in the pair should be 35 μ s. Obtained flow fields are shown in Figure 8 to Figure 11. Part a) of each figure shows velocity vectors obtained by ICV superimposed on the LIF signal captured on the first image of the pair. Shown LIF signals are pseudo colored proportional to the strength of the LIF signal and thus acetone concentration. Part b) of each figure shows averaged vector map. On these figures the channel exit is on the left margin of the figure and the gas is flowing from left to right. Shown field of view is 0.825 mm vertically (slightly wider than channel exit width of 0.5 mm) and 1.7 mm horizontally. Time interval between the images in one pair for Figure 8 to Figure 10 was 35 μ s, and for Figure 11 it was 8 μ s. To obtain flow fields on Figure 8 to Figure 11, a square source window of 31

pixel side was used. Since flow direction is known from the experiment, possible source window displacements were searched in the flow direction within rectangular roam window with 61 pixel width. Length of the roam window was selected based on maximum expected displacement based on the flow conditions and time between image frames, those length were 55 pixel, 90 pixel, 135 pixel, and 70 pixel for Figure 8 to Figure 11 respectively. Table 1 summarizes average measured velocities and shows their comparison with estimation based on the set gas mass flow rate.

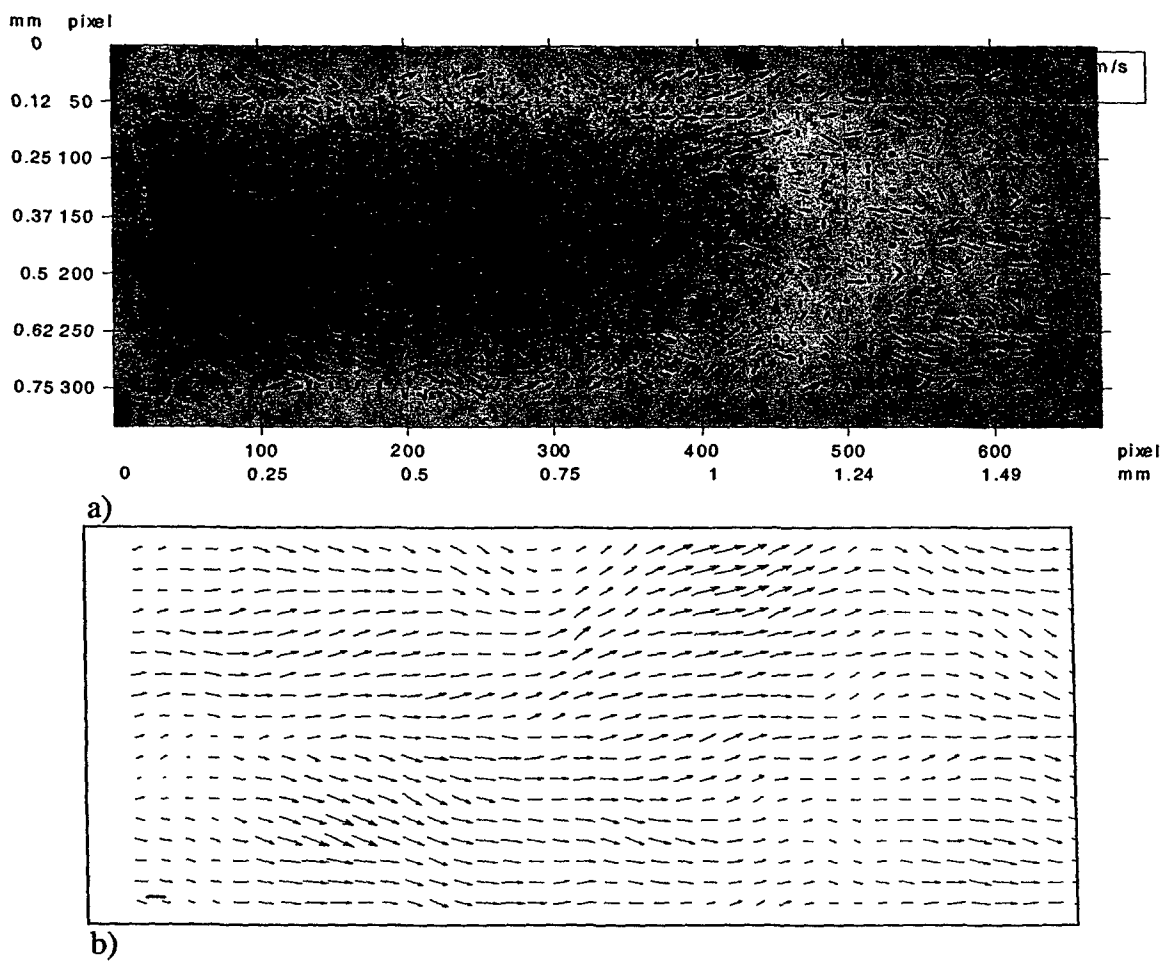


Figure 8. Free jet flow velocity field obtained via ICV processing of acetone LIF images. Expected average velocity 0.75 m/s. a) Color coded acetone LIF image is superimposed on the velocity vector field, b) Averaged vector map.

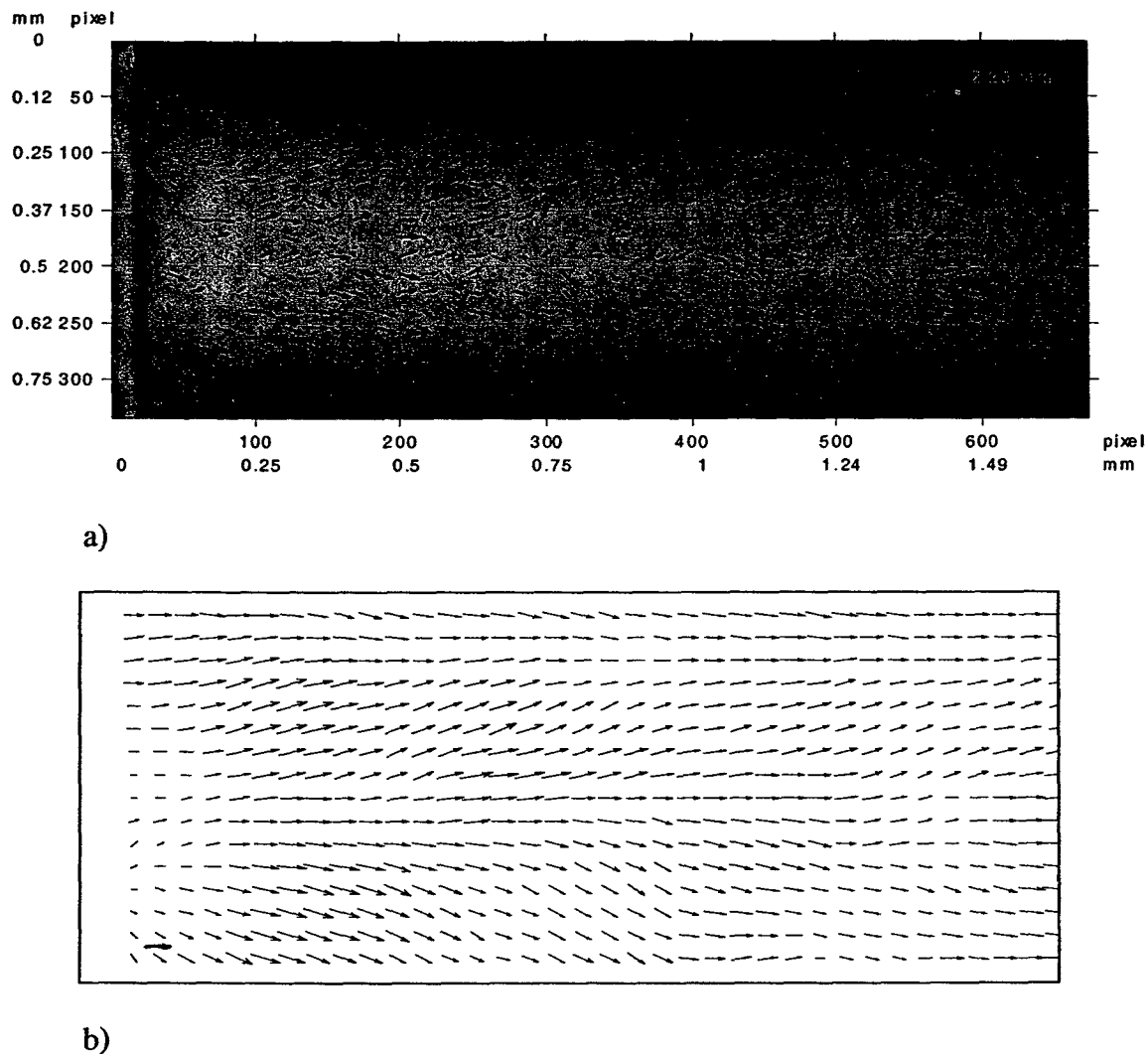
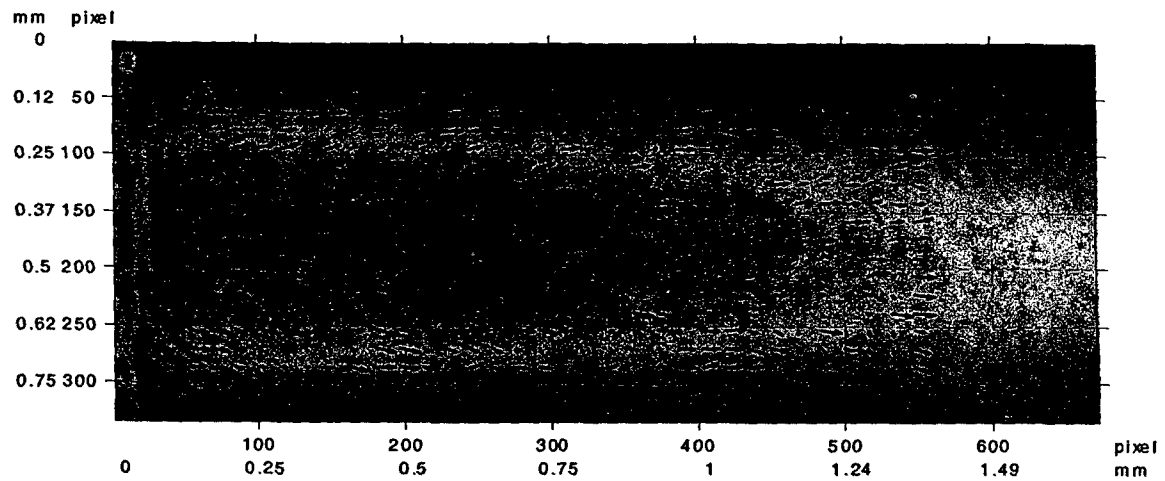
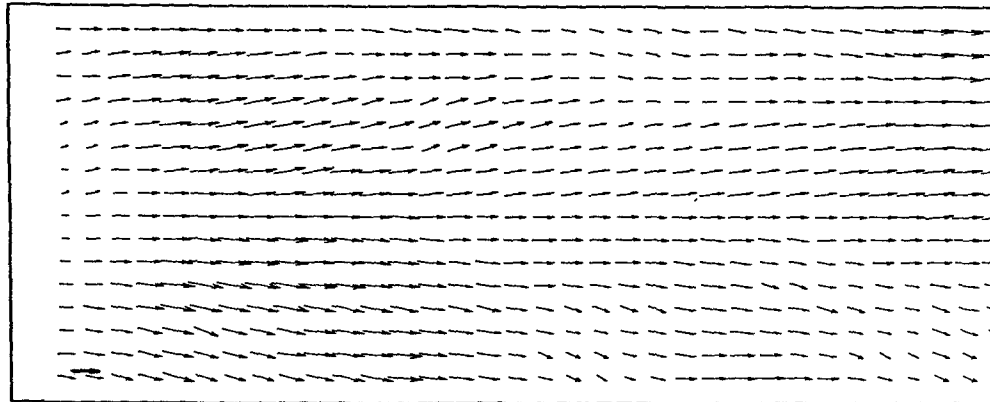


Figure 9. Free jet flow velocity field obtained via ICV processing of acetone LIF images. Expected average velocity 2.25 m/s. a) Color coded acetone LIF image is superimposed on the velocity vector field, b) Averaged vector map.



a)



b)

Figure 10. Free jet flow velocity field obtained via ICV processing of acetone LIF images. Expected average velocity 3.6 m/s. a) Color coded acetone LIF image is superimposed on the velocity vector field, b) Averaged vector map.

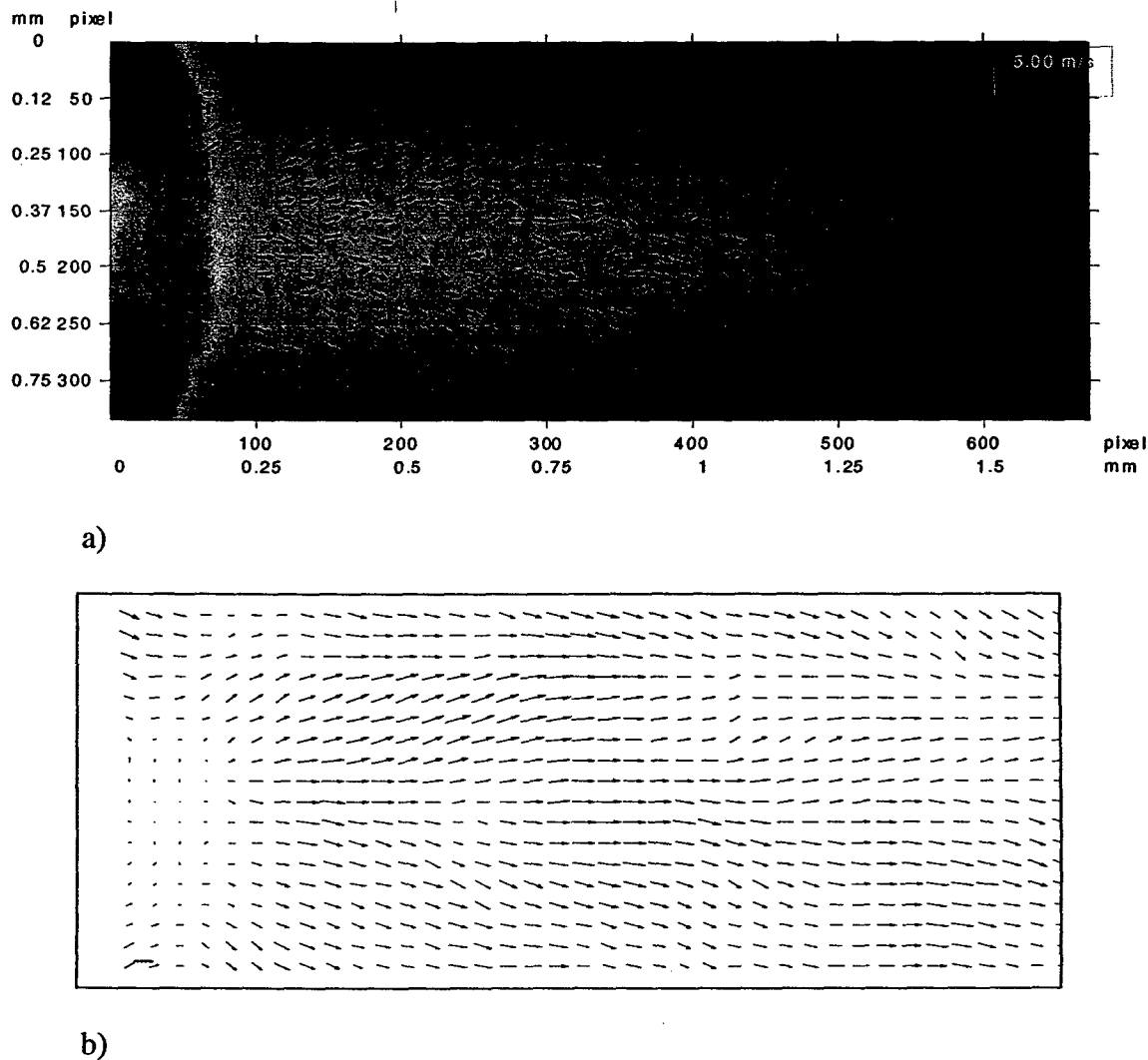


Figure 11. Free jet flow velocity field obtained via ICV processing of acetone LIF images. Expected average velocity 5 m/s. a) Color coded acetone LIF image is superimposed on the velocity vector field, b) Averaged vector map.

Table 1. Comparison of measured flow velocities with estimation based on the set gas mass flow rate.

Gas Mass Flow Rate, sccm	Estimated average velocity, m/s	Measured average velocity, m/s	Percent deviation, %
16	0.75	0.66	12.4
48	2.25	2.05	8.9
77	3.6	3.16	12.2
102	5	4.42	11.6

3.1.2 Molecular Tagging Velocimetry

In addition to velocity measurements by ICV technique, molecular tagging velocimetry (MTV) tests were conducted. For MTV tests following arrangement was used. The laser beam of Nd:YAG laser was narrowed with plano-convex lens from 4 mm diameter down to about 100 μm diameter. The laser was arranged to fire close to the microchannel exit with the beam perpendicular to the flow direction as shown schematically in Figure 12. Nitrogen gas flow was constantly seeded with acetone vapor to produce LIF signal. As illustrated in Figure 12, sets of 30 to 60 images were taken simultaneously with laser shots ($t=t_0$) and with a time delay after the laser shots ($t=t_0+\Delta t$). The displacement of the line written by the laser at $t=t_0$ was determined by comparing the LIF signal profiles in the flow direction on averaged images taken with zero delay and Δt delay. To compare the profiles they were fitted with Gaussian function using least-squares fitting, and the displacement was obtained from the position of the peaks of the obtained fits. Gaussian fitting was selected because it describes laser energy distribution in the beam. Gas velocity was obtained from the measured displacement and a know delay for the images taken after the laser shot.

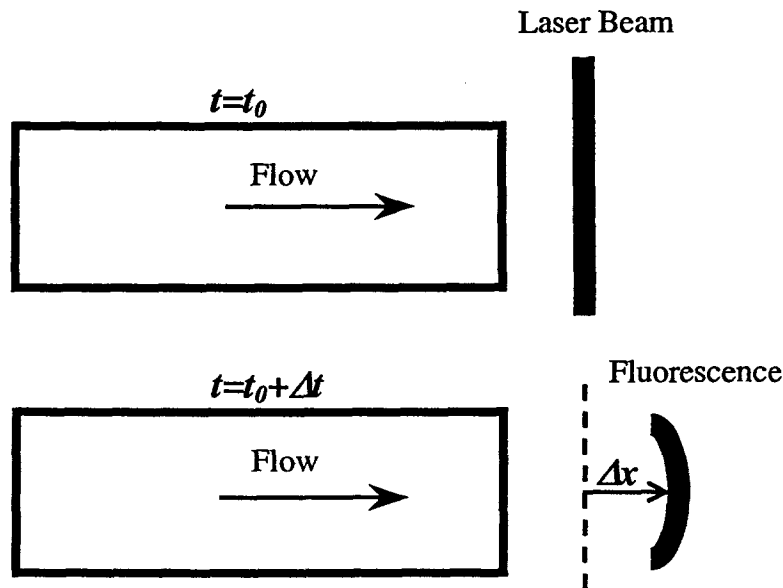


Figure 12. Schematic diagram of molecular tagging velocimetry arrangement.

Typical line written into the flow is shown in Figure 13, on this figure the channel exit is on the left and the flow is from left to right. Image on Figure 13 is taken with zero delay after the laser shot. Typical LIF signal profiles of written line are shown in Figure 14. Two profiles are shown in Figure 14, one with zero delay and the other with 80 ns delay. Both profiles are shown with corresponding least-squares fitting with Gaussian function.

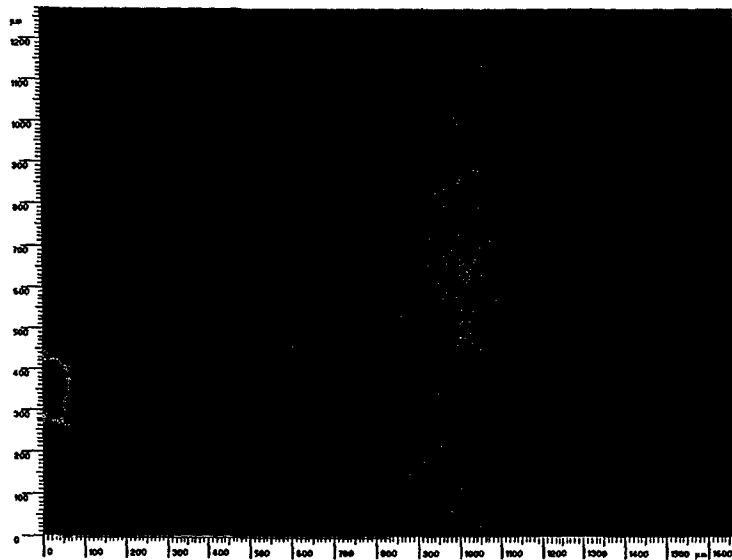


Figure 13. Line written into the flow, image taken with zero delay after the laser shot.

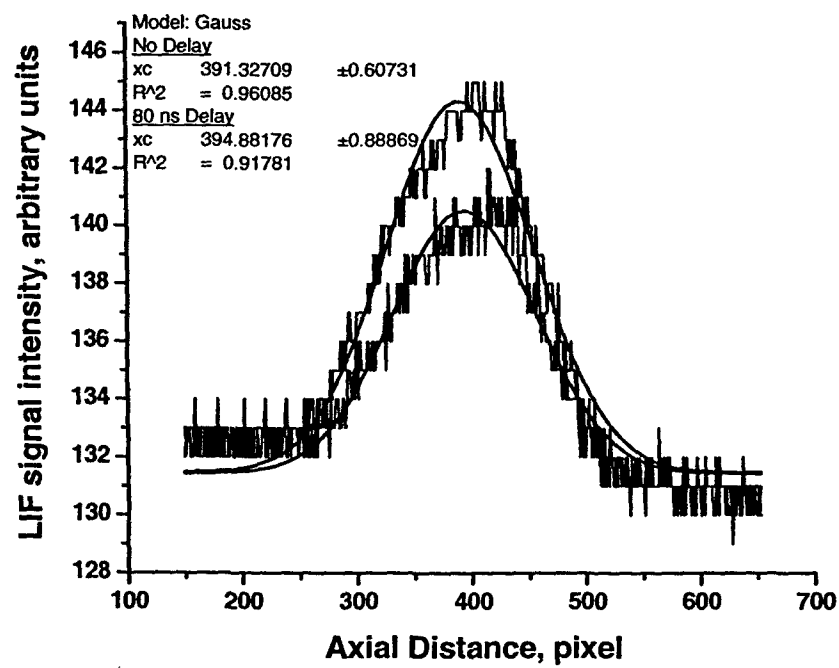


Figure 14. LIF signal profiles with Gaussian fits of the line written into the flow.

A one dimensional velocity profile obtained by MTV technique is shown in Figure 15. This profile was obtained for the microchannel inlet pressure of 92 torr and the pressure

in the test cell of 62 torr (ambient pressure at the exit). Using these conditions and channel dimensions in the solution for volume flow rate for incompressible flow in rectangular duct (White, 1974, eq. (10)) corresponding average flow velocity of 61 m/s was obtained.

$$Q = C \frac{b \cdot a^3}{6 \cdot \mu} \cdot \frac{dP}{L}, \quad C = 1 - \frac{192 \cdot a}{\pi^5 \cdot b} \left(\sum_i \frac{\tanh(i \cdot \pi \cdot \frac{b}{2a})}{i^5} \right) \quad (10)$$

where a and b are channel height and width (in our case of square channel $a = b$).

This estimation compares very favorably with average velocity of 60 m/s from the data in Figure 15.

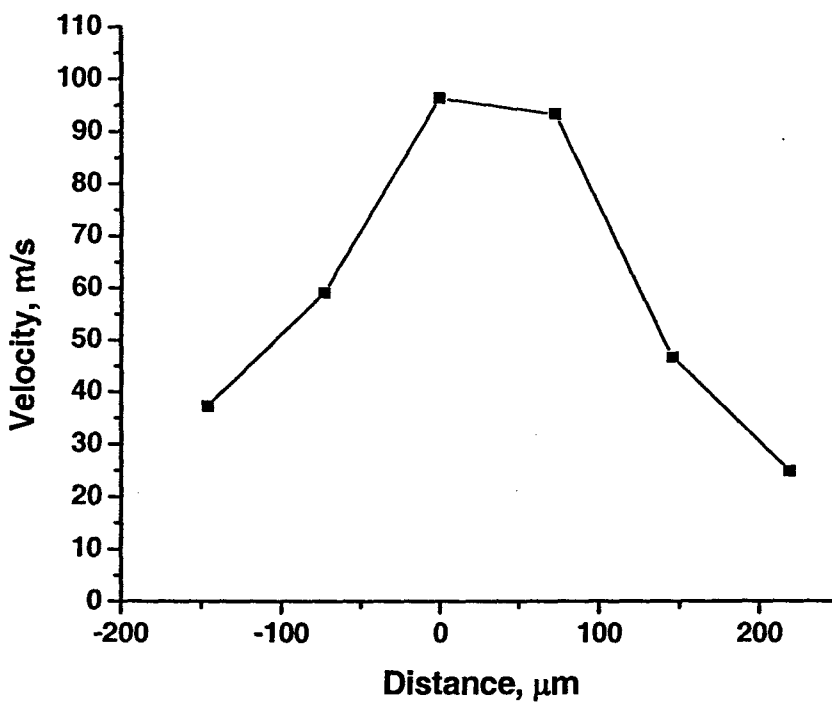


Figure 15. Velocity profile near microchannel exit ($P_{in} = 92$ torr, $P_{amb} = 62$ torr).

Fluorescence intensity of initially written lines as a function of pressure in the test cell is shown in Figure 16. It is seen from the figure that LIF intensity is approximately

linearly dependent on pressure. This approximately linear dependence was previously observed by Lempert et al. (2002) for pressure range up to 9 torr. Our data confirms their result and shows that such linear dependence is observed for pressures up to 100 torr.

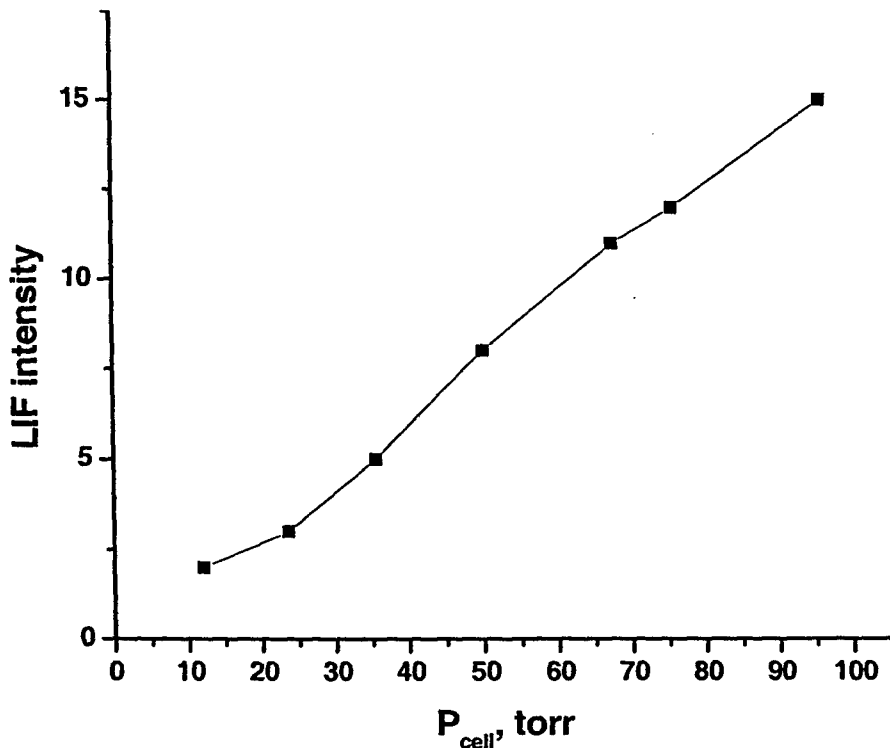


Figure 16. Fluorescence intensity of initially written lines as a function of pressure in the test cell.

3.1.3 Gas Mass Flow Rate Through Micronozzle

Sandwich type design micronozzles with rectangular cross section were obtained from MEMS-exchange manufacturing company. Photograph of one of the manufactured nozzles is shown in Figure 17. The shown micronozzle has throat width of about 100 μm , which is somewhat larger than the design width of 80 μm .

In order to verify the integrity of the micronozzle and gas supply line mass flow test was conducted. A simple set-up was assembled for the purpose of this testing. The

set-up consisted of gas cylinder with regulator, pressure transducer, and mass flow meter on the inlet side of the nozzle and the other mass flow meter on the outlet side of the nozzle. Figure 18 shows measured flow rates before and after the micronozzle as a function of plenum pressure. It is seen from this figure that for pressures up to 40 PSI gas flow rate before and after the micronozzle are the same within the measurement error. Thus, there is no leaks within the micronozzle or in the gas supply line.

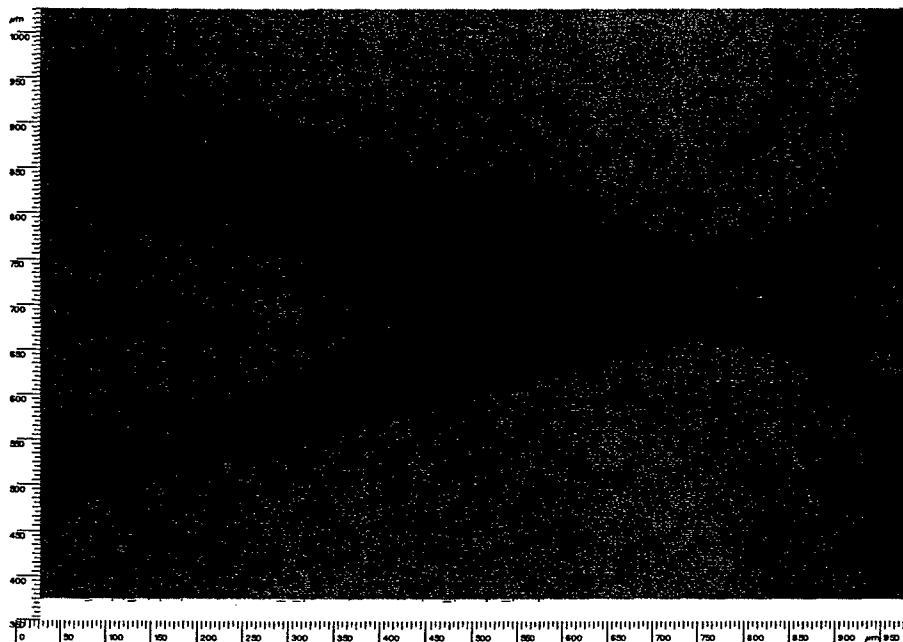


Figure 17. Top view of rectangular cross section sandwich type micronozzle.

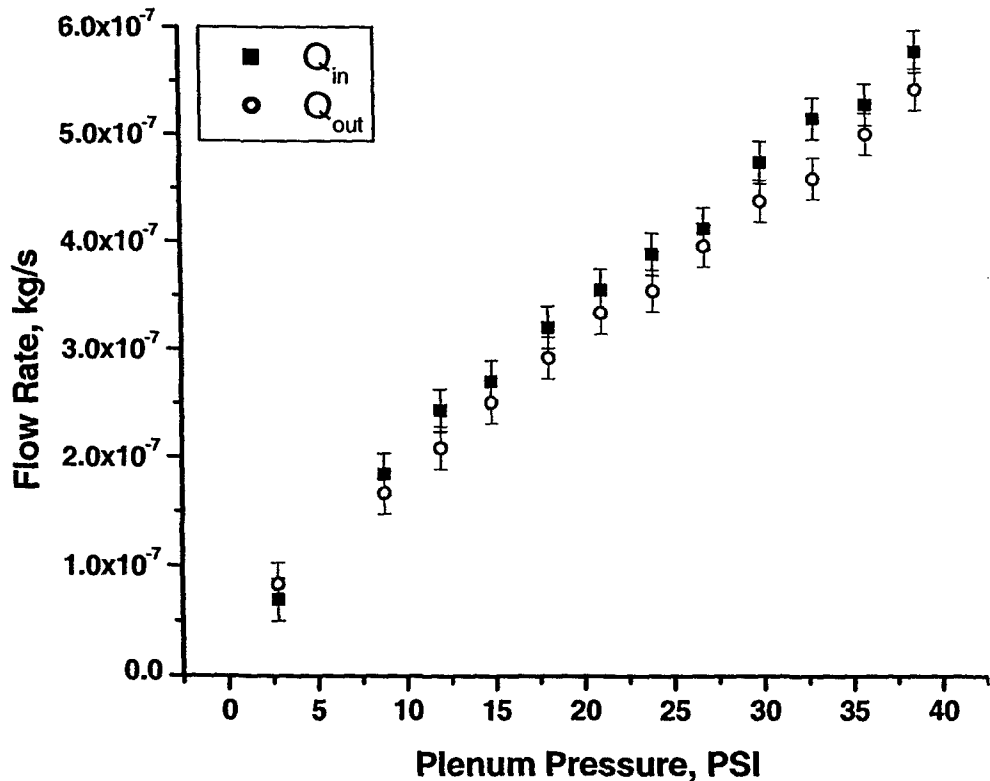


Figure 18. Mass flow measurements for 100 μm throat width micronozzle.

3.2 Numerical Modeling

3.2.1 Modeling of Gas Flows in a DeLaval Nozzle Using Continuum Model

A continuum model based on Navier-Stokes equations was used to investigate gas flows in a DeLaval nozzle. Parametric studies included the effect of geometric scaling via scaling down of throat diameter for various throat Reynolds numbers and the effect of chemical propellants on the integrated performance of the nozzle. A correlation was developed to predict the specific impulse for any given throat diameter and throat Reynolds number. Detailed description of the model, its validation, and parametric study results are presented in following sections.

3.2.1.1 Numerical Model and Its Validation

To perform numerical modeling of gas flows in a DeLaval nozzle 2-D axisymmetric compressible form of Navier-Stokes equations was employed. The governing equations are presented below.

Continuity equation:

$$\frac{\partial}{\partial x}(\rho v_x) + \frac{\partial}{\partial r}(\rho v_r) + \frac{\rho v_r}{r} = 0 \quad (11)$$

Axial and radial momentum equations:

$$\begin{aligned} \frac{1}{r} \frac{\partial}{\partial x} (r \rho v_x v_x) + \frac{1}{r} \frac{\partial}{\partial r} (r \rho v_r v_x) &= - \frac{\partial p}{\partial x} + \frac{1}{r} \frac{\partial}{\partial x} \left[r \mu \left(2 \frac{\partial v_x}{\partial x} - \frac{2}{3} (\nabla \cdot \vec{v}) \right) \right] + \\ \frac{1}{r} \frac{\partial}{\partial r} \left[r \mu \left(\frac{\partial v_x}{\partial r} + \frac{\partial v_r}{\partial x} \right) \right] \end{aligned} \quad (12)$$

$$\begin{aligned} \frac{1}{r} \frac{\partial}{\partial x} (r \rho v_x v_x) + \frac{1}{r} \frac{\partial}{\partial r} (r \rho v_r v_x) &= - \frac{\partial p}{\partial x} + \frac{1}{r} \frac{\partial}{\partial x} \left[r \mu \left(2 \frac{\partial v_x}{\partial x} - \frac{2}{3} (\nabla \cdot \vec{v}) \right) \right] + \\ \frac{1}{r} \frac{\partial}{\partial r} \left[r \mu \left(\frac{\partial v_x}{\partial r} + \frac{\partial v_r}{\partial x} \right) \right] \end{aligned} \quad (13)$$

$$\text{where } \nabla \cdot \vec{v} = \frac{\partial v_x}{\partial x} + \frac{\partial v_r}{\partial r} + \frac{v_r}{r}$$

Energy equation

$$\begin{aligned} \frac{1}{r} \frac{\partial}{\partial r} \left[r \left(\rho C_v T v_r + p_r v_r - v_r \left[2 \mu \frac{\partial v_r}{\partial r} + \frac{2 \mu}{3} \left(\frac{1}{r} \frac{\partial(r v_r)}{\partial r} + \frac{\partial v_x}{\partial x} \right) \right] - v_x \mu \left(\frac{\partial v_x}{\partial r} + \frac{\partial v_r}{\partial x} \right) - k \frac{\partial T}{\partial r} \right) \right] \\ + \frac{\partial}{\partial x} \left[\left(\rho C_v T v_x + p_x v_x - v_x \left[2 \mu \frac{\partial v_x}{\partial x} + \frac{2 \mu}{3} \left(\frac{1}{r} \frac{\partial(r v_r)}{\partial r} + \frac{\partial v_x}{\partial x} \right) \right] - v_r \mu \left(\frac{\partial v_x}{\partial r} + \frac{\partial v_r}{\partial x} \right) - k \frac{\partial T}{\partial x} \right) \right] = 0 \end{aligned} \quad (14)$$

Equation of state

$$\rho = \frac{p}{RT} \quad (15)$$

Experimental work of Jamison et al (2003) was used as the reference problem for model verification and validation. The geometry of the nozzle used in simulations is the same

as that of the nozzle used by Jamison et al (2003). As shown in Figure 19 the nozzle has a throat diameter of 1 mm and an exit diameter of 7.9 mm, which gives an expansion ratio of $\epsilon = 62.41$, the converging and diverging sections of the nozzle have cone angles of 30° and 20° , respectively. The 2D axisymmetric model has been meshed with quadrilateral elements as shown in Figure 20.

In order to ensure accurate solutions of the governing equations, a grid must be sufficiently fine and the results must be independent of grid. A grid independence test was carried out before the actual test cases were run. The numbers of nodes on axial and radial directions was increased to generate different grids. Grid independency is defined as a stage at which, the results remain unchanged with the increase of mesh size. To find the grid independent results, several cases were run at $Re_{throat} = 2.6$ with no-slip conditions. The criterion for the grid independency in the present study was the variation of the mass averaged velocity at the nozzle exit and also the variation of velocity at a point in the throat region.

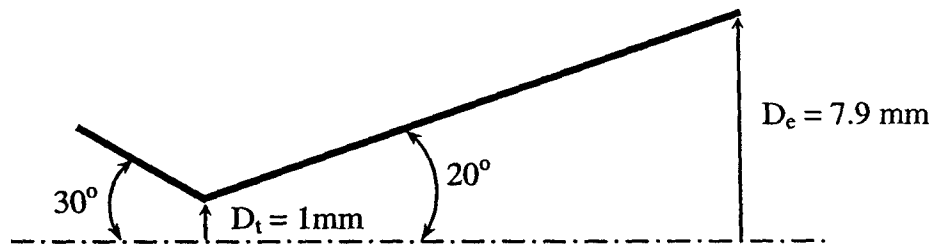


Figure 19. Nozzle geometry.

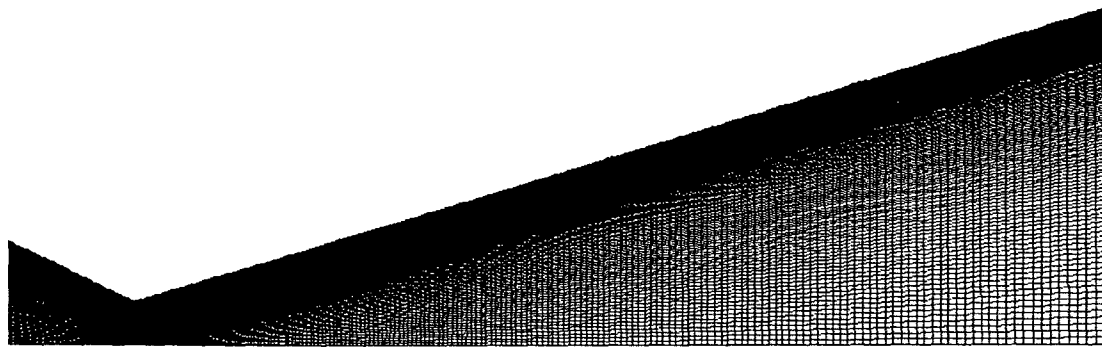


Figure 20. Nozzle grid.

A 240×400 grid was selected as the finest one and used as the reference to calculate the percentage difference of velocity obtained from the grids of 7×12 to 240×400 . Figure 21 shows the grid independence study results, where the left hand scale denotes the velocity (m/s), while the scale on the right hand side represents the percentage of the velocity deviation with the fine grid. It can be observed from Figure 21 that for a 150×250 grid, the percentage deviation in the mass averaged exit velocity with fine grid was about 1.4 % and for the percentage deviation for the velocity at throat, $y = 0.25$ mm was 0.1624 %. The 150×250 grid was selected as the optimum grid for the simulations.

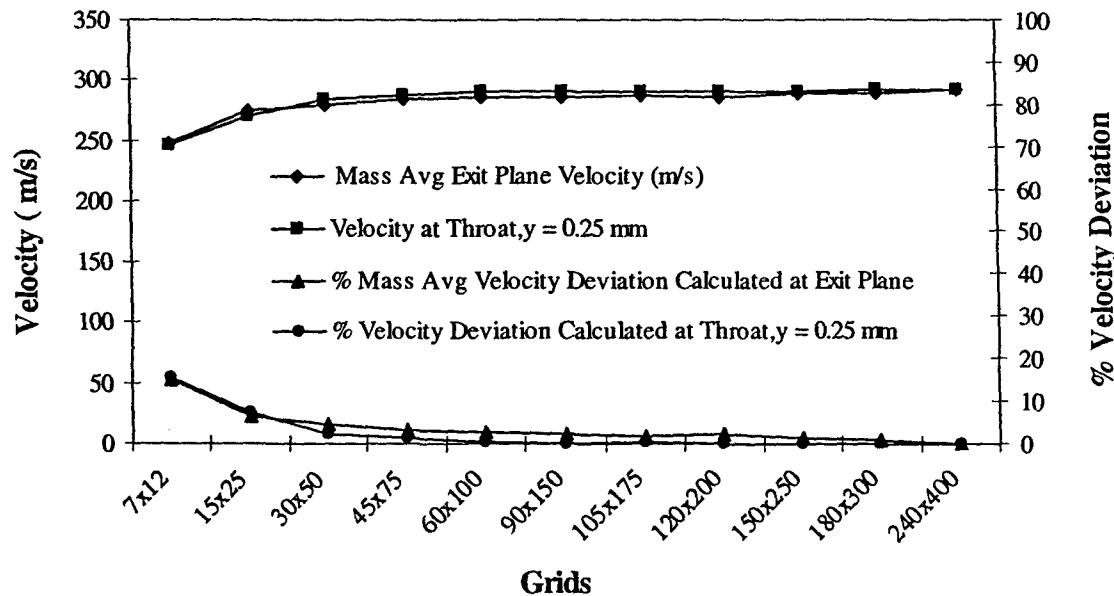


Figure 21. Grid independence study results.

To validate our numerical model we compared the nozzle exit thrust as a function of Reynolds number with experimental measurements of Jamison et al (2003). The nozzle exit thrust is defined as the sum of velocity thrust ($M_e V_e$) and pressure thrust ($P_e A_e$) and is given by the equation (16).

$$T_n = M_e V_e + P_e A_e \quad (16)$$

Comparison of numerical modeling and experimental data are shown in Figure 22. The experimental thrust calculations consisted of velocity thrust, while for the present numerical study, calculations for exit thrust were attempted with and without the pressure component employing both slip and no-slip boundary conditions. It can be observed from Figure 22 that the simulation results of nozzle exit thrust, which included pressure component, are significantly larger than the experimental data at low Reynolds number, and are similar at increasing Reynolds number. A possible reason for the discrepancy at

low Reynolds number could be due to the neglect of maximum backpressures and boundary layer growth.

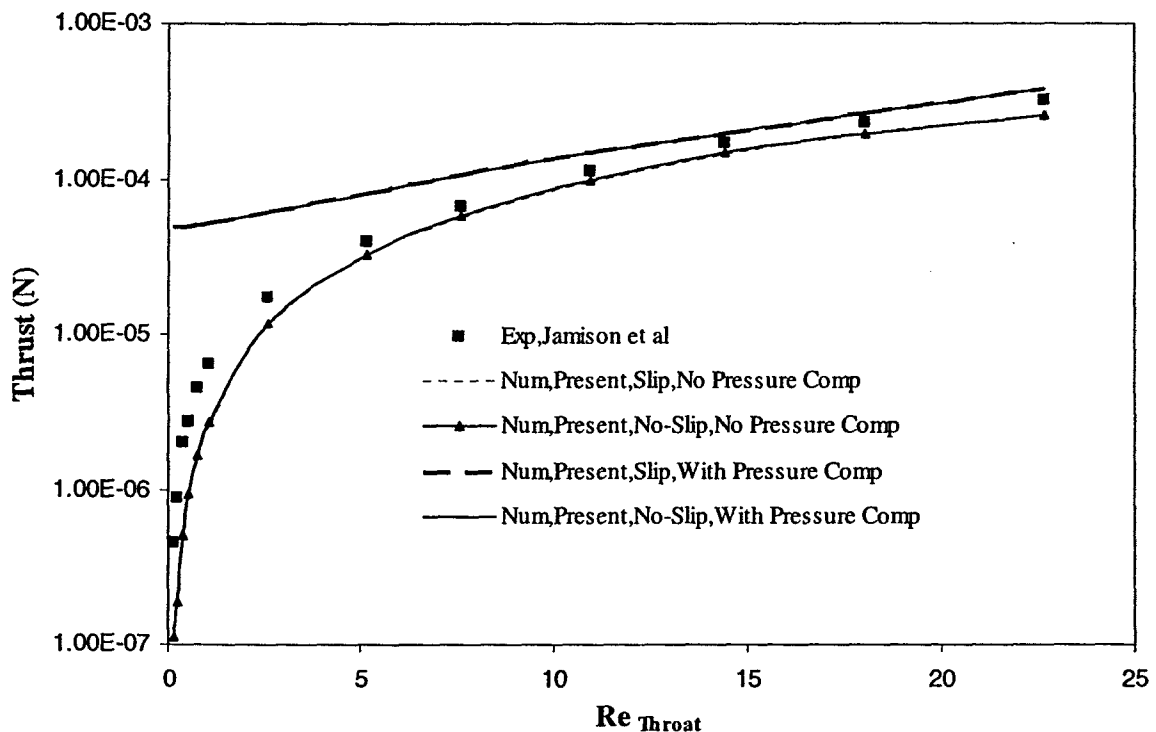


Figure 22. Comparison of the nozzle exit thrust measured experimentally and predicted numerically.

The simulation results for nozzle exit thrust excluding pressure component under predicted the experimental data for both slip and no-slip flows with an error varying from 12 to 19 % for $Re_{throat} = 5.164 \sim 22.692$, which provides reasonable validation of the numerical model. It was observed that the thrust value without pressure component for no-slip flow was slightly higher than that predicted by slip flow model for all $Re_{throat} = 0.164 \sim 22.692$. However, the percentage deviation between the no-slip flow and slip flow was very small between 0.02 to 4.66 % for $Re_{throat} = 0.164 \sim 22.61$. Since the experimental data provided only the thrust measurements, which gives a little information about the physical process taking place inside the nozzle, initial simulations were carried

out with continuum modeling with no-slip boundary conditions. These simulations were used to predict the local Knudsen number, which indicated that the flow was in a transitional regime from inlet to outlet for $Re_{throat} = 0.164$ and 0.219 . For $Re_{throat} = 0.3846$ to 22.692 , the flow is in a slip regime for nozzle inlet, while for the throat, the flow continued to be in a transitional regime until $Re_{throat} = 2.637$ and continued to be in slip regime for $Re_{throat} = 22.692$. In this validation, it was observed that the model predicted close values to the experimental data even though the flow was in transitional regime for certain areas inside the nozzle. This indicates the validity of the model even for the flows in transitional flow regime.

3.2.1.1 Geometric Scaling

Simulations were conducted to study the effect of the geometric scaling of the nozzle on the integrated performance of the nozzle. Figure 23 shows the scaling down of the nozzle schematically. Parametric studies were conducted for the flows ranging for Re_{throat} equal to 5, 20, 50 and 100. In the present research, all the dimensions of the nozzle were scaled in same proportion and in the process, the throat diameter was scaled from 10,000 microns to 10 microns while maintaining same expansion ratio, converging and diverging angles to investigate the effects of nozzle throat diameter with the increase of Re_{throat} .

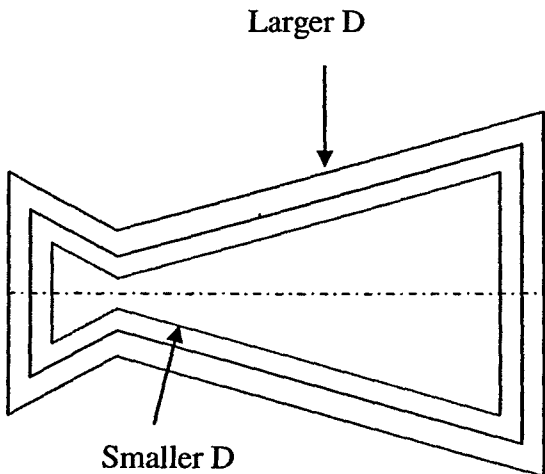


Figure 23. Geometric Scaling of the Nozzle

Figure 24 shows the variation of specific impulse I_{sp} as a function of the throat diameter. It can be observed from the Figure 24, that for each Re_{throat} , with the decrease of D_t , there was one fixed D_t (turning point) beyond which the increase in the value of I_{sp} is relatively small. There is a shift of the turning point with Re_{throat} and was marked with a smooth curve on the figure. This curve divides the entire plot into two zones known as scale sensitive region and scale numb region. The variation of I_{sp} with the decrease of D_t is significantly large in the scale sensitive region, when compared to scale numb region. One possible reason for the turning point shift could be due to the effect of geometric dimension on I_{sp} at low Re_{throat} . This effect subsided with the increase of Re_{throat} .

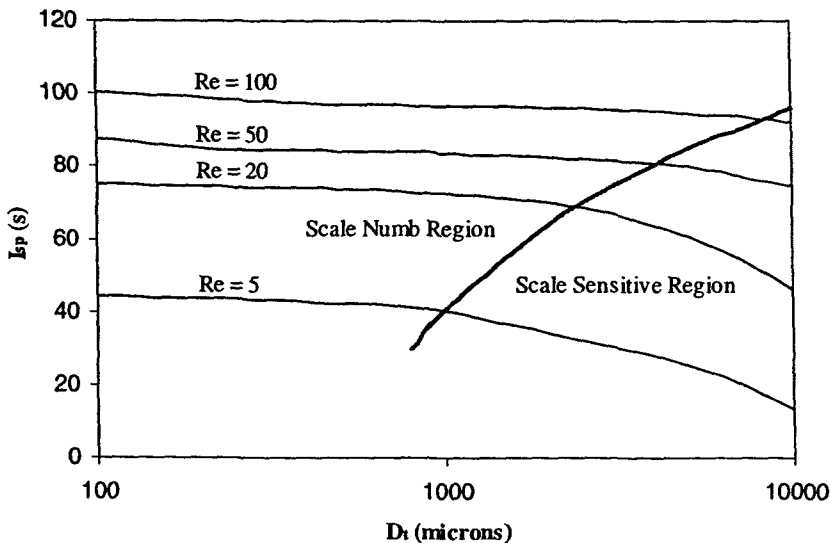


Figure 24. Variation of I_{sp} with D_t for Different Re_{throat} ($Re = Re_{throat}$).

3.2.1.2 Correlation for the specific impulse

A correlation was developed to understand the variation of specific impulse(s) with the variation of throat diameter and throat Reynolds number and is given by the equation:

$$I_{sp} = C \text{ } Re^{\frac{1}{3}} D_t^{-2.04} \quad (17)$$

Where C can be approximated to 29.54. It was observed that I_{sp} is varying in negative power with the throat diameter. Figure 25 shows the correlation plot for various throat diameters and throat Reynolds numbers. Using this correlation, specific impulse of helium propellant can be approximated for any given throat diameter and throat Reynolds number with an average error of 10 %.

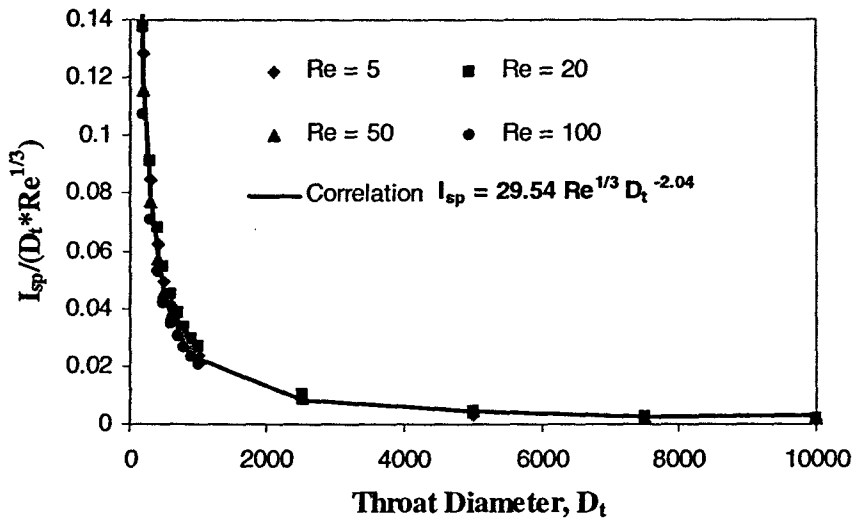


Figure 25. Correlation for the specific impulse ($Re = Re_{throat}$)

3.2.1.3 Effect of Chemical Propellants

Simulations were conducted to study the effect of the chemical propellants on the performance of the nozzles for various throat diameters of 10, 1 and 0.1 mm respectively. These throat diameters were chosen to understand the effect of chemical propulsion system on the dimension of the scale (i.e. micro and macro scale). The propellants were helium, nitrogen, argon and carbon dioxide. One way of measuring the effectiveness of a chemical propulsion system is by calculating the specific impulse of the ejected gas. Mathematically, it can be expressed as

$$I_{sp} = \frac{V_e}{g} \quad (18)$$

The following are the merits for adopting specific impulse for performance evaluation of the nozzle. First, it gives us a quick way to determine the thrust of a rocket, if the mass flow rate through the nozzle is known. Second, it is an indication of engine efficiency. Out of two different rocket engines that have different values of specific impulse, the engine with the higher value of specific impulse is more efficient because it

produces more thrust for the same amount of propellant. The rocket weight will define the required value of thrust. Dividing the thrust required by the specific impulse will tell us how much weight flow of propellants the engine must produce. This information determines the physical size of the engine.

The throat Reynolds number was varied from 5 to 2000 for four different propellants. Figure 26, Figure 27, and Figure 28 show the variation of specific impulse for throat diameters 0.1, 1 and 10 mm respectively. It can be inferred that helium is best propellant, followed by nitrogen, carbon dioxide and argon. It was observed that for throat diameter equal to 0.1 mm, there was not much difference in the value of specific impulse for argon and carbon dioxide when Re_{throat} is below 250. Above $Re_{throat} = 250$, carbon dioxide dominated argon. Similarly for throat diameter equal to 1 mm, up to $Re_{throat} = 250$, there was not much difference between argon and carbon dioxide and above this value carbon dioxide dominated argon. Finally for $D_t = 10$ mm, argon produced higher specific impulse when compared to carbon dioxide up to $Re_{throat} = 400$, beyond which, carbon dioxide generated higher specific impulse than argon. It was also observed that there was no significant increase in the value of I_{sp} when Re_{throat} is greater than 750 for all propellants for the three throat diameters investigated.

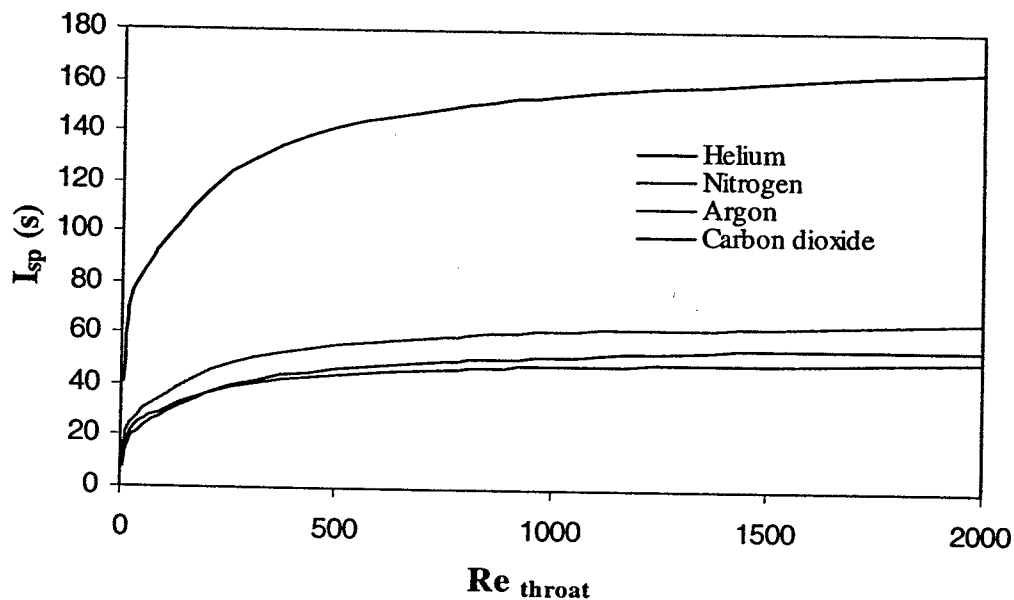


Figure 26. Variation of I_{sp} with Re_{throat} for $D_t = 0.1$ mm.

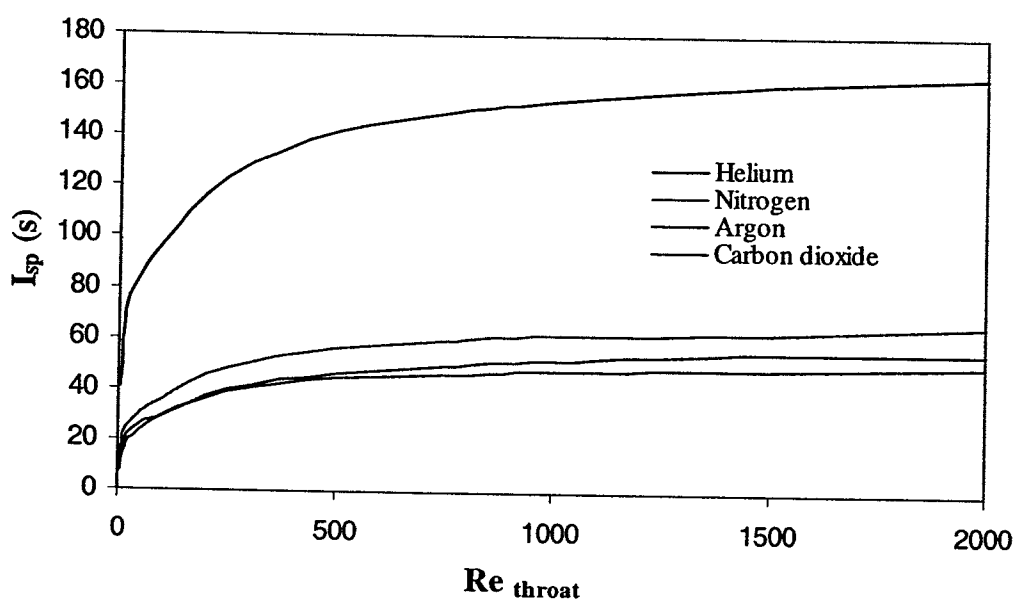


Figure 27. Variation of I_{sp} with Re_{throat} for $D_t = 1$ mm.

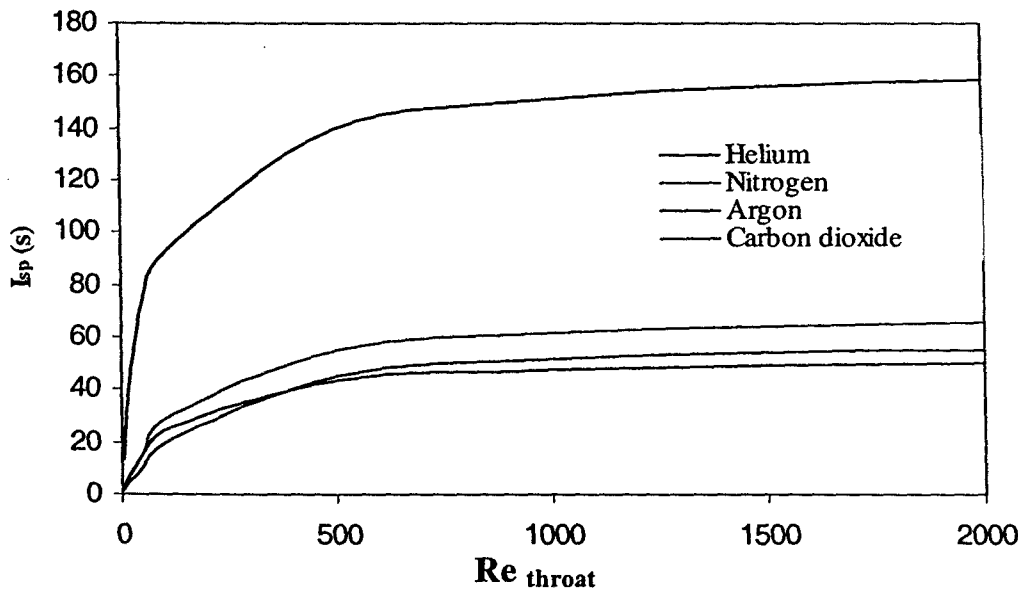


Figure 28. Variation of I_{sp} with Re_{throat} for $D_t = 10 \text{ mm}$.

Specific impulse calculated at $D_t = 10 \text{ mm}$ was smaller for gases like nitrogen, argon and carbon dioxide when compared to specific impulse calculated at $D_t = 1 \text{ mm}$. The results also showed that there was no significant improvement in the value of specific impulse for gases like nitrogen, argon and carbon dioxide when the throat diameter is decreased from 1mm to 0.1 mm.

Simulations were performed at a mass flow rate of $3.09 \times 10^{-7} \text{ kg/s}$ to study the effect of gases on the I_{sp} value. The results are shown in the Table 2. From the table it is very clear that helium dominated, followed by nitrogen. Argon and carbon dioxide predicted specific impulse almost close to each other but argon predicted a little higher value.

Table 2. Specific Impulse at a given mass flow rate of 3.09×10^{-7} kg/s.

Gas	$I_{sp}(s)$
He	72.61
N ₂	25.988
Ar	20.94
CO ₂	20.86

3.2.2 Modeling of Three-dimensional Compressible Gas Flow in Microchannels Using Continuum Model

Nitrogen gas flow in long microchannel with square cross-section was simulated numerically with a three-dimensional continuum model with slip and no-slip boundary conditions. The governing equations of the model were solved by a control volume method. Numerical model was validated with available experimental and numerical results. For incompressible flow, it was found that when D_h was less than 60 μm , slip boundary condition must be applied. Analytical expression for normalized friction coefficients, C_{IC}^* , i.e. ratio of fRe (slip) and fRe (no-slip), was developed on the basis of flow behavior for incompressible flow. For compressible flow, parametric study was conducted for $D_h = 1\mu\text{m}$, $L/D_h = 200$ and with varying pressure ratio (PR = 1.5 – 5.0). It was found that as the pressure ratio increased from 1.5 to 5.0, compressibility effects increased while the rarefaction effects started diminishing. The slip effects also played an important role in the friction characteristics of microchannel flows. Analytical expression for normalized friction coefficients, C_C^* , i.e. ratio of fRe (compressible) and fRe

(incompressible), was developed on the basis of flow behavior for compressible flow. Comparative study of two-dimensional and three-dimensional flow was also conducted and it was shown that two-dimension assumption for the compressible flow was not valid since it gave higher flow velocities, 15% to 45% higher then 3-D and lower friction factor, 7% to 12% lower then 3-D.

Nitrogen gas flow in 3D square microchannel was studied numerically (Figure 29). For incompressible flow, following Chen's (2004) validation model for the three-dimensional steady laminar incompressible flow in microchannel, the channel outlet pressure was maintained at atmospheric pressure with a constant pressure ratio of 1.0001. The channel length over hydraulic diameter ratio was kept as $L/D_h = 1000 \& 200$ with the channel hydraulic diameter varied from $D_h = 200$ to $0.01 \mu\text{m}$. As the pressure ratio was very small, the compressibility effect was negligible. For the compressibility and rarefaction effects study the $L/D_h = 200$, $D_h = 1 \mu\text{m}$ were used. The channel outlet pressure was maintained at atmospheric pressure, with a varying pressure ratio from 1.5 to 5.0, in these high-pressure ratios the compressibility effects were crucial. The inlet was located at $x = 0$. The complete physical model description and fluid properties are tabulated in Table 3.

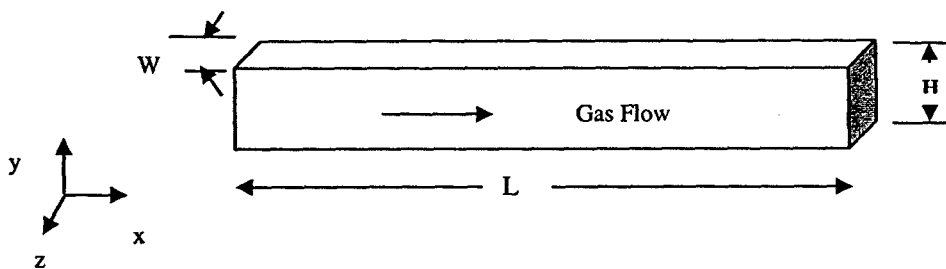


Figure 29. Microchannel geometry.

Table 3. Physical model dimensions and fluid properties.

Parameter	Range or Mean
Working Fluid	Nitrogen
Length, L/D _b	200-1000 μm
Width, W = H	0.01 – 200 μm
Pressure Ratio, PR = P _{in} /P _{out}	1.0001, 1.5 – 5.0
Outlet Pressure, P _{out}	101.325 kPa
Inlet Temperature, T _i	297 K
Wall Temperature, T _w	297 K
Knudsen Number, Kn	0.001 – 0.065
Absolute Viscosity, μ	1.663 x 10 ⁻⁵ Ns/m ²
Specific Gas Constant, R	296.7 J/kg K
Ratio of Specific heat, γ	1.4
Molecular mass	28.013 kg/kmol

The simulated 3-D gas flow and heat transfer is assumed to be steady and laminar. The continuity, momentum and energy equations for the compressible gas flow were expressed as follows:

Continuity

$$\frac{\partial \rho u}{\partial x} + \frac{\partial \rho v}{\partial y} + \frac{\partial \rho w}{\partial z} = 0 \quad (19)$$

Momentum

$$\begin{aligned}
 & u \frac{\partial \rho u}{\partial x} + v \frac{\partial \rho u}{\partial y} + w \frac{\partial \rho u}{\partial z} + \frac{\partial P}{\partial x} - \mu \left\{ \frac{\partial^2 u}{\partial x^2} + \frac{\partial^2 u}{\partial y^2} + \frac{\partial^2 u}{\partial z^2} + \frac{1}{3} \left(\frac{\partial^2 u}{\partial x^2} + \frac{\partial^2 v}{\partial x \partial y} + \frac{\partial^2 w}{\partial x \partial z} \right) \right\} = 0 \\
 & u \frac{\partial \rho v}{\partial x} + v \frac{\partial \rho v}{\partial y} + w \frac{\partial \rho v}{\partial z} + \frac{\partial P}{\partial y} - \mu \left\{ \frac{\partial^2 v}{\partial x^2} + \frac{\partial^2 v}{\partial y^2} + \frac{\partial^2 v}{\partial z^2} + \frac{1}{3} \left(\frac{\partial^2 v}{\partial y^2} + \frac{\partial^2 u}{\partial x \partial y} + \frac{\partial^2 w}{\partial y \partial z} \right) \right\} = 0 \quad (20) \\
 & u \frac{\partial \rho w}{\partial x} + v \frac{\partial \rho w}{\partial y} + w \frac{\partial \rho w}{\partial z} + \frac{\partial P}{\partial z} - \mu \left\{ \frac{\partial^2 w}{\partial x^2} + \frac{\partial^2 w}{\partial y^2} + \frac{\partial^2 w}{\partial z^2} + \frac{1}{3} \left(\frac{\partial^2 w}{\partial z^2} + \frac{\partial^2 u}{\partial x \partial z} + \frac{\partial^2 v}{\partial y \partial z} \right) \right\} = 0
 \end{aligned}$$

Energy

$$\begin{aligned} & \nabla \cdot (\vec{V}(\rho E + p)) - \frac{\partial}{\partial x} \left(k \frac{\partial T}{\partial x} \right) - \frac{\partial}{\partial y} \left(k \frac{\partial T}{\partial y} \right) - \frac{\partial}{\partial z} \left(k \frac{\partial T}{\partial z} \right) \\ & + \frac{2}{3} \mu \left(\frac{\partial u}{\partial x} + \frac{\partial v}{\partial y} + \frac{\partial w}{\partial z} \right)^2 - \mu \left[2 \left(\frac{\partial u}{\partial x} \right)^2 + 2 \left(\frac{\partial v}{\partial y} \right)^2 + 2 \left(\frac{\partial w}{\partial z} \right)^2 \right] - \mu \left[\left(\frac{\partial u}{\partial y} + \frac{\partial v}{\partial x} \right)^2 + \left(\frac{\partial u}{\partial z} + \frac{\partial w}{\partial x} \right)^2 + \left(\frac{\partial v}{\partial z} + \frac{\partial w}{\partial y} \right)^2 \right] = 0 \\ & E = h - \frac{p}{\rho} + \frac{V^2}{2} \end{aligned} \quad (21)$$

Slip Boundary Conditions

$$U_w - U_s = \left(\frac{2 - \alpha_v}{\alpha_v} \right) Kn \frac{\partial U}{\partial n} \quad (22)$$

$$T_w - T_s = 2 \left(\frac{2 - \alpha_r}{\alpha_r} \right) Kn \frac{\partial T}{\partial n} \quad (23)$$

The gas velocity and temperature at slip boundary condition were governed by equations as discussed above. All walls were assumed to be adiabatic at slip and no-slip conditions. For the case where flow was considered incompressible the density term was considered constant. Pressure boundary conditions were used at inlet and outlet boundaries with outlet boundary having atmospheric pressure while static pressure was specified at the inlet.

The governing Navier-Stokes equations were solved with finite volume method. The continuity and momentum equations were solved with second order upwind implicit scheme, and the pressure-velocity coupling with SIMPLEC algorithm. Energy equation was also solved by second order upwind implicit scheme. As the hydraulic diameters of the simulated channels were mostly of the order of 10^{-6} m, the scaled convergence

criterion was set four orders less than the hydraulic diameter for all parameter calculations. The 3-D microchannel was divided into small hexahedral mesh volumes for numerical calculations.

Grid independence study was performed to ensure properly sufficient number of grids had been generated near the walls as shown in Table 4. The grid of size $30 \times 30 \times 600$ was chosen as optimum grid, with further increase of grid size resulting less than 2% increase in average outlet velocity.

Table 4. Grid independence study.

Grid Size	V_{out}	Difference (%)	Grid Size	V_{out}	Difference (%)
$10 \times 10 \times 600$	0.689014	5.90	$30 \times 30 \times 150$	0.7345011	4.5
$20 \times 20 \times 600$	0.7279103	0.80	$30 \times 30 \times 300$	0.7342024	2.3
$30 \times 30 \times 600$	0.7335787	0.60	$30 \times 30 \times 600$	0.7335787	0.1
$40 \times 40 \times 600$	0.7355692	0.40	$30 \times 30 \times 900$	0.73374	0.01
$50 \times 50 \times 600$	0.7364773	0.00	$30 \times 30 \times 1200$	0.73375	0

The numerical technique was validated first with analytical, experimental and numerical results from the literature, then the simulations had been carried out for different hydraulic diameters for incompressible gas flow to study the effects of hydraulic diameter on gas flow properties and then compressibility and rarefaction effects were studied for the compressible gas flow, and finally the 3-D effects were studied.

3.2.2.1 Numerical Technique Validation

To validate the numerical technique, the numerical simulations were done on conventional-size channel (Arkilic et al., 1997). The channel height was fixed at 1 cm. The channel width was varied to obtain different aspect ratios. The channel length was 1000 times the hydraulic diameter. The working fluid was nitrogen. The channel outlet pressure was atmospheric pressure and the pressure ratio, PR, was 1.0001. The friction factor for the flow in conventional size channels was calculated for different aspect ratios and the calculated fRe were compared with the analytical solution and results obtained by Chen (2004) as shown below.

Table 5. Friction factor for conventional size channel

Re	H/W	fRe	fRe	fRe
		(Numerical, Chen (2004))	(Analytical, Chen (2004))	(Numerical, Present)
116	1	57.08	56.91	57.45
212	0.5	62.44	62.19	62.89

Analytical solution for fully developed incompressible laminar channel flow is given below (Chen et al., 1998), the symbols u_m, ρ_m are the average velocity and density over a cross section, respectively.

$$u_m = -\frac{W^2}{12\mu} \frac{dP}{dx} \left[1 - \frac{192}{\pi^5} \left(\frac{W}{H} \right) \sum_{n=1,3,\dots}^{\infty} \frac{1}{n^5} \tanh \left(\frac{n\pi H}{2W} \right) \right] \quad (24)$$

Analytical solutions for mass flow rate Q , friction factor f and Reynolds number Re were calculated using the analytical u_m :

$$Q = \rho u_m A \quad (25)$$

$$f = \left(-\frac{dP}{dx} \right) \frac{2D_h}{\rho u_m^2} \quad (26)$$

$$Re = \frac{\rho u_m D_h}{\mu} \quad (27)$$

$$f Re = \frac{96}{\left(1 + \frac{W}{H}\right)^2} \left[\frac{1}{1 - \frac{192W}{\pi^5 H} \sum_{n=1,3,5,\dots}^{\infty} \frac{\tanh\left(\frac{n\pi H}{2W}\right)}{n^5}} \right] \quad (28)$$

The flow was considered incompressible since the pressure ratio used in the numerical simulations was very small. The numerical simulations were in good agreement with the numerical simulations reported by Chen (2004) and with the analytical results reported by Arkilic et al. (1997). The agreement was within the 1%.

To further validate the numerical model, we simulated compressible microchannel flows and compared the simulated pressure distribution with the available analytical solution and the experimental data (Arkilic et al., 1997). The dimensions of this microchannel were $1.2 \times 40 \times 3000 \text{ } \mu\text{m}$. To comply with the test condition, the channel outlet pressure was fixed at the atmospheric pressure. The pressure ratio was 2.708 with nitrogen as a working fluid. Due to high pressure the flow was considered compressible and the slip effects were also included. The results matched well with the experimental (Arkilic et al., 1997) and numerical (Chen, 2004) results thus validating our numerical technique. In the present simulation the Reynolds number for the flow in Figure 30 was 0.104.

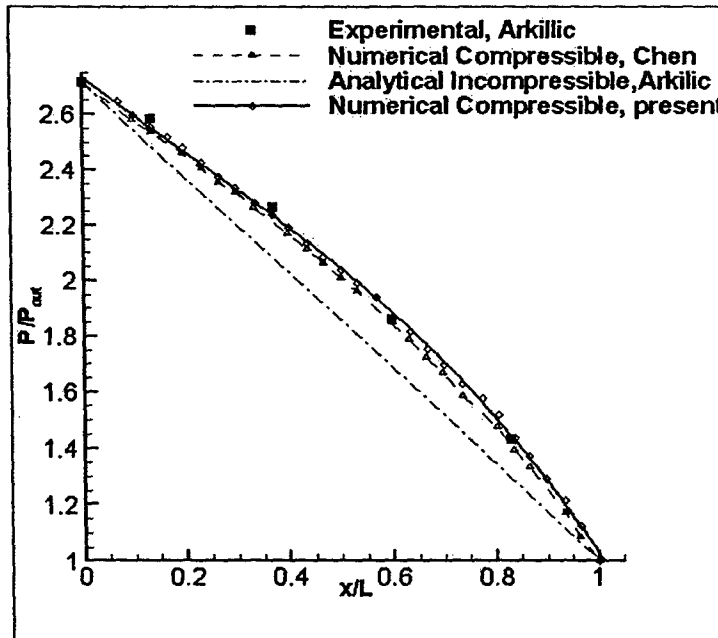


Figure 30. The longitudinal pressure distribution for nitrogen at PR = 2.708.

3.2.2.2 Effect of Geometrical Properties

In the following study of incompressible gas flow in the square microchannel, the geometrical properties like hydraulic diameter and channel length were varied and their effects on flow properties were reported. Hydraulic diameter is equal to height or width of square microchannel. The Pressure Ratio ($PR = P_{in}/P_{out}$) was set to 1.0001. The outlet pressure was fixed as atmospheric pressure.

In our study by Mo et al. (2005), the square microchannel had $L/D_h = 1000$, $PR = 1.0001$. The channel hydraulic diameter was decreased from $D_h = 100$ to $0.01 \mu\text{m}$. We reported simulation results of $fRe = 54.8$, which differed from the analytical solution by 3.85%. We reported that the slight difference could be resulted from the neglect of sidewall effects in the 2-D analytical solutions.

Present results were obtained for square microchannel with $L/D_h = 200$, $PR = 1.0001$. The channel hydraulic diameter in this case was also decreased from $D_h = 100$ to $0.01 \mu\text{m}$ to investigate the effect of L/D_h .

Mo et al. (2005) reported that when the gas flow was in slip regime, the friction factor would be reduced due to the slip flow effect compared with no-slip wall condition, the slip model calculated fRe started to decrease at $D_h = 60 \mu\text{m}$ with the decrease of D_h , where the flow was still in continuum flow regime.

Normalized friction coefficient, $C_{IC}^* = fRe_{\text{Slip}}/fRe_{\text{NoSlip}}$ was calculated for the incompressible gas flow here from Mo et al. (2005). As shown in Figure 31 our results matched well with these results. We can conclude that for the incompressible gas flow reducing the L/D_h from 1000 to 200 had negligible effect on normalized friction coefficient. So to save expensive computational time we could use $L/D_h = 200$ for the developed flow calculation in microchannel. We could also conclude that as the hydraulic diameter increased the effect of slip boundary conditions reduced.

An analytical expression for normalized friction coefficients was developed on the basis of behavior for incompressible flow as shown in Figure 31.

$$C_{IC}^* = \frac{kD_h}{D_h + c} \quad (29)$$

Within the present ranges, the values of constants k and c were, $k \sim 54.6 \pm 0.5$ and $c \sim 0.6 \pm 0.05$.

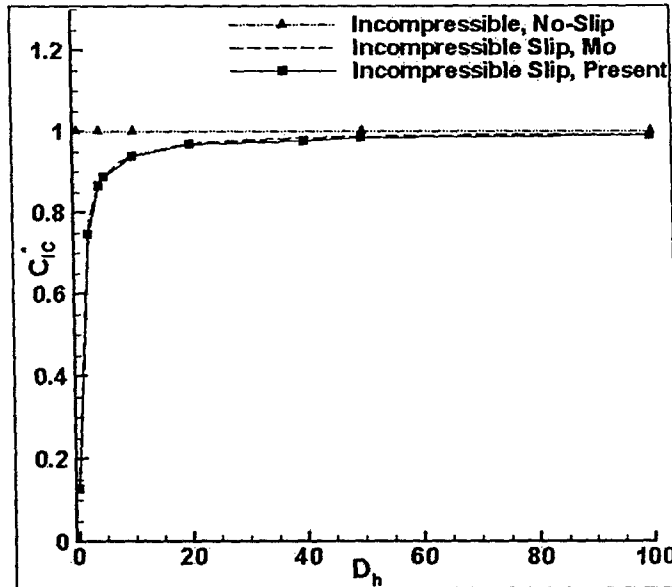


Figure 31. C^*_{IC} versus hydraulic diameter, $C^*_{IC} = fRe_{slip}/fRe_{noslip}$.

3.2.2.3 Compressibility and Rarefaction Effects

To study the compressibility effects for slip and no-slip boundary conditions on the three-dimensional microchannel flows, we simulated flow in square microchannel with flow conditions specified in Table 3. The channel outlet pressure was fixed at atmospheric pressure. The inlet pressure ratio was varied from 1.5 to 5.0.

The pressure drop in the channel takes place in order to overcome the frictional forces along the walls. The effect of slip and no-slip boundary conditions on the pressure variation (P/P_{out} is the ratio of local pressure to outlet pressure) along the centerline of the channel is shown in Figure 32 for compressible flow. It could be observed that with the increase in pressure ratio the divergence in the pressure distribution between slip and no-slip wall condition increases. The maximum percent difference in the pressure distribution between two wall condition was almost 6% at PR = 5.0. Linear pressure distribution for incompressible no-slip flow is also shown for comparison in Figure 32.

As shown in Figure 32, when the pressure ratio was small, $PR = 1.5$, the compressibility effect was small, and pressure distribution was almost linear for all the flow conditions. But when the pressure ratio became higher, the pressure distribution became highly non-linear due to the compressibility effects. So we could conclude that the nonlinearity of the pressure distribution and corresponding compressibility effect increased with the increasing pressure ratio for 3-D flow conditions. As observed in Figure 32, the pressure distribution for the no-slip was more non-linear when compared to the slip flow. The reason could be that the slip flow reduced the wall friction and therefore diminishes the non-linearity of the pressure distribution compared to no-slip flow.

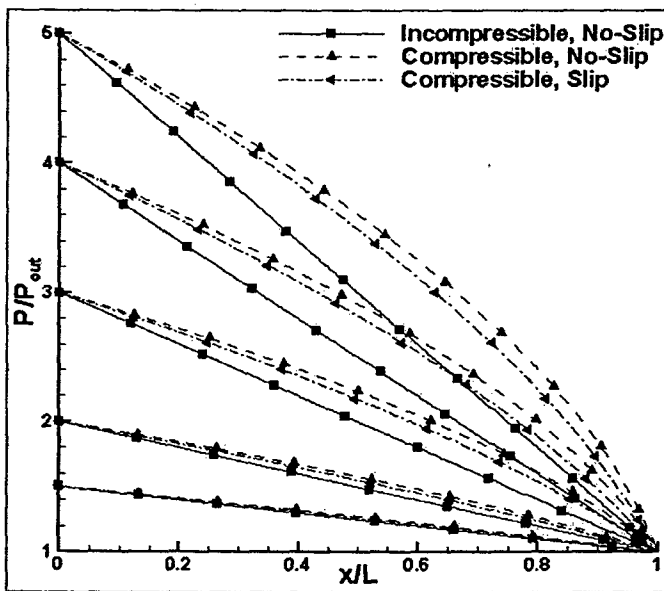


Figure 32. The longitudinal pressure distribution at various pressure ratios.

As the pressure ratio ($PR = P_{in}/P_{out}$) increases the mass flow rate increases nonlinearly for compressible slip and no-slip gas flows while it increases linearly for incompressible no-slip simulations as shown in Figure 33. This is because as the pressure

ratio increases the compressibility effect becomes more dominant and thus affects the mass flow rate more substantially. As observed in the Figure 33, the mass flow rate was higher with the slip boundary conditions than with the no-slip boundary conditions. This was the result of the lower friction resistance in the microchannel.

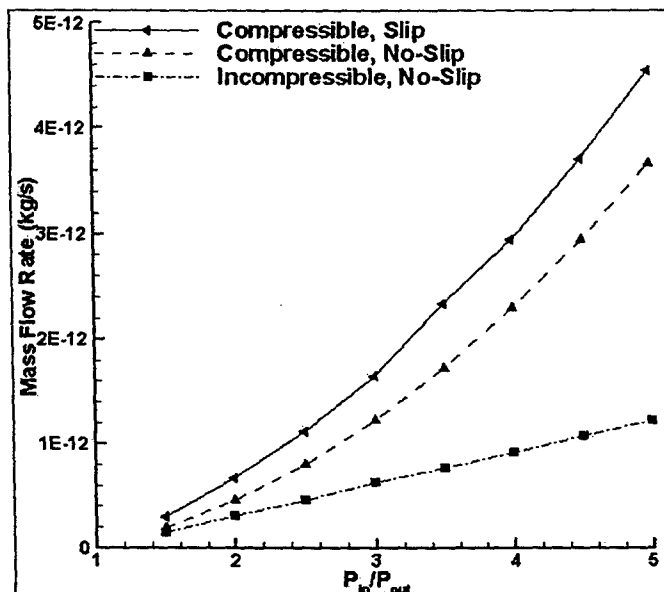


Figure 33. Mass flow rates at various pressure ratios.

Since for compressible gas flow the density decreases from inlet to outlet and Knudsen number varies inversely with density. Therefore the Knudsen number of a microchannel flow increases along the longitudinal axis and reaches the maximum at the outlet as shown in Figure 34. Figure 34 shows the local Knudsen number variation from inlet to outlet for two pressure ratios for compressible flow. The behavior was similar for all other pressure ratios. The Knudsen number variation from inlet to outlet for incompressible gas flow was very minimal and thus can be assumed to be constant. Figure 35 shows the Knudsen number behavior with increasing pressure ratio. The mass

weighted average Knudsen number was calculated for microchannel at each pressure ratio. It could be seen that with the increasing pressure ratios the average Knudsen number was reducing for the compressible case while for the incompressible case it was almost constant. The difference between the average Knudsen number for slip and that for no-slip compressible flow was negligible. It could be observed that as the pressure ratio increased from 1.5 to 5.0 the average Knudsen number was almost in the no-slip regime, $\text{Kn} = 0.012$.

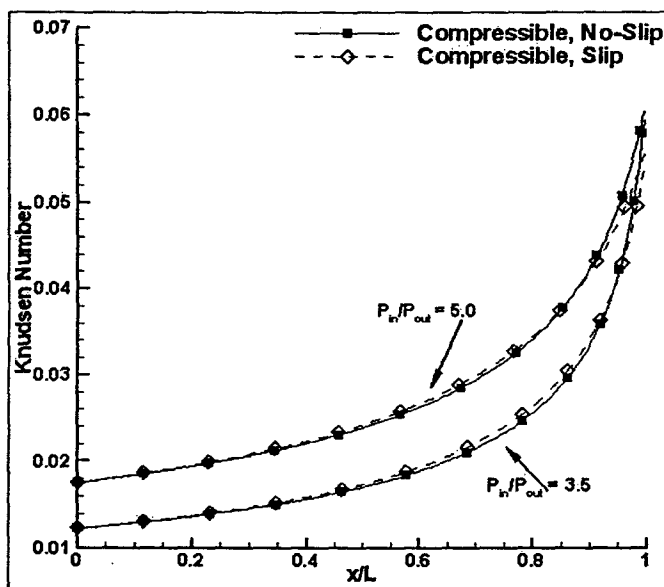


Figure 34. Local Knudsen number variation along the channel length.

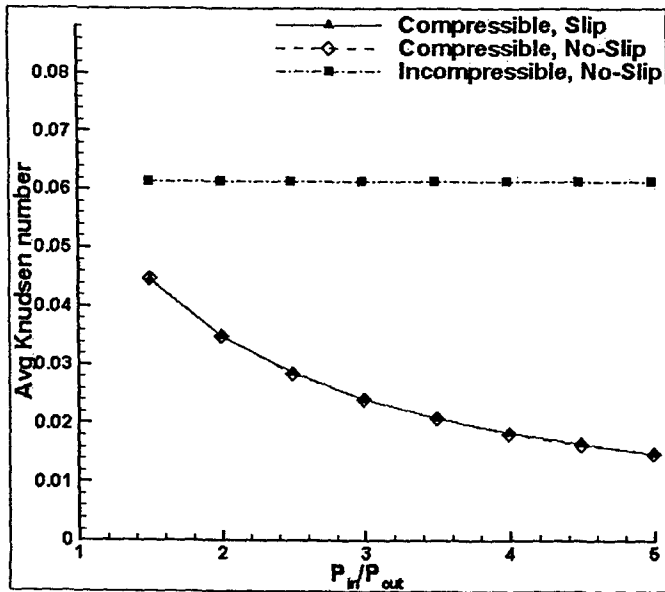


Figure 35. Average Knudsen number with varying pressure ratio.

As the pressure ratio increased the average mass weighted Mach number increased as shown in Figure 36 compressible no-slip case had the least average Mach number then compressible slip case. At relatively low $PR = P_{in}/P_{out}$, average Mach number for compressible slip flow was the highest; while at relatively high P_{in}/P_{out} , the incompressible no-slip flow's average Mach number was the highest. The reason could be that as the pressure ratio increased the compressibility effects became more dominant.

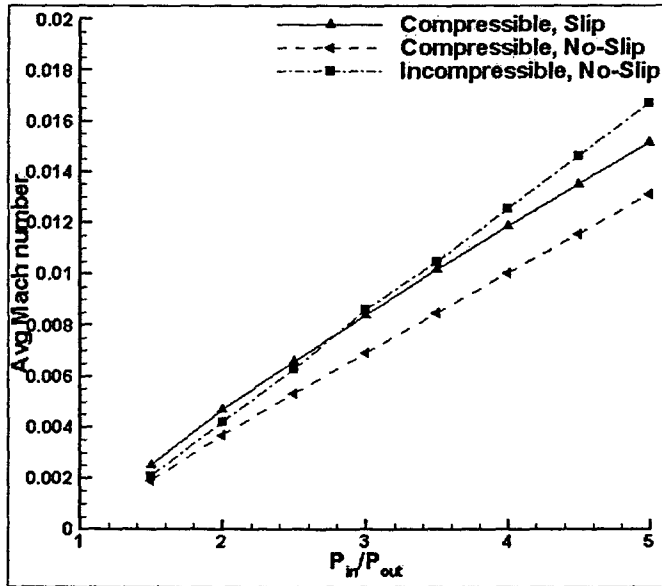


Figure 36. Average Mach number with varying pressure ratio.

Normalized friction coefficient, $C_c^* = fRe_{Comp}/fRe_{Incomp}$, was calculated for varying pressure ratio as shown in Figure 37. The incompressible friction factor was the friction factor for incompressible no-slip boundary conditions fully developed flow, which was constant. The compressible no-slip case had higher friction coefficients and it increased slightly with the increasing pressure ratios. The compressible slip case had friction coefficients lower than that for no-slip flow. These results showed that the slip effect indeed reduced the wall friction significantly. The results also proved that the fRe value of slip flow depend strongly on the pressure ratio (or Reynolds number) especially when P_{in}/P_{out} was low. As mentioned earlier the slip effects decreased with increasing pressure ratio since at higher pressure ratio the gas density was increased and the mean free path of gas molecules were reduced. The Knudsen number and the slip effect diminish with decreasing mean free path.

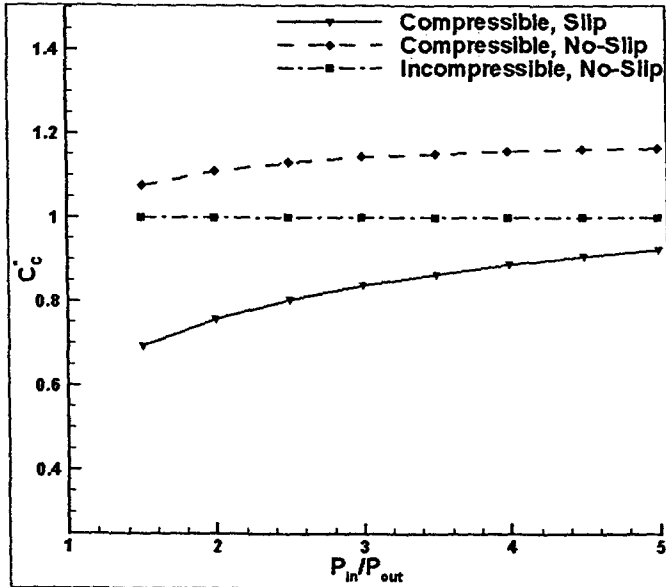


Figure 37. C_C^* versus varying pressure ratio, $C_C^* = fRe_{Comp}/fRe_{Incomp}$.

An analytical expression for normalized friction coefficients was developed on the basis of behavior for compressible slip flow as shown in Figure 37.

$$C_C^* = k_1 e^{k_2 * \left(\frac{P_{in}}{P_{out}}\right)^{-0.5}} \quad (30)$$

Where k_1 and k_2 were the constants, for our case they were $k_1 \sim 1.31 \pm 0.05$ and $k_2 \sim -0.78 \pm 0.02$.

Figure 38 shows the streamwise velocity at centerline for pressure ratio 2.0-5.0, at the channel exit, for slip and no-slip flow conditions with the incompressible no-slip condition also presented. It could be observed in Figure 38 (a) and (b) that compressible slip flow conditions had the maximum centerline velocity when PR = 2.0 – 3.0. But as the pressure ratio increased from 3.0 to 5.0 the incompressible slip flow condition had the maximum centerline velocity as shown in Figure 38 (c) and (d). As discussed earlier this kind of behavior could be due to the diminishing slip effects with increasing pressure

ratio. Though the compressible flow through the microchannel was not fully developed but the traditional parabolic curves exist.

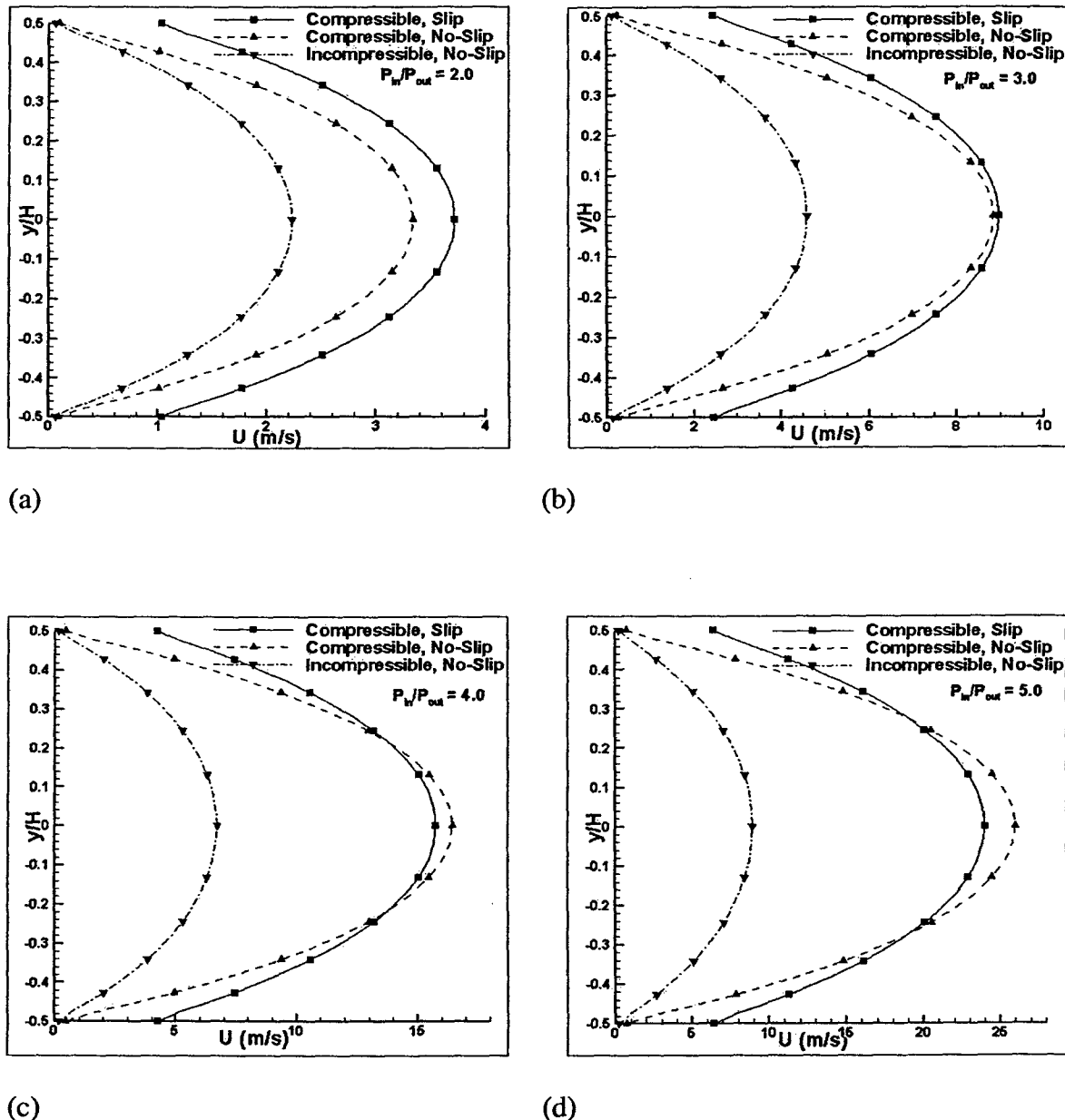


Figure 38. Downstream streamwise velocities at centerline for various pressure ratios, at channel exit.

The corresponding velocity solutions at the channel centerline were plotted in Figure 39. The slip condition solutions consistently show a higher magnitude of velocity than no-slip condition due to lower shear stress at the walls. The nonlinear distribution of the velocity was dependent on the pressure distribution and hence varies for different pressure ratios. As the pressure ratios increased, the non-linearity of the centerline velocity distribution became prominent.

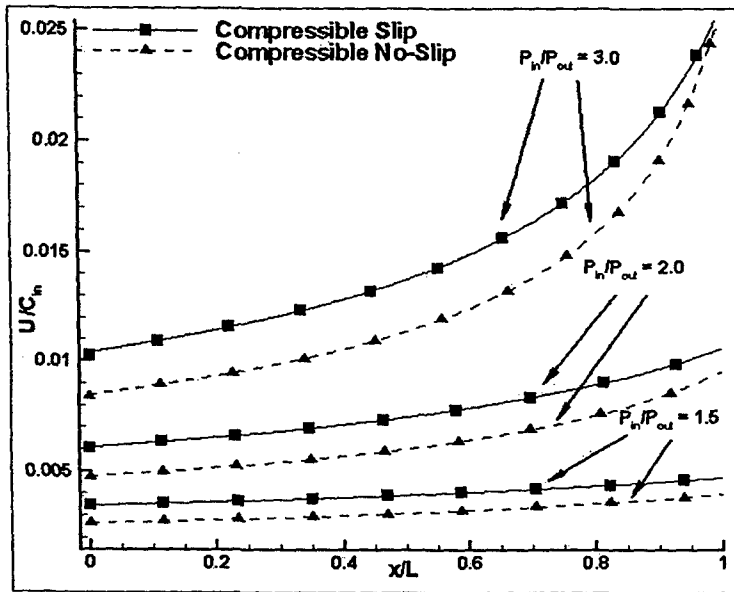


Figure 39. Centerline velocity distribution normalized with speed of sound at the inlet C_{in} for various pressure ratios.

Figure 40 shows the flow development along the microchannel for PR = 3.5. As could be observed, the incompressible flow was fully developed but the compressible flow was not fully developed for slip and no-slip conditions. Figure 40 shows increase in streamwise velocity with the corresponding rise in wall velocity due to slip. As Kn increased due to lower density downstream, the slip affects increased.

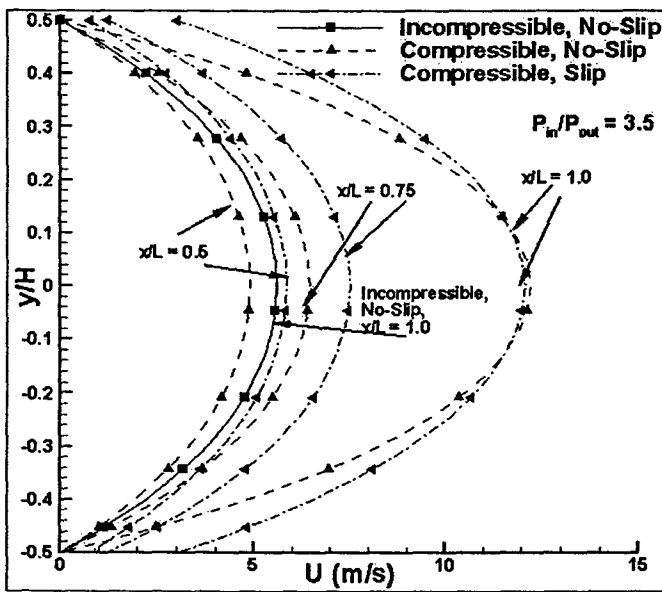


Figure 40. Slip and no-slip U-velocity at different cross-sections along the y-direction.

3.2.2.4 Three Dimensional (3-D) Effects

To investigate the 3-D effects, compressible gas flow for two-dimensional microchannel was simulated to compare with 3-D simulation. The geometric configurations was $L/D_h = 200$, $D_h = 1 \mu\text{m}$.

This study was conducted with slip flow boundary conditions. Figure 41 compares the velocity solutions along the channel centerline. As can be observed for exactly the same conditions the U-velocity component always had higher magnitude for 2-D flow then 3-D flow. The difference between U-velocity component for 3-D and 2-D flow was in the range of 15% to 20%.

This showed for compressible flows the assumption of 2-D microchannel was not accurate and it could not get acceptable results as expected. Similar behavior was

observed for V-velocity component along y-direction at the channel centerline as shown in Figure 42. The difference between V-velocity component for 3-D and 2-D flow was in the range of 20% to 25%.

Figure 43 shows the W-velocity component at channel centerline for 3-D case at the exit of the channel. The magnitude of W-velocity increased with increasing pressure ratio. This is three-dimensional effect, which was neglected, in two-dimensional study.

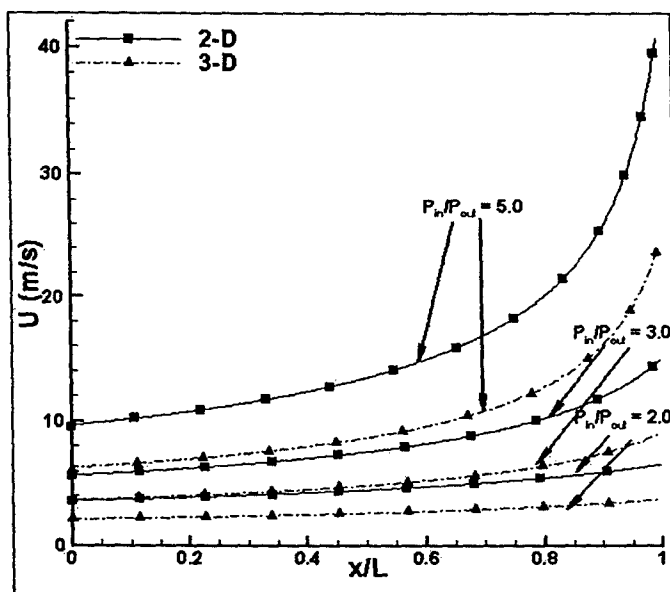


Figure 41. Centerline U-velocity distribution for compressible gas flow with slip flow boundary conditions.

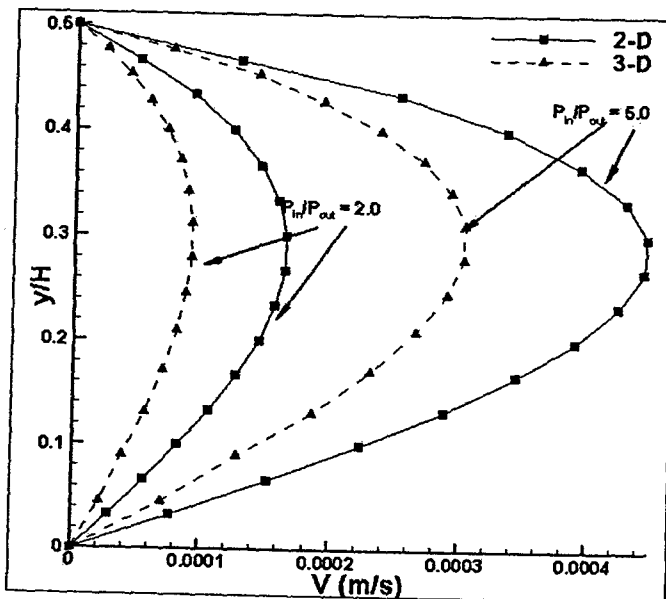


Figure 42. V-velocity at centerline cross-section along the y-direction for compressible gas flow with slip flow boundary conditions.

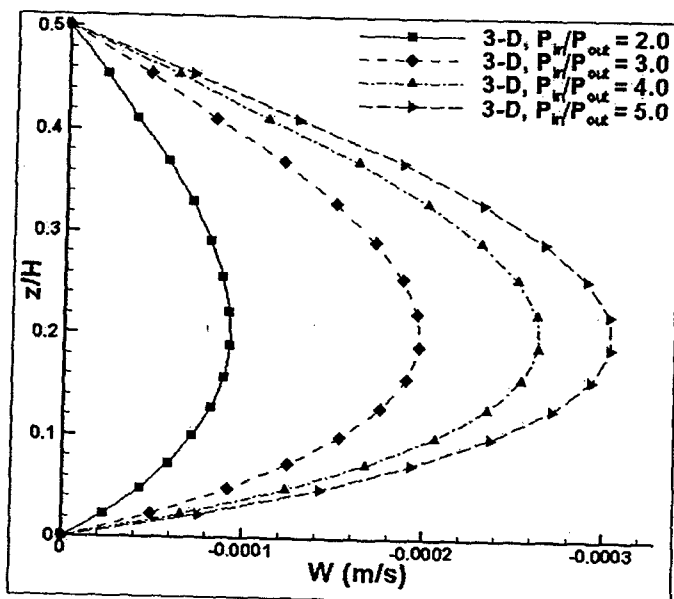


Figure 43. W-velocity at centerline cross-section along the z-direction for compressible gas flow with slip flow boundary conditions.

Figure 44 compares C_C^* for 2D and 3D case. As could be seen from Figure 44, the two-dimensional microchannel always gave lower C_C^* and thus deviating from the actual values. This validated our point that one could not use two-dimensional assumption to predict the compressible flow accurately. The difference in the 3-D and 2-D results was in the range of 7% to 12%.

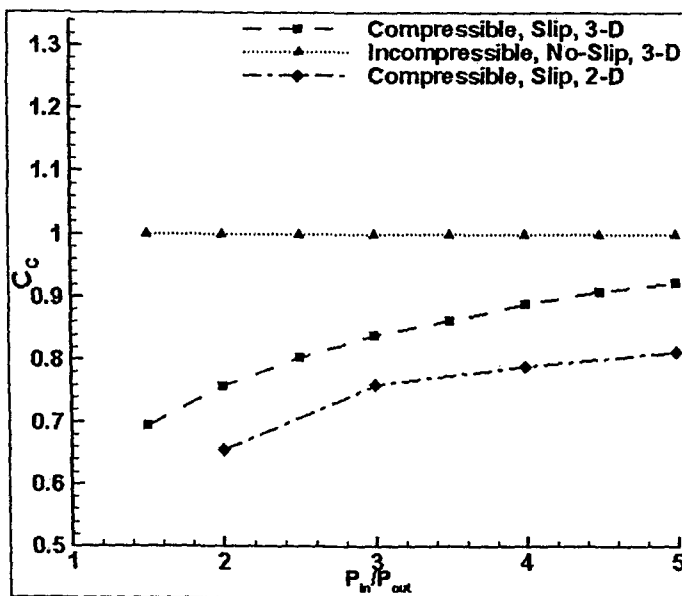


Figure 44. C_C^* versus varying pressure ratio, $C_C^* = fRe_{Comp}/fRe_{Incomp}$.

3.2.2.5 Effects of Aspect Ratio

To study the effect of varying channel aspect ratio we varied the height and width of the microchannels. To maintain dynamic similarity, we kept the hydraulic diameter fixed as 1 μm as shown in Table 4. The maximum Knudsen numbers at the channel outlet were less than 0.06. In the following simulation, the slip effects were included. The channel outlet pressure was fixed at atmospheric pressure, and the inlet pressure varied from 2.0–5.0.

Table 6. Microchannels dimensions used for aspect ratio effect study.

AR	$W (\mu\text{m})$	$H (\mu\text{m})$	D_h
1	1	1	1
0.75	1.167	0.875	1
0.5	1.5	0.75	1
0.25	2.5	0.625	1
0.20	3	0.60	1

Figure 45 depicts the calculated normalized friction constant, C^* , as a function of pressure ratio for different aspect ratio. As shown in Figure 45, C^* increased with the decrease in aspect ratio. As the aspect ratio decreases the channel height becomes narrower, which gives rise to a wall friction. As the aspect ratio was decreased to 0.20, the strongest slip effects increased the C^* to almost twice then at aspect ratio of AR = 1.

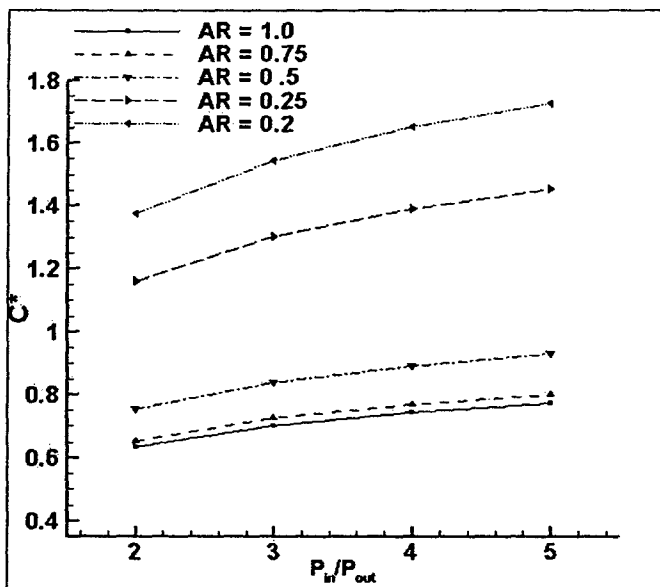
**Figure 45. Normalized Friction constant as a function of pressure ratio for varying aspect ratio.**

Figure 46 depicts the increase in mass flow rate with reducing aspect ratio. As shown in Figure 47, as the aspect ratio increased the mean velocity reduced, this is due to increase in the wall friction effects.

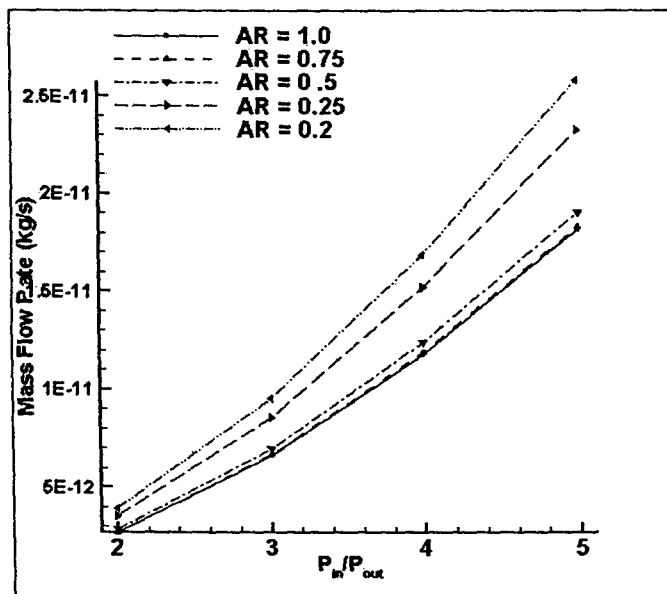


Figure 46. Mass flow rate as function of pressure ratio.

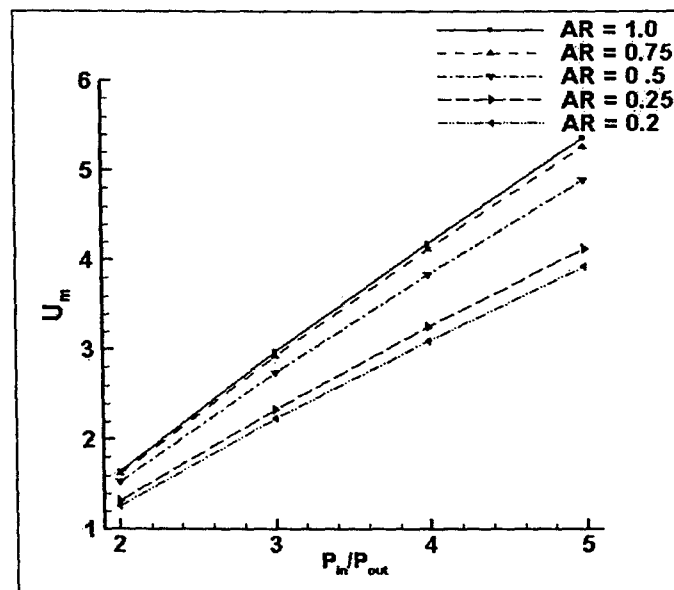


Figure 47. Mean velocity as function of pressure ratio.

The investigation of effects of aspect ratio on the laminar friction constant for compressible gas flows would be incomplete if we don't investigate the effects on flow properties with increase in aspect ratio. The aspect ratio was increased from 1 to 5, keeping the hydraulic diameter constant ($D_h = 1\mu\text{m}$). As shown in Figure 48, the normalized laminar friction constant is minimum for square microchannel and it increases as the aspect ratio decreases or increases from 1. Figure 49 shows the effect of aspect ratio on the mass flow rate, as the aspect ratio deviates from 1 the mass flow rate increases. As shown in figures the behavior is symmetrical.

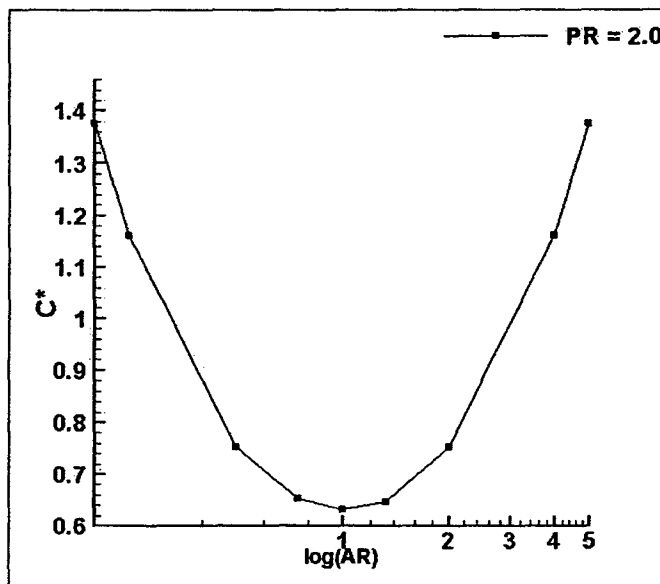


Figure 48. The C^* with varying aspect ratio at $\text{PR} = 2.0$

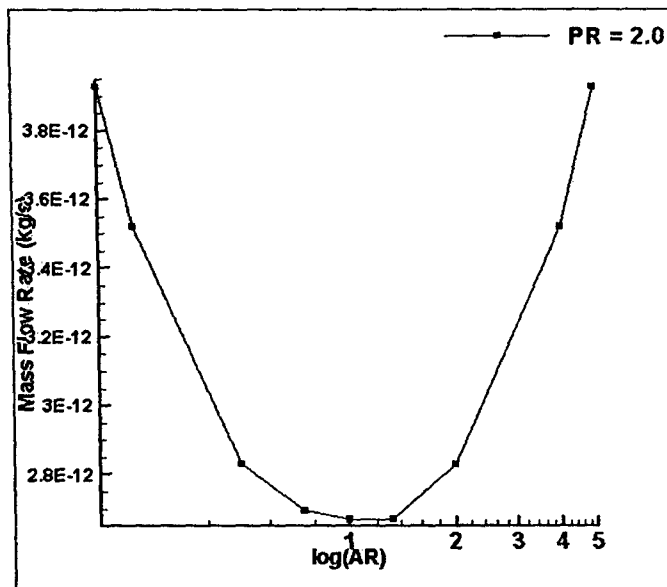


Figure 49. Mass flow rate with varying aspect ratio.

The effect of aspect ratio was further investigated at the various pressure ratios. As can be seen in Figure 50, as the pressure ratio increases the normalized laminar friction constant, C^* increases, this is due to increasing compressibility and diminishing rarefaction effects. It is interesting to observe that the behavior of the friction constant versus aspect ratio is symmetrical and the trend continues for varying pressure ratios. A narrower or wider channel has larger friction at the walls and therefore higher friction factor. The friction characteristic for compressible flow in microchannels is much more complicated than that for incompressible flow in conventional-size channels. For incompressible conventional channel flow, the normalized laminar friction constant is only a function of aspect ratio. But as shown in Figure 50, for compressible flow, the normalized laminar friction constant is a function of Knudsen number, compressibility (pressure ratio) and aspect ratio in microchannels.

Figure 51 shows the mean flow velocity as a function of aspect ratio. It can be observed that as the pressure ratio increases the mean flow velocity increases due to compressibility effects. And, at aspect ratio of 1.0, the channel has the maximum mean flow velocity.

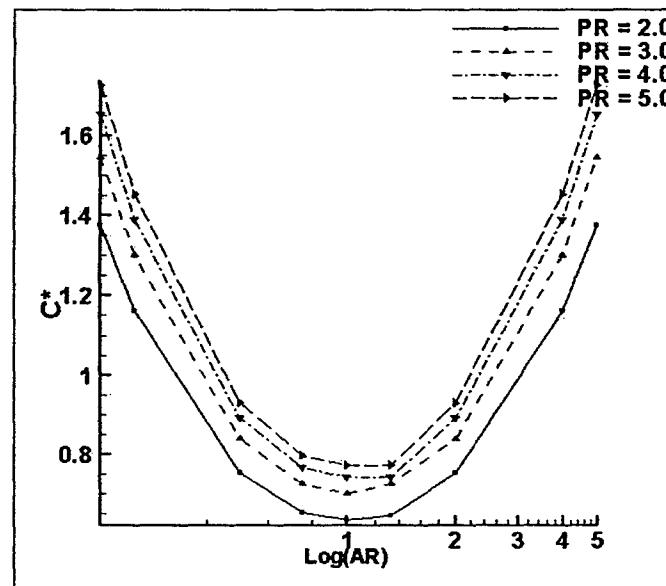


Figure 50. The C^* with varying aspect ratio at various pressure ratios.

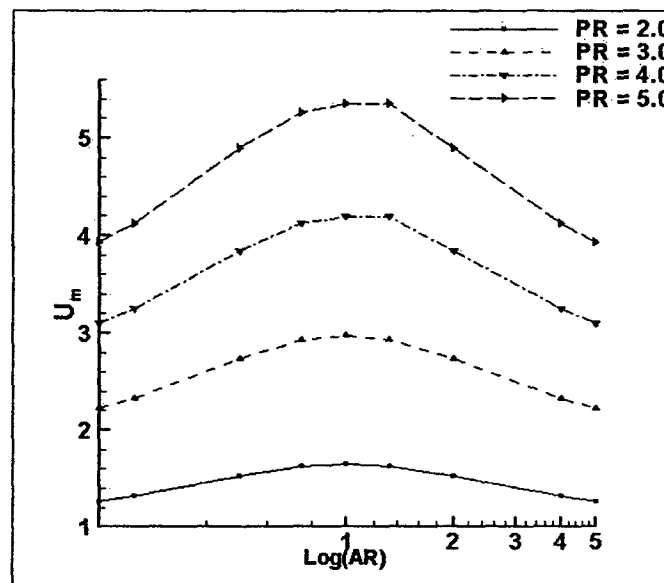


Figure 51. Mass flow rate with varying aspect ratio at various pressure ratios.

3.2.3 DSMC Simulations of Axisymmetric Gas Flow in Conical Micronozzles

The direct simulation Monte Carlo (DSMC) method of Bird (1976) is a statistical simulation technique that models a real flow governed by Boltzmann equation with a set of representative molecules. Current applications of DSMC are limited to near continuum and rarefied flows due to its intensive computational cost (Chung et al. 1995). 2D and 3D gas flows in micronozzles were investigated by DSMC to aid the development of microelectromechanical system (MEMS) applications in micro-scale thrusters, etc. (Ivanov et al. 1999, Markelov and Ivanov 2001, Alexeenko et al. 2002, Boyd et al. 1992 and 1994), where Rothe's (1971) experiment was frequently used as the reference problem. Chung et al. (1995), studied low-density nozzle flow by DSMC and continuum methods based on Rothe's (1971) experimental data. It was reported that the continuum method could provide good results inside the nozzle in terms of density while DSMC could provide good results in both density and rotational temperature.

The present study is focused on the performance evaluation of DSMC and continuum methods for the simulations of normal-density gas flows at low Reynolds number in a conical micronozzle with throat diameter of 1 mm (in contrast to Rothe's (1971) 5 mm), in order to explore the advantages of using the two approaches in different flow regimes.

Experimental work of Jamison et al. (2003) is used as the reference problem (Figure 52). The throat diameter is $D_t = 1$ mm and exit diameter, $D_e = 7.9$ mm, which gives an expansion ratio of $\varepsilon = 62.41$. The half angles are 30^0 and 20^0 in the converging

and diverging sections respectively. The total length of the nozzle is $L = 10.7$ mm. Helium gas is used as the working fluid.

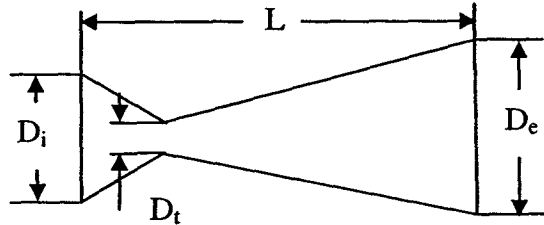


Figure 52. Nozzle geometry.

The Reynolds number is calculated at the nozzle throat as:

$$Re = \frac{\rho U D_t}{\mu} \quad (31)$$

Knudsen number is calculated at the nozzle inlet:

$$Kn = \frac{\lambda}{D_i} \quad (32)$$

Where λ is molecular mean free path and calculated as (Mohamed 1999):

$$\lambda = \frac{kT}{\sqrt{2\pi\sigma^2 P}} \quad (33)$$

The flow regimes are categorized by Knudsen number as (Mohamed 1999): $Kn < 10^{-3}$, continuum flow; $10^{-3} < Kn < 10^{-1}$, slip flow; $10^{-1} < Kn < 10$, transitional flow; $Kn > 10$, free molecular flow. Important parameters used in the simulations are listed in Table 7.

Table 7. Computation Parameters.

Throat	Nozzle Inlet		DSMC	
Re	P(Pa)	Kn	Cell Size, m	Timestep, s
0.16	50.127	0.1398	1.12E-04	8.28E-08
0.22	58.501	0.1198	9.62E-05	7.10E-08
0.38	78.859	0.0889	7.14E-05	5.26E-08
0.55	87.616	0.0800	6.42E-05	4.74E-08
0.77	99.651	0.0703	5.65E-05	4.17E-08
1.04	119.781	0.0585	4.70E-05	3.47E-08
2.64	206.087	0.0340	2.73E-05	2.01E-08
5.16	275.927	0.0254	2.04E-05	1.50E-08
7.58	390.045	0.0180	1.44E-05	1.06E-08
10.93	423.106	0.0166	1.33E-05	9.81E-09
14.45	463.021	0.0151	1.22E-05	8.97E-09
18.08	539.380	0.0130	1.04E-05	7.70E-09
22.69	695.976	0.0101	8.09E-06	5.97E-09

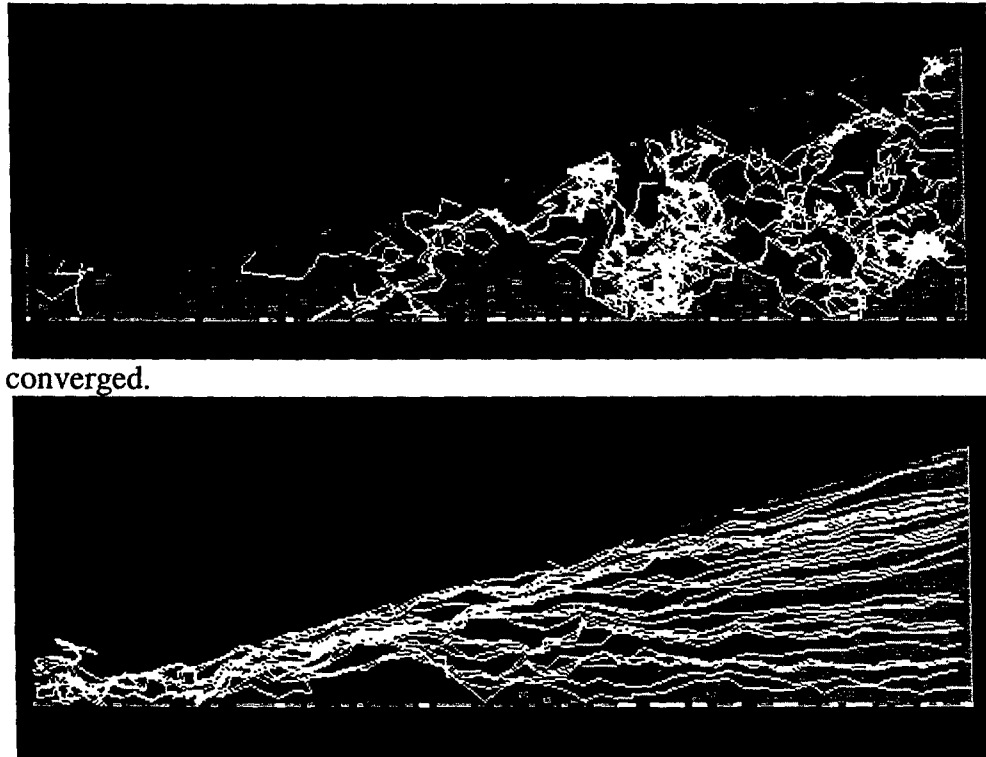
Bird's DS2V DSMC codes are used for the calculations. Nozzle geometry is divided into a set of cells with the cell size calculated as one third of the molecular mean free path. Timestep is calculated as one third of the molecular mean collision time. Initially, the number of simulated particles in the computational domain is assigned arbitrarily. The number ratio of simulated molecules to real molecules leads to the statistical scatter, following the Poisson distribution, with the standard deviation on the order of the inverse square root of the sample size. The simulation fluctuations may become unstable in some flow configurations due to random walk effect in one or more variables. One characteristic of a random walk is that displacement from mean position or value increases with square root of time. Random walk can arise whenever one of the molecular quantities is conserved only on the average, rather than exactly, in any of the simulation procedures.

The core of the DSMC algorithm consists of four primary processes:

1. Move the particles
2. Index and cross-reference the particles
3. Simulate collisions
4. Sample the flow field.

These procedures are uncoupled during each time-step. Of primary importance is the selection of a timestep that is less than the mean collision time. Simulation results are independent of the timestep increment as long as this requirement and the cell-size requirement on the gradient resolution are satisfied.

The DSMC technique is explicit and time-marching, so that it always produces a flow simulation that is unsteady. For an unsteady flow application, an ensemble of many independent computations may be assembled and averaged to obtain final results with an acceptable statistical accuracy. An ensemble average (the instantaneous average over area or volume elements of an arbitrarily large group of similar systems) is commonly used to present unsteady DSMC results. To simulate a steady problem, each independent computation proceeds until a steady flow is established at a sufficiently large time, and the desired steady result is a time average of all values calculated after reaching the steady state. With a cumulative sample, the statistical fluctuations declines with the square root of the sample size and it should be possible to achieve any desired level of accuracy by continuing or repeating the simulation to build up the size of the sample to the required magnitude. The gradual approach of a sampled quantity to its correct value is sometimes referred to as ‘convergence’. Figure 53 shows the judgment of convergence by observing the smoothness of flow stream line.



a) Not converged.

b) Possibly converged.

Figure 53. Judgment of convergence by observations.

As shown in Table 7, with the decrease of Knudsen number, DSMC cell size and timestep are both decreasing due to the decrease of the molecular mean free path. In continuum and slip flow regimes, the fluid is much denser and the rarefaction effect is negligible, where DSMC is much more time consuming than Navier-Stokes (NS) method. The nozzle exit thrust simulated by DSMC and NS methods show good agreement with experimental data at throat Reynolds number larger than 10 (Figure 54) where the flow is in slip regime. With the decrease of throat Reynolds number, the fluid density reduces and the rarefaction effect becomes important. In this flow regime, NS simulation is heavily influenced by the back flow at the exit and the exit pressure is limited to a fixed value (1 Pa in this report), resulting in larger predictions of exit thrust. By assuming the exit pressure is negligible, the exit thrust calculated by NS method

demonstrates a good agreement with the experimental results. While the DSMC predicts larger thrust than the experimental data with a similar variation trend with the throat Reynolds number.

As shown in Figure 55, at throat Reynolds number of 18.08, the pressure, Mach number and temperature contours predicted by DSMC and NS methods are similar in pattern, except the magnitude and smoothness of distributions. The exit pressure is 0 in DSMC and a very small value (close to 1 Pa) in NS. The pressure difference is not obvious in pressure contour (Figure 55 a), but it causes a larger Mach number predicted by DSMC (Figure 55 b). The temperature distribution near the wall is larger in DSMC predictions (Figure 55 c).

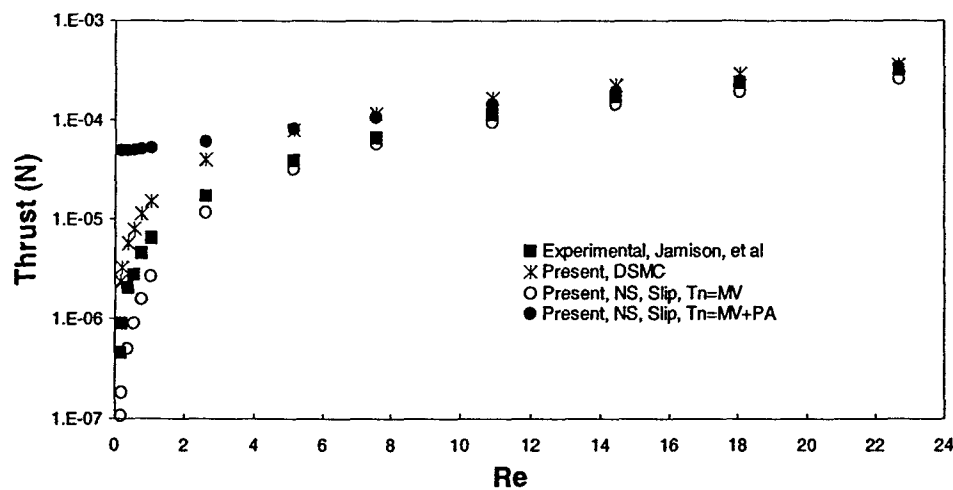


Figure 54. Nozzle exit thrust vs. throat Reynolds number.

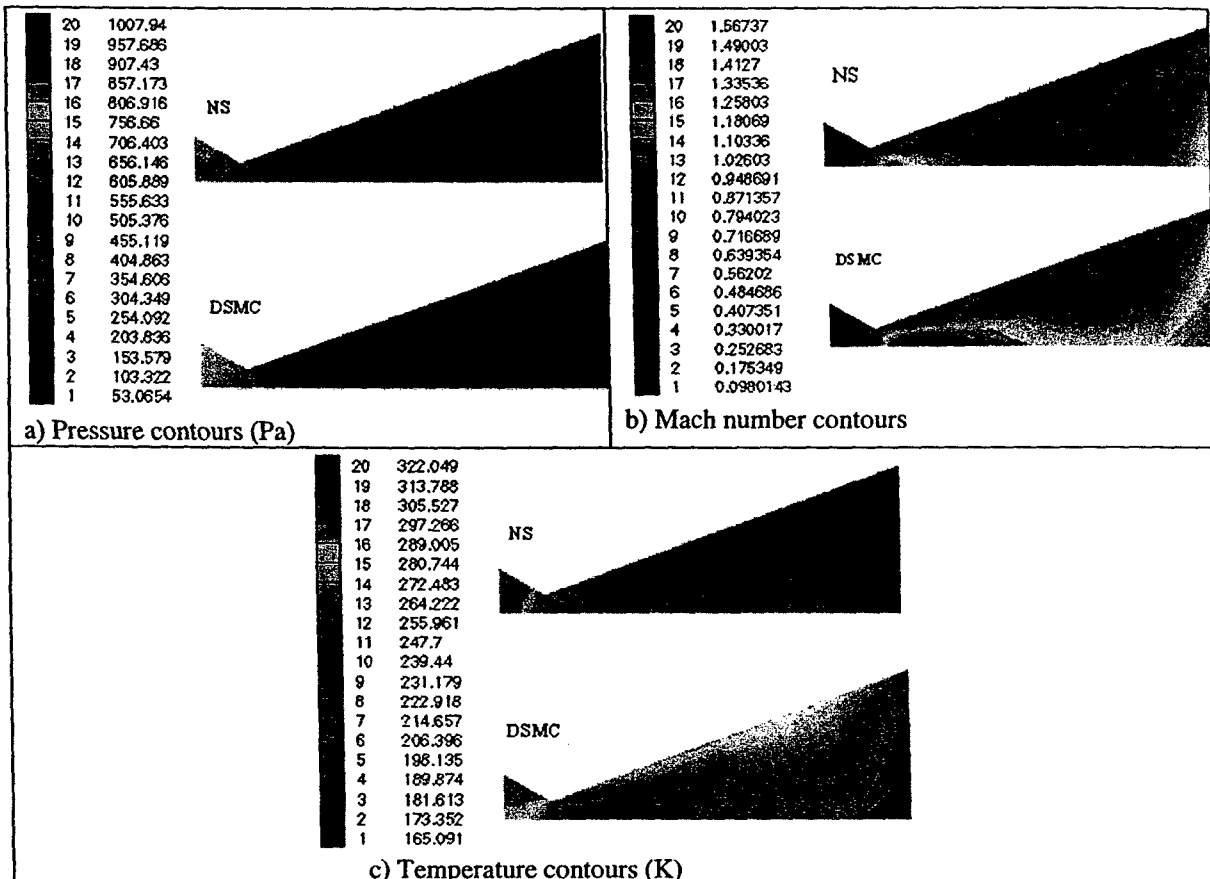


Figure 55. Contours predicted by DSMC and NS methods (throat Reynolds number = 18.08).

Figure 56 shows the effect of the inlet temperature of the propellant gas at $P_0 = 1$ Torr, $D_{\text{throat}} = 1$ mm. With higher inlet temperature, the molecular kinetic energy is higher, resulting more thrust generated.

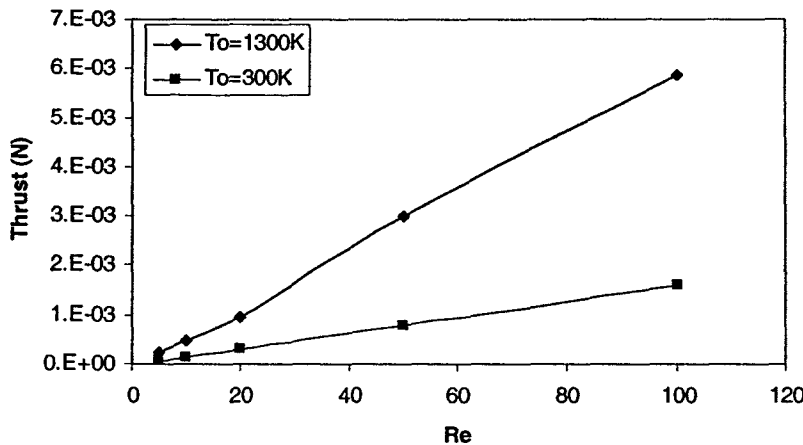


Figure 56. Effect of the inlet temperature of the propellant gas at $P_0 = 1$ Torr, $D_{throat} = 1$ mm.

3.2.4 Modeling using Unified Flow Solver

This section contains modeling results obtained in the course of consulting services from CFD Research Corporation (CFDRC) and presented in the Final Report by CFDRC entitled “Testing & Demonstration of the Unified Flow Solver for Micro Flow Applications”. The team has been working with CFDRC in selection of test cases and in modeling and evaluation of the Unified Flow Solver (UFS) for gas flows in microchannels and micronozzles.

The Unified Flow Solver is developed for rarefied and continuum flows. The UFS code includes deterministic Boltzmann solver for highly non-equilibrium flows at high Knudsen number and continuum (Euler or Navier-Stokes) solvers for low Knudsen numbers (see Figure 57). Direct Numerical Solution of the Boltzmann equation is preferable to DSMC for coupling kinetic and continuum models and for simulations of low speed flows.

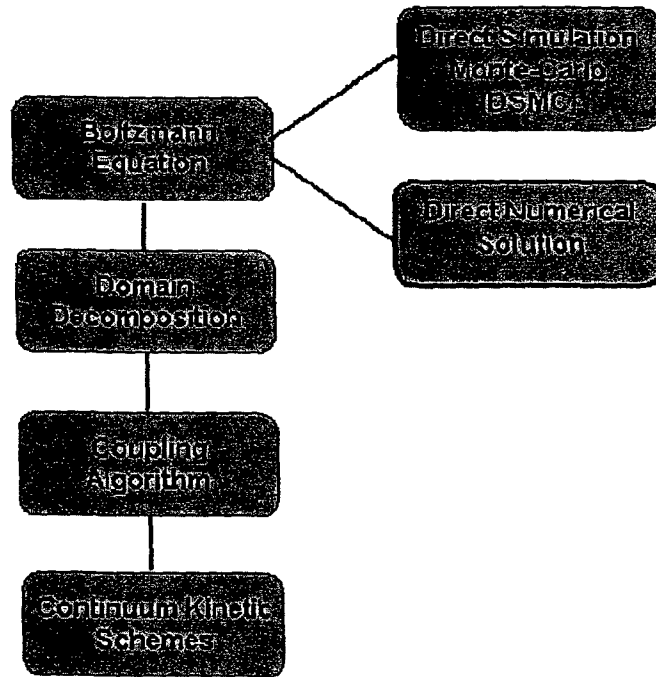


Figure 57. The architecture of the Unified Flow Solver.

The UFS uses continuum breakdown criteria to dynamically select kinetic and continuum domains and applies appropriate boundary conditions to couple the Boltzmann and continuum solvers at the boundaries.

3.2.4.1 Boltzmann and Continuum Solvers

The Boltzmann transport equation (BTE) for a particle distribution function f in a one component atomic gas has the form:

$$\frac{\partial f}{\partial t} + \nabla_r \cdot (vf) + \nabla_v \cdot (af) = N - vf \quad (34)$$

Here r is spatial coordinate, v is velocity vector, and a is acceleration vector. The left hand side of Eq. (34) describes the free motion of the particles, the right hand side

describes collisions among the particles. The elastic binary collisions are described by integral operators

$$\nu = \int_R \int_S \sigma(|\xi - \xi_1|, \omega) |\xi - \xi_1| f(\xi_*) d\omega d\xi_*$$

$$N(f, f) = \int_R \int_S \sigma(|\xi - \xi_1|, \omega) |\xi - \xi_1| f(\xi') f(\xi'_*) d\omega d\xi_* \quad (36)$$

Here ω is a unit vector on a sphere S in velocity space, and $d\omega$ is an element of the area of the surface of this sphere, where (ξ', ξ'_*) represent the post collisional velocities associated with the precollisional velocities (ξ, ξ_*) and the collisional parameter ω , and the kernel σ describes details of the binary interactions.

The kinetic gasdynamics scheme for the continuum equations is based on finite volume evaluation of semi-fluxes at cell faces using analytical values for a Maxwellian distribution function. For the Navier-Stokes equations, the semi-flux scheme is based on BGK equation. Directional splitting method is used, and flux in one direction is evaluated by means of the construction the distribution function $f_0(t, x, \xi)$, and Maxwellian $g(x, t)$ around the cell face at each time step. For a 1D case this means:

$$f_0(x) = g^l [1 + a^l x - \tau(a^l \xi + A^l)] (1 - H[x]) + g^r [1 + a^r x - \tau(a^r \xi + A^r)] H[x],$$

$$g(x) = g_0 [1 + (1 - H[x]) \bar{a}^l x + H[x] \bar{a}^r x + At], \quad (37)$$

where $H[x]$ is the Heaviside step function, g^l and g^r are Maxwellian distributions at the left and right sides of the cell face, g_0 is a Maxwellian at the cell face, and functions $a^{l(r)}, \bar{a}^{l(r)}, A^{l(r)}$ and A are polynomials with local coefficients. The fluxes at cell faces are computed using general solution of the BGK equation for the distribution function f . Note that term $\tau(a^{l(r)} \xi + A^{l(r)}) g^{l(r)}$ defines deviation of the distribution function from

equilibrium, where $\tau = \mu / p$. This procedure gives equations for mass, momentum and energy transport and approximates NS equations. If the parameter τ is set to zero, the Euler kinetic scheme is obtained.

The automatic switch between the Boltzmann solver and the continuum solvers is performed using binary switches that belong directly to the “cell” structure and are accessible everywhere throughout the UFS code. The memory for the Boltzmann solver is allocated only in the kinetic regions of the computational domain. The rest of the computational domain is solved by the continuum (Euler or NS) solvers. The switch is based on gasdynamic macroparameters and so is known everywhere in the computational domain.

The following switching criteria are available in the source code:

$$S_{gk\rho} = Kn \sqrt{\left(\frac{\nabla \rho}{\rho}\right)^2 + \frac{1}{T} \left[\left(\frac{\partial u}{\partial x}\right)^2 + \left(\frac{\partial v}{\partial y}\right)^2 + \left(\frac{\partial w}{\partial z}\right)^2 \right]} \quad (38)$$

$$S_{NS} = \tau \sqrt{\left(\frac{\nabla p}{p}\right)^2 + \left[\left(\frac{\partial u}{\partial x}\right)^2 + \left(\frac{\partial v}{\partial y}\right)^2 + \left(\frac{\partial w}{\partial z}\right)^2\right] / (u^2 + v^2 + w^2)} \quad (39)$$

where p_{xx}, p_{yy}, p_{zz} are appropriate components of the non-equilibrium stress tensor, p is the pressure, ρ is density, T is temperature, u, v, w are appropriate component of velocity (all values are given in dimensionless form). If S is greater than a threshold value, then the kinetic solver must be used. The applicability of different criteria and the ways to choose the threshold value is currently being studied. So far, it was obtained

experimentally that criterion S_{NS} gives correct kinetic regions and allows successfully couple NS kinetic solver with Boltzmann solver.

In order to match the Boltzmann and the Euler solutions, a special technique is used which consists in the following. In a narrow layer around the Boltzmann region, Maxwellian distribution is calculated based on local gasdynamics macroparameters. The advection part of the Boltzmann solver is then run using these Maxwellian distributions in the surrounding layer.

3.2.4.2 Simulation of Microchannel Flow

Simulation conditions corresponding to experiments of Hsieh et al. (2004) were used for microchannel flow test case.

In order to reduce the computational effort, the simulation domain in the y-z slice includes only a quarter of the domain under the study as shown in Figure 58. Two boundaries in the y-z slice are considered as symmetry and the other two as Neumann boundaries on which diffusive reflection with $T = 1$ is set (see Figure 58).

The inlet and exit boundaries are treated as Inflow and Outflow boundaries. On the Inflow boundary, the density and pressure is set; the velocity field is taken from the simulation domain values so that normal derivatives of the velocities are zero. On the Outflow boundary, only the pressure is set; the velocity and density field is taken from the simulation domain values so that normal derivatives of the density and velocities are zero. This is a usual way of setting boundary conditions for simulations of flow in long tubes.

Results of the simulation are shown in Figure 59 as contour plots of the density, longitudinal velocity, and temperature.

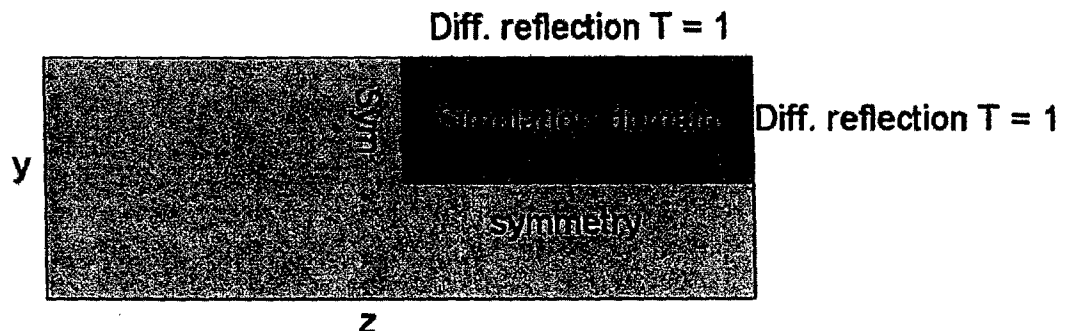
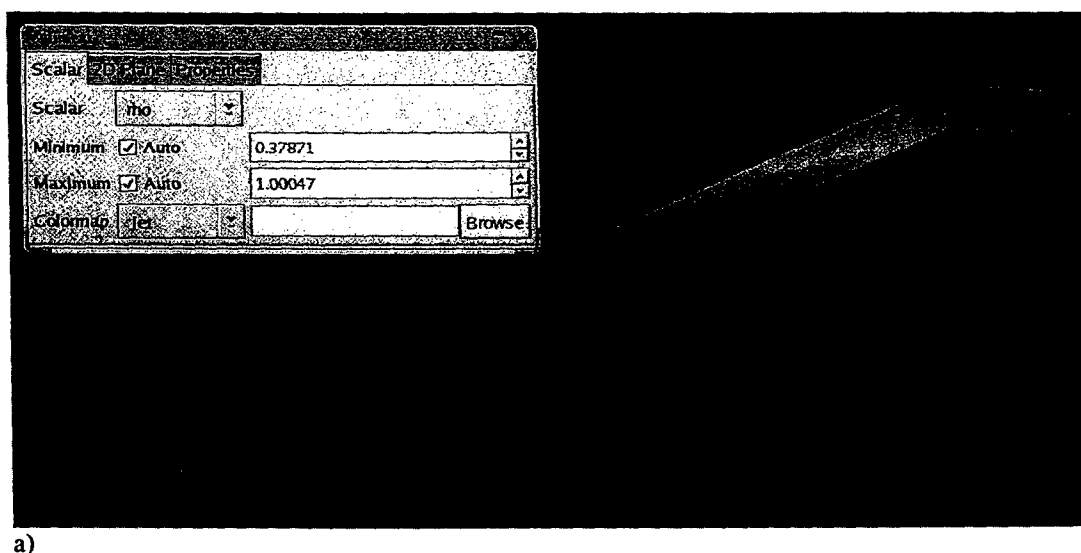


Figure 58. Simulation domain and boundary conditions in the y-z slice of the studied geometry.



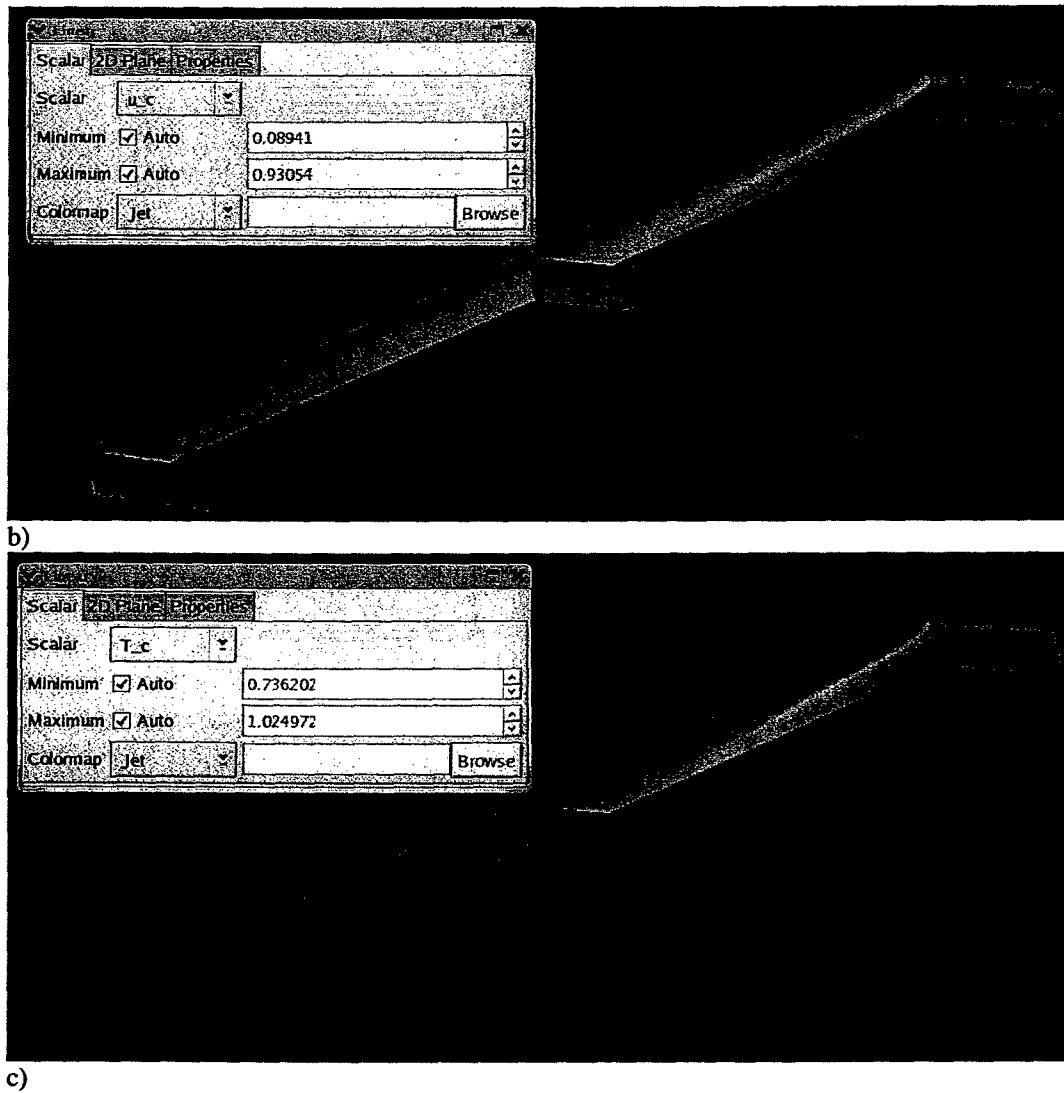


Figure 59. Results of microchannel flow simulation by Unified Flow Solver: a) density; b) longitudinal velocity; c) temperature.

3.2.4.3 Simulation of Micronozzle Flow

Experimental and modeling results of Bayt (1999) were used as a reference case for testing UFS for micronozzle flow applications. Following boundary conditions were used $\rho = 1$, $u = 0.2 * \text{sqrt}(5./6.*1.2)$ and $T = 1.2$ at the entrance and $\rho = 0.05$, $u = 1.73$ and $T = 0.2$ at the exit. Thus, at the entrance, the Mach number is set to 0.2. These

boundary conditions are close to those in the Bayt thesis (1999). The results of simulations using the gasdynamic solver are shown in Figure 60. For comparison, we show the Mach number profiles from the Bayt theses in Figure 61. One can see a good comparison with the results of the UFS code.

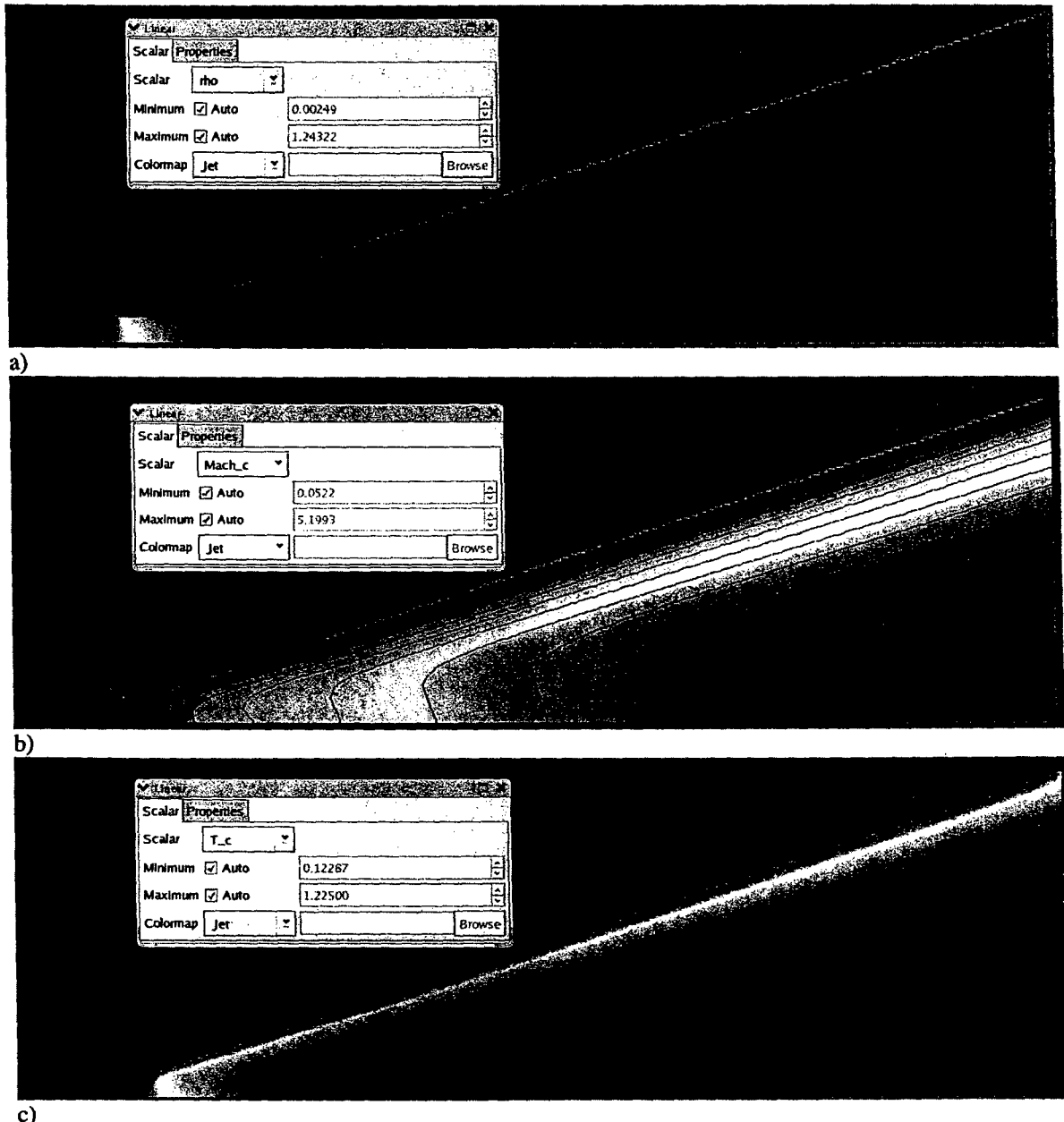


Figure 60. Results of simulation of the Bayt's nozzle using the Euler solver: a) Density contours; b) Mach number contours; and c) Temperature contours.

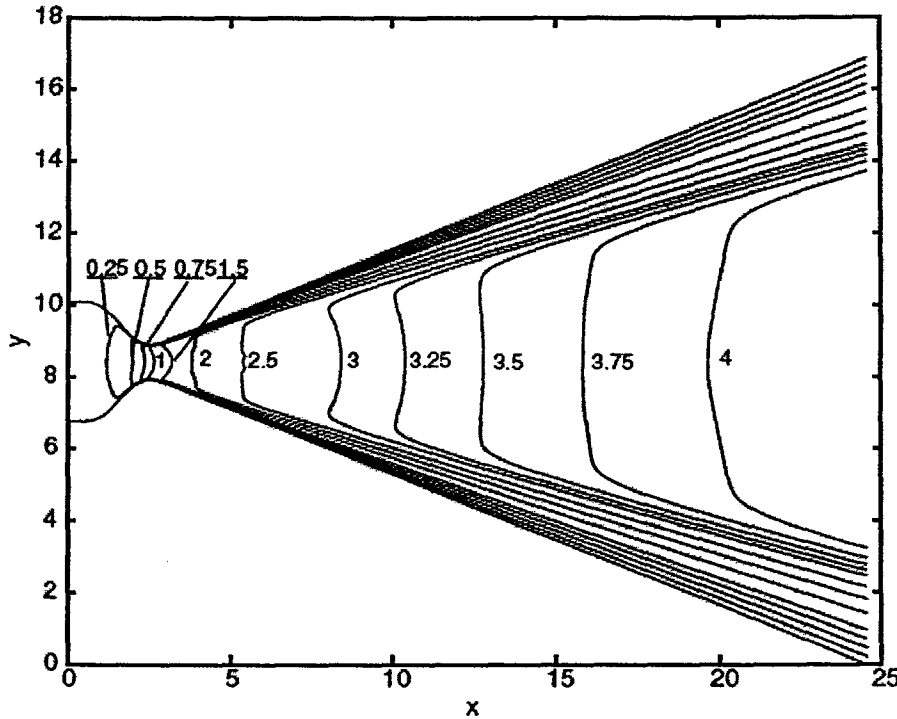


Figure 61. Mach number contours for the 16.9:1 nozzle at a Reynolds number of 1914 (from Bayt (1999)).

The above simulation was repeated with $\text{Kn}=0.001$ to demonstrate the automatic switch between the gasdynamic and Boltzmann solvers. The results are presented in Figure 62. One can see that there is a considerably large kinetic region (shown in red in Figure 62 a)) in the portion of the nozzle with low density.

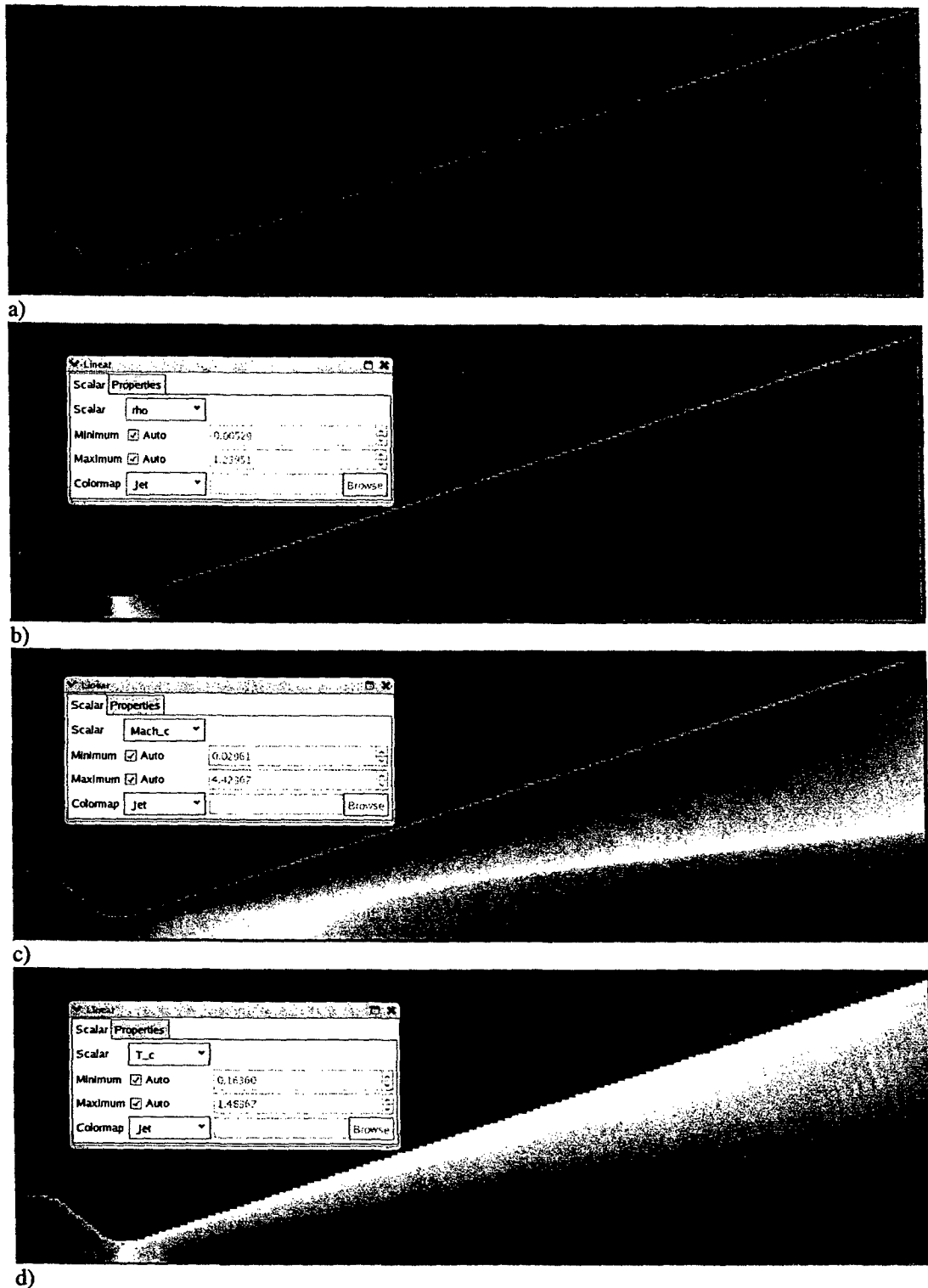


Figure 62. Results of micronozzle flow simulation by Unified Flow Solver ($\text{Kn}=0.001$): a) kinetic flag; b) density contours; c) Mach number contours; d) temperature contours.

3.3 Summary and Conclusions

A test set-up capable of establishing controlled gas flow in microchannels and micronozzles has been designed, assembled, and tested. Validation of the set-up was performed by conducting flow tests with pure nitrogen gas and comparing measurements with classical correlations for fluid flows in square duct. Reasonable agreement of experimental data with correlations was observed when hydraulic diameter of 500 μm to 550 μm was used in the correlations. A micro gas Laser Induced Fluorescence system was setup. Image analysis script utilizing Image Correlation Velocimetry (ICV) principles was written and tested with specially designed test images as well as with images with added random noise. The velocity profile obtained by ICV script was found to follow closely the test profile used to obtain test images. The script was capable to tolerate random noise of up to 5% of total gray scale. Gas velocity measurements in microscale were conducted using ICV technique for free jet flow exiting from the microchannel. Maximum deviation of experimentally measured average velocity via LIF-ICV technique from estimation based on the set gas mass flow rate was 12.4%. Velocity measurements were also preformed via Molecular Tagging Velocimetry technique and produced good agreement with estimation of average velocity for incompressible flow in a rectangular duct.

Continuum modeling on nozzle flows was conducted and validated by available experimental data. A numerical study has been performed on the effects of throat diameter via geometric scaling down of throat diameter from 10 mm to 0.1 mm for four different throat Reynolds numbers with helium as test propellant. Variation of I_{sp} was

found to be negligible from 1mm to 0.1 mm when compared to 10 mm to 1mm of throat diameter for a given throat Reynolds number for helium flows. Similar behavior for I_{sp} was observed for other propellants. A correlation for specific impulse involving throat diameter and throat Reynolds number was developed and presented. The correlation is capable of predicting I_{sp} with an error of up to 10 % of the actual value.

In a numerical study of gas propellants it was found that helium proved to be best among nitrogen, argon and carbon dioxide for throat Reynolds number varying from 5 to 2000 for the three throat diameters investigated. Nitrogen followed helium. The comparative performance of argon and carbon dioxide varied depending on the throat diameter and the throat Reynolds number.

In the modeling of three-dimensional gas flow in microchannels, for incompressible model, the effect of variation of L/D_h on fRe or C_{IC}^* was found negligible. As the hydraulic diameter was varied from, $D_h = 0.01$ to $100 \mu\text{m}$ friction factor increased. An analytical correlation was developed to predict the normalized friction factor variation with change in pressure ratio for incompressible flow.

Compressibility and rarefaction effects in three-dimensional microchannel gas flow were studied with Reynolds number varying from 0.0001 to 1.2, pressure ratio varying from 1.5 to 5.0, and Knudsen number varying from 0.001 to 0.06. The findings are summarized as follows:

- Due to compressibility effects, the pressure drop exhibits an unusual nonlinear behavior as compared to that in a larger channel. Rarefactions effects were important but as the pressure ratio (or Reynolds number) increased the compressibility effects became major dominant factor.
- Knudsen number increased from inlet to outlet for compressible flow but Knudsen number decreased as the pressure ratio increases.

- With increasing pressure ratio the normalized friction factor increased for both slip and no-slip flows. For the studied range of pressure ratios, the fRe for compressible slip flow is less than fRe for incompressible case.
- An analytical correlation was developed to predict the normalized friction factor variation with change in pressure ratio for compressible slip flow.
- Two dimensional assumption was not valid for compressible flow study in microchannel since it gave much higher velocities, 15% -45% higher then 3-D and lower normalized friction factor, 7% -12% lower then 3-D.

Effects of aspect ratio on compressible gas flow in microchannels were studied for the ranges of pressure ratio from 2.0 to 5.0, Reynolds number from 0.01 to 1.2, and aspect ratio from 0.2 to 5.0. It was observed that the change from square to rectangular microchannel results in the increase of the normalized friction constant. The increase could be almost two times higher for narrower rectangular microchannels compared to the square microchannel. For compressible flow, the normalized laminar friction constant was observed to depend on Knudsen number, compressibility (pressure ratio) and aspect ratio.

In DSMC simulations of axisymmetric gas flow in conical micronozzles it was found that at throat Reynolds numbers larger than 10, DSMC and continuum methods predicted closer nozzle exit thrusts to the experimental data. Pressure, Mach number and temperature contours were predicted by DSMC and continuum methods to be similar in pattern, but different the magnitude and smoothness of distributions. DSMC predicted larger Mach number and temperature near the wall and closer results at throat Reynolds numbers less than 10 where the flow is switching from slip to transitional regimes. A study of propellant gas temperature effect showed that at $P_0 = 1$ Torr, $D_{throat} = 1$ mm, the higher the gas temperature, the larger the thrust is generated.

A Unified Flow Solver that utilizes hybrid approach using deterministic Boltzmann solver for highly non-equilibrium flows at high Knudsen number and continuum (Euler or Navier-Stokes) solvers for low Knudsen numbers was tested and demonstrated for gas flows in microscale. Initial examination showed that a reasonable agreement with the data from open literature was obtained for the micronozzle test case.

4.0 Nomenclature

A_e	Exit Area (m^2)
D_t	Throat Diameter (mm)
D_h	Hydraulic Diameter (mm)
D_e	Exit Diameter (mm)
g	Acceleration of gravity (9.8 m/s^2)
I_{sp}	Specific Impulse (s^{-1})
k	Boltzmann's Constant ($1.38 \times 10^{-23} \text{ J/K}$)
K	Thermal Conductivity ($\text{W/m}\cdot\text{K}$)
Kn	Knudsen Number
L	Characteristic Length (m)
M_e	Mass Flow Rate (Kg/s)
P	Pressure (Pa)
Q	Volume flow rate (m^3/s)
$\text{Re}_{\text{throat}}$	Throat Reynolds Number
T	Temperature (K)
T_n	Nozzle Exit Thrust (N)
ρ	Fluid Density (Kg/m^3)
λ	Mean Free Path (m)
μ	Molecular Viscosity ($\text{Kg/m}\cdot\text{s}$)
σ_c	Collision Diameter of the Molecules (m)

5.0 References

Alexeenko, A.A., Levin, D.A., Gimelshein, S.F., Collins, R.J. and Reed, B.D., "Numerical Modeling of Axisymmetric and Three-Dimensional Flows in Microelectromechanical Systems Nozzles," AIAA Journal, Vol. 40, No.5, pp. 897-904, 2002.

Arkilic, E.B., Schmidt, M.A., and Breuer, K.S., "Gaseous slip flow in long microchannels," Journal of Microelectromechanical System, 6, 167-178, 1997.

Ayon, A.A., Bayt, R.L., and Breuer, K.S., Deep reactive ion etching: a promising technology for micro- and nanosatellites, *Smart Materials and Structures*, 10, 1135–1144, 2001.

Bayt, R. L., "Analysis, Fabrication and Testing of a MEMS-Based Micro propulsion system," Ph D.Dissertation, Dept.of Aeronautics and Astronautics, MIT, Cambridge, MA, June 1999.

Beskok, A., and Karniadakis, G. E., A model for flows in channels, pipes, and ducts at micro and nano scales, *Microscale Thermophysical Engineering*, 3, 43-77, 1999.

Bird, G.A., *Molecular Gas Dynamics*, Oxford University Press, London, 1976.

Boyd, I.D., Penko, P.F., Meissner, D.L. and DeWitt, K.J., "Experimental and Numerical Investigations of Low-Density Nozzle and Plume Flows of Nitrogen," *AIAA Journal*, Vol. 30, No.10, pp. 2453-2461, 1992.

Boyd, I.D., Jafry, Y. and Beukel, J.V., "Particle Simulations of Helium Microthruster Flows," *Journal of Spacecraft and Rockets*, Vol. 31, No.2, pp. 271-277, 1994.

Chen, C.S., "Numerical method for predicting three-dimensional steady compressible flow in long microchannels," *Journal of Micromechanics & Microengineering*, 14, 1091-1100, 2004.

Chen C.S., Lee S.M. and Sheu S.D. "Numerical analysis of gas flow in microchannels," *Numerical Heat Transfer, A33*, 749-762, 1998.

Chung, C.H., Kim, S.C., Stubbs, R.M., De Witt, K.J., "Low Density Nozzle Flow by Direct Simulation Monte Carlo and Continuum Methods." J of Propulsion and Power, Vol.10, No.1, pp.64-70, 1995.

Fielding, J., Long, M.B., Fielding, G., and Komiya, M., "Systematic errors in optical-flow velocimetry for turbulent flows and flames," Applied Optics, 40(6), 757-764, 2001.

Gad-el-Hak, M., The fluid mechanics of microdevices: the Freeman Scholar Lecture, J. Fluids Mechanics, 121, 5-33, 1998.

Gendrich, C.P. and Koochesfahani, M.M., "Spatial correlation technique for estimating velocity fields using molecular tagging velocimetry (MTV)," Experiments in Fluids 22.1 (1996): 67-77.

Hsieh, S.S., Tsai, H.H., Lin, C.Y., Huang, C.F., and Chien, C.M., "Gas flow in long microchannels," International Journal of Heat and Mass Transfer, 47, 3877-3887, 2004.

Ivanov, M.S., Markelov, G.N., Ketsdever, A.D., Wadsworth, D.C., "Numerical Study of Cold Gas Micronozzle Flows," AIAA 99-0166, 1999.

Jamison, A.J., Ketsdever, A.D., "Low Reynolds Number Performance Comparison of an under expanded Orifice and a DeLaval Nozzle." Rarefied Gas Dynamics: 23rd International Symposium (2003): 557-564.

Kato, S., and Fujimoto, T., A laser-induced fluorescence approach to measurement of physical properties in micro-scale heat and fluid flows, 3rd ASME/JSME Joint Thermal Engineering Conference, vol. 4, 153-158, 1991.

Koplik, J., and Banavar, J. R., Continuum deductions from molecular hydrodynamics, Annual Review of Fluid Mechanics, 27, 257-292, 1995.

Lempert, W.R., Jiang, N., Sethuram, S., and Samimy, M., Molecular tagging velocimetry measurements in supersonic microjets, AIAA Journal 40(6), 1065-1070, 2002.

Markelov, G.N. and Ivanov, M.S., "Numerical Study of 2D/3D Micronozzle Flows," Rarefied Gas Dynamics: 22th International Symposium, pp.539-546, 2001.

Maynes, D., and Webb, A.R., Velocity profile characterization in sub-millimeter diameter tubes using molecular tagging velocimetry, Experiments in Fluids, 32(1), 3-15, 2002.

Meinhart, C.D., Wereley, S.T., and Santiago J.G., PIV measurements of a microchannel flow, Experiments in Fluids, 27, 414–419, 1999.

Mo, H.L., Ye, C.M., Gadepalli, V.V., and Lin, C.X., "Numerical modeling of gas flow in square microchannels," Proceedings of Third International Conference on Microchannnels and Minichannels, ICMM2005 – 75047, Toronto, Ontario, Canada, 2005.

Mohamed, G. H., "The Fluid Mechanics of Microdevices - the Freeman Scholar Lecture," Journal of Fluids Engineering, Vol. 121, 1999, pp. 5-33.

Paul, P.H., Gargulio, M.G., and Rakestraw, D.J., Imaging of pressure- and electrokinetically-driven flows through open capillaries, *Analytical Chemistry*, 70, 2459-2467, 1998.

Rothe, D.E., " Electron beam studies of viscous flow in supersonic nozzle." *AIAA Journal*, 9 (5) (1971): 804-810.

Shah, R.K., and Bhatti, M.S., "Laminar Convective Heat Transfer in Ducts," in *Handbook of Single-Phase Convective Heat Transfer*, eds. Kakac, S., Shah, R.K., and Aung, W., Wiley-Interscience, New York (1987).

Shah, R.K., and London, A.L., "Laminar Flow Forced Convection in Ducts," Supplement 1 to *Advances in Heat Transfer*, Academic, New York (1978).

Simek, O., and Hadjiconstantinou, N. G., Slip-flow constant-wall-temperature Nusselt number in circular tubes in the presence of axial heat conduction, ASME International Mechanical Engineering Congress and Exposition, New York, November 11-16, paper HTD-24106, 2001.

Thompson, B.R., Maynes, D., and Webb, B.W., Micro-scale velocity measurements using molecular tagging velocimetry: methodology and uncertainty, *Proceedings of ASME Joint U.S.-European Fluids Engineering Conference*, Print, Vol. 2, Symposia and General Papers (A and B), Fluids Engineering Division, vol. 257-2, pp. 123-133, 2002.

Wereley, S.T., Gui, L., and Meinhart, C.D., Advanced algorithms for microscale particle image velocimetry, AIAA Journal, 40(6), 1047-1055, 2002.

White, F.M., "Viscous fluid flow," McGraw-Hill, Inc. New York, 1974.

Zheng, Q. and Klewicki, J. C., "Fast data reduction algorithm for molecular tagging velocimetry: The decoupled spatial correlation technique," Measurement Science and Technology, 11(9) (2000): 1282-1288.

6.0 Appendix

Table 8. Experimental data and correlation predictions for N₂ flow in a square microchannel (see Figure 4).

P _{in} , torr	P _{out} , torr	Q, sccm	dP, torr	dP _{corr Dh=500μm} , torr	dP _{corr Dh=550μm} , torr
16.80556	12.13773	14.68102	4.66782	9.067	6.193
27.717	20.87664	26.96391	6.84036	10.38	7.09
36.80702	28.36647	39.50738	8.44056	11.771	8.04
44.55369	34.73196	50.86811	9.82173	12.827	8.761
51.96964	40.94871	62.70616	11.02093	13.893	9.489
59.20849	46.93731	76.39973	12.27118	15.275	10.433
66.29013	52.94336	88.76407	13.34678	16.243	11.094
73.11198	58.62907	100.6728	14.48291	17.091	11.673
79.49758	64.0252	113.57422	15.47238	18.134	12.386
85.92691	69.4262	125.21704	16.50071	18.497	12.634
92.1764	74.68936	137.02256	17.48704	18.868	12.887
98.85651	80.28471	148.65989	18.5718	19.088	13.037

Table 9. Velocity profile near microchannel exit obtained by MTV technique (P_{in} = 92 torr, P_{amb} = 62 torr, see Figure 15).

Distance, μm	V, m/s
-292	80.92
-219	62.24
-146	37.35
-73	59.13
0	96.48
73	93.36
146	46.68
219	24.9
292	80.92

Table 10. Fluorescence intensity of initially written lines as a function of pressure in the test cell (See Figure 16).

P _{cell} , torr	LIF intensity
12.1	2
23.7	3
35.7	5
50.2	8
67.7	11
75.9	12
96.2	15

Table 11. N₂ mass flow rate through the 100 μm throat width micronozzle (see Figure 18).

P _{in} , psi	Q _{m in} , kg/s	Q _{m out} , kg/s	Error Q _{m in} , kg/s	Error Q _{m out} , kg/s
2.80666	6.929E-8	8.333E-8	1.942E-8	1.942E-8
8.79558	1.84E-7	1.667E-7	1.942E-8	1.942E-8
12.00444	2.43E-7	2.083E-7	1.942E-8	1.942E-8
14.87842	2.697E-7	2.5E-7	1.942E-8	1.942E-8
18.11976	3.201E-7	2.917E-7	1.942E-8	1.942E-8
21.1042	3.544E-7	3.333E-7	1.942E-8	1.942E-8
24.00094	3.883E-7	3.542E-7	1.942E-8	1.942E-8
26.89764	4.12E-7	3.958E-7	1.942E-8	1.942E-8
30.05596	4.735E-7	4.375E-7	1.942E-8	1.942E-8
33.02218	5.144E-7	4.583E-7	1.942E-8	1.942E-8
35.9765	5.276E-7	5E-7	1.942E-8	1.942E-8
38.83834	5.772E-7	5.417E-7	1.942E-8	1.942E-8

Table 12. Nozzle exit thrust: comparison of experimental data with continuum Navier-Stokes solution with slip and no-slip boundary conditions (see Figure 22).

Re_{throat}	Exit Thrust (T_n), N				
	Expt	Slip, no press. comp	No-slip, no press. comp	Slip, with press. comp	No-slip, with press. comp
0.1648353	4.54E-07	1.06389E-07	1.12807E-07	4.91254E-05	4.91318E-05
0.2197804	8.82E-07	1.79329E-07	1.90828E-07	4.91987E-05	4.92110E-05
0.3846155	2.01E-06	4.85461E-07	5.10002E-07	4.95075E-05	4.95331E-05
0.5494507	2.76E-06	8.97384E-07	9.37582E-07	4.99219E-05	4.99633E-05
0.7692309	4.45E-06	1.57842E-06	1.64526E-06	5.06056E-05	5.06739E-05
1.043956	6.45E-06	2.61363E-06	2.71020E-06	5.16453E-05	5.17421E-05
2.637363	1.72E-05	1.14733E-05	1.18251E-05	6.05172E-05	6.08740E-05
5.164835	3.92E-05	3.24186E-05	3.29897E-05	8.14811E-05	8.20540E-05
7.582418	6.67E-05	5.73122E-05	5.82437E-05	1.06387E-04	1.07319E-04
10.93407	1.13E-04	9.69756E-05	9.91597E-05	1.46046E-04	1.48246E-04
14.45055	1.69E-04	1.44584E-04	1.48100E-04	1.93658E-04	1.97190E-04
18.07692	2.32E-04	1.94417E-04	1.96718E-04	2.44574E-04	2.68739E-04
22.69231	3.19E-04	2.57116E-04	2.60746E-04	3.35296E-04	3.76755E-04

Table 13. The longitudinal pressure distribution for nitrogen at PR = 2.708 (See Figure 30).

Experimental (Arkillic, 1997)		Numerical Compress. (Chen, 2004)		Analyt. Incompr. (Arkillic, 1997)		Numerical Compress. Present study	
x/L	P/P_{out}	x/L	P/P_{out}	x/L	P/P_{out}	x/L	P/P_{out}
6.52E-09	2.7142	6.52E-09	2.7142	6.52E-09	2.7142	6.52E-09	2.714189
0.1344262	2.584232	0.09836067	2.578043	1	1	0.06985247	2.647551
0.3704918	2.262435	0.1344262	2.534725			0.09936067	2.598043
0.6	1.860188	0.1967213	2.460464			0.1354262	2.554725
0.8295082	1.433188	0.2327869	2.404768			0.1682131	2.517594
		0.2655738	2.355261			0.1977213	2.480464
		0.2983607	2.31813			0.2337869	2.424768
		0.3344262	2.262435			0.2665738	2.375261
		0.4	2.169609			0.2993607	2.33813
		0.4360656	2.113913			0.3354262	2.282435
		0.4655738	2.064406			0.3682131	2.239116
		0.5016394	2.00871			0.401	2.189609
		0.5311475	1.959203			0.4370656	2.133913
		0.6327869	1.785928			0.4665738	2.084406
		0.6655738	1.724044			0.5026394	2.03871
		0.6983607	1.668348			0.5321475	1.989203
		0.7344263	1.587899			0.5682131	1.939696
		0.8032787	1.476507			0.6337869	1.815928
		0.8360656	1.396058			0.6665738	1.754044
		0.8655738	1.334174			0.6993607	1.698348
		0.9344262	1.173275			0.7354263	1.627899
		0.9639344	1.086638			0.7747705	1.578391
		1	1			0.8042787	1.516507
						0.8370656	1.436058
						0.8665738	1.374174
						0.8993607	1.293725
						0.9354262	1.213275
						0.9649344	1.126638
						1	1

Table 14. Normalized friction coefficients comparison (see Figure 31).

$D_h, \mu\text{m}$	C_{IC}^* Numerical	C_{IC}^* From eq. (29)	% Difference
1	0.622	0.625	0.586
2	0.765	0.769	0.638
10	0.941	0.943	0.124
20	0.969	0.971	0.065
40	0.985	0.985	0.053
50	0.987	0.988	0.044
60	0.989	0.991	0.033
80	0.992	0.993	0.026
100	0.994	0.995	0.022

Table 15. Mass flow rates at various pressure ratios (See Figure 33).

P_{in}/P_{out}	Mass Flow Rate, kg/s		
	Compressible Slip flow	Compressible No-slip	Incompressible No-slip
1.5	2.93564E-13	1.91068E-13	1.52843E-13
2	6.67737E-13	4.58537E-13	3.05742E-13
2.5	1.12066E-12	8.02481E-13	4.58621E-13
3	1.65130E-12	1.22287E-12	6.29309E-13
3.5	2.58108E-12	1.71934E-12	7.64255E-13
4	2.94287E-12	2.29230E-12	9.17130E-13
4.5	3.70404E-12	2.94126E-12	1.06999E-12
5	4.54195E-12	3.66662E-12	1.22277E-12

Table 16. Average Knudsen number with varying pressure ratio (See Figure 35).

P_{in}/P_{out}	Average Kn number		
	Compressible Slip flow	Compressible No-slip	Incompressible No-slip
1.5	4.45E-02	0.044751	0.061373
2	3.48E-02	0.034909	0.061373
2.5	2.85E-02	0.028508	0.061373
3	2.41E-02	0.024046	0.061373
3.5	2.09E-02	0.020772	0.061373
4	1.84E-02	0.018271	0.061373
4.5	1.64E-02	0.016302	0.061373
5	1.48E-02	0.014712	0.061373

Table 17. Average Mach number with varying pressure ratio (See Figure 36).

P_{in}/P_{out}	Average Mach number		
	Compressible Slip flow	Compressible No-slip	Incompressible No-slip
1.5	0.002533	0.001927	0.002093
2	0.004664	0.003665	0.004186
2.5	0.006599	0.005316	0.006279
3	0.008421	0.006917	0.008626
3.5	0.010168	0.008488	0.010463
4	0.011868	0.01004	0.012556
4.5	0.013531	0.011578	0.014648
5	0.015168	0.013107	0.01674

Table 18. C_C^* versus varying pressure ratio, $C_C^* = fRe_{Comp}/fRe_{Incomp}$ (See Figure 37).

P_{in}/P_{out}	$C_C^* = fRe_{Comp}/fRe_{Incomp}$		
	Compressible Slip flow	Compressible No-slip	Incompressible No-slip
1.5	0.693295652	1.074244047	1
2	0.757747981	1.110755759	1
2.5	0.804152495	1.131335386	1
3	0.839292896	1.143927117	1
3.5	0.863271638	1.15194438	1
4	0.889292205	1.157532565	1
4.5	0.908009958	1.161366766	1
5	0.923859309	1.164120215	1

Table 19. Comparison of 2-D and 3-D results for $C_C^* = fRe_{Comp}/fRe_{Incomp}$ (See Figure 44).

P_{in}/P_{out}	$C_C^* = fRe_{Comp}/fRe_{Incomp}$		
	3-D Compressible Slip	3-D Incompressible No-slip	2-D Compressible Slip
1.5	0.693296	1	
2	0.757748	1	0.654161488
2.5	0.804152	1	
3	0.839293	1	0.759835223
3.5	0.863272	1	
4	0.889292	1	0.790601968
4.5	0.90801	1	
5	0.923859	1	0.813153222

Table 20. The 2-D and 3-D flow U –velocity comparison (See Figure 41).

P_{in} / P_{out}	2-D (U m/s)	3-D (U m/s)	% Difference
2.0	6.55	3.79	42.2
3.0	14.89	9.01	39.49
4.0	26.50	16.12	39.17
5.0	40.81	24.24	40.61

Table 21. Nozzle exit thrust: comparison of DSMC, experiments, and Navier-Stokes solution (see Figure 54).

Re_{throat}	Exit Thrust (T_n), N			
	Experiment	DSMC	NS, slip $T_n = MV$	NS, slip $T_n = MV + PA$
0.16	4.54E-07	2.38E-06	1.07E-07	4.91E-05
0.22	8.82E-07	3.21E-06	1.83E-07	4.92E-05
0.38	2.01E-06	5.73E-06	4.99E-07	4.95E-05
0.55	2.76E-06	7.99E-06	9.00E-07	4.99E-05
0.77	4.45E-06	1.13E-05	1.56E-06	5.06E-05
1.04	6.45E-06	1.53E-05	2.62E-06	5.17E-05
2.64	1.72E-05	3.97E-05	1.15E-05	6.06E-05
5.16	3.92E-05	7.86E-05	3.19E-05	8.09E-05
7.58	6.67E-05	1.15E-04	5.65E-05	1.06E-04
10.93	1.13E-04	1.66E-04	9.52E-05	1.44E-04
14.45	1.69E-04	2.19E-04	1.42E-04	1.91E-04
18.08	2.32E-04	2.90E-04	1.93E-04	2.45E-04
22.69	3.19E-04	3.54E-04	2.55E-04	3.36E-04

Table 22. DSMC simulation results for the effect of the inlet temperature of the propellant gas at $P_0 = 1$ Torr, $D_{throat} = 1$ mm (see Figure 56).

Re_{throat}	T_n , N	
	$T_0 = 300$ K	$T_0 = 1300$ K
5	7.61E-05	0.000226
10	0.000153	0.000461
20	0.00031	0.000939
50	0.000776	0.002992
100	0.001605	0.005945

Table 23. MatLab Image Correlation Velocimetry script.

```
% ncc-normxcorr2/image crop/x-y SW size/x-y max distance/x-y overlap/
% parameters: swx,swy,dxlm,dxrm,dytm,dybm,lapx,lapy,tresh,cropimg,maporfig
% 19 Jan 2005
% Author: Ali K. Reyhanogullari
clc;

%%%% CONSTANT DEFINITIONS
% display preferences
version = 'ICVncc23'; qscale = 0.75; disp_opt = 3;
xmmstep = 100; ymmstep = 50;
% area to be processed
topc = 0.3; bottomc = 0.7; leftc = 0.00; rightc = 1.00;
% sample vector value
sampleval = [20.0 0.0];

%%%% PRE-PROCESSING
% extract raw image pair and experiment data from dataset
img1 = FMInput{1,2}.Img.Img1;
img2 = FMInput{1,2}.Img.Img2;
% experimental setup parameters
dt = FMInput{1,1}.TimeBtwPulses;
sfactor = FMInput{1,1}.CameraSetup.ScaleFactor;
pxpitch = FMInput{1,1}.CameraSetup.PxPitch;
% extract parameters
params = str2num(ParamStr);
swx = params(1);
swy = params(2);
dxlm = params(3);
dxrm = params(4);
dytm = params(5);
dybm = params(6);
lapx = params(7);
lapy = params(8);
tresh = params(9);
cropimg = params(10);
maporfig = params(11);

% raw image width and height in pixels
[n,m] = size(img1);
% if desired, crop raw image to process only a portion
if (cropimg == 1)
    img1 = imcrop(img1,[leftc*m topc*n (rightc-leftc)*m (bottomc-topc)*n]);
    img2 = imcrop(img2,[leftc*m topc*n (rightc-leftc)*m (bottomc-topc)*n]);
end
% updated image width and height in pixels
[nc,mc] = size(img1);

% image dimensions in mm for display
xmmloc = [0:xmmstep:mc]';
ymmloc = [0:ymmstep:nc]';
xmm = num2str(round(xmmloc*pxpitch(1)*sfactor*1e+5)*1e-2);
ymm = num2str(round(ymmloc*pxpitch(2)*sfactor*1e+5)*1e-2);

%%%% IMAGE ENHANCEMENT
% contrast scaling
img1 = double(img1);
img2 = double(img2);
% find minimum and maximum pixel values
```

```

a = min(img1(:));
b = max(img1(:));
% rescale image matrix according to these values, resulting pixel values
% might be floating numbers and should be converted to integers
if (b < 256)
    imgtype = '8-bit';
    img1 = uint8(255/(b-a)*(img1-a));
    img2 = uint8(255/(b-a)*(img2-a));
elseif (b < 65536)
    imgtype = '16-bit';
    img1 = uint16(65535/(b-a)*(img1-a));
    img2 = uint16(65535/(b-a)*(img2-a));
else
    error('Image is not a MATLAB indexed 8 or 16 bit type.');
end

%% NCC FOR EACH INTERROGATION WINDOW (SW)
tic;
% number of SWs in x and y direction of image including overlaps
lapx = floor(lapx*swx);
lapy = floor(lapy*swy);
nswx = floor((mc-(dxlm+dxrm)-lapx)/(swx-lapx));
nswy = floor((nc-(dytm+dybm)-lapy)/(swy-lapy));
sx = floor((mc-(dxlm+dxrm)-(nswx*swx-(nswx-1)*lapx))/2);
sy = floor((nc-(dytm+dybm)-(nswy*swy-(nswy-1)*lapy))/2);
threshav = 0;
for i=1:nswy

    % upper edge of current SW
    yssw = sy+dytm+1+(i-1)*swy-(i-1)*lapy;

    for j=1:nswx

        % left edge of current SW
        xssw = sx+dxlm+1+(j-1)*swx-(j-1)*lapx;

        % crop current SW and RW
        SW = imcrop(img1,[xssw yssw (swx-1) (swy-1)]);
        RW = imcrop(img2,[xssw-dxlm yssw-dytm (dxlm+swx-1+dxrm) ...
            (dytm+swy-1+dybm)]);
        NCC = normxcorr2(SW,RW);
        % since normxcorr2 gives "extrapolated" coefficients, discard them
        NCC = imcrop(NCC,[swx swy (dxlm+dxrm) (dytm+dybm)]);

        [NCCmax,iNCCmax] = max(NCC(:));
        % assign shift values, assign NaN if no satisfactory correlation
        if (NCCmax > thresh)
            [yNCCmax,xNCCmax] = ind2sub(size(NCC),iNCCmax(1));
            xshift(i,j) = xNCCmax-(dxlm+1);
            yshift(i,j) = yNCCmax-(dytm+1);
        else
            xshift(i,j) = 0;
            yshift(i,j) = 0;
        end

        % position for these vectors
        xpos(i,j) = xssw - 1 + floor(swx/2);
        ypos(i,j) = yssw - 1 + floor(swy/2);

        % velocities in m/sec calculated using delta_t, pixel_pitch and
        % scale_factor
    end
end

```

```

U(i,j) = (xshift(i,j)*pxpitch(1))*sfactor/dt;
V(i,j) = (yshift(i,j)*pxpitch(2))*sfactor/dt;
treshav = treshav+NCCmax;
end
end

toc1 = toc;
treshav = treshav/(nswx*nswy);
Uav = sum(sum(U))/(nswx*nswy);

%% SEND RESULTS TO FLOWMANAGER
if (maporfig == 0)
    format compact;
    disp('Analysis with: '); disp(version); disp(' ');
    % flip vector map vertically
    % RECALL: FlowManager takes bottom of the image as the vertical 0
    % whereas MATLAB takes it as the top of the image)
    ypos = nc-ypos;
    V = -V;
    FMOutVector(xpos,ypos,U,V);
    treshav
    % nswx,nswy,Uav,Vav,treshav,delta_t,scale_factor,pixel_pitch
else
    % clear any previous figure
    clf;
    % color schemes
    if (disp_opt == 0)
        map = 'white'; color = 'b';
    elseif (disp_opt == 1)
        map = 'bone'; color = 'c';
    elseif (disp_opt == 2)
        map = 'summer'; color = 'k';
    else
        map = 'jet'; color = 'r';
    end

    cap = 'Analysis with %s: %s Vector Map [%dx%d] found in %4.2fs.';
    info = 'swx=%d swy=%d dxlm=%d dxrm=%d dytm=%d dybm=%d';
    info = strcat(info, ' lapx=%d lapy=%d thresh=%1.2f');
    info = strcat(info, ' Uav=%2.2fm/s treshav=%1.2f SF=%1.4f dt=%1.2e');
    % sample vector
    U(1,nswx) = sampleval(1); V(1,nswx) = sampleval(2);
    sample = ' %2.2f m/s \n';
    sample = sprintf(sample,sqrt(sampleval(1)^2+sampleval(2)^2));
    hfigure = figure(1);
    set(hfigure,'Visible','off');
    cap = sprintf(cap,version, ' ',nswx,nswy,to1);
    info = sprintf(info,swx,swy,dxlm,dxrm,dytm,dybm,lapx,lapy,thresh, ...
        Uav,treshav,sfactor,dt);
    imshow(img2); colormap(map);
    hold on; grid on; axis on;
    text(xmmloc-mc*0.015,nc*1.12*ones(size(xmmloc,1),1),xmm);
    text(-mc*0.10*ones(size(ymmloc,1),1),ymmloc,ymm);
    text(-mc*0.10,-nc*0.06,'mm'); text(-mc*0.04,-nc*0.06,'pixel');
    text(mc*1.015,nc*1.12,'mm'); text(mc*1.015,nc*1.06,'pixel');
    hquiver = quiver(xpos,ypos,U,V,qscale,color);
    set(hquiver,'LineWidth',1.4);
    htext = text(xpos(1,nswx),ypos(1,nswx)*0.90,sample);
    set(htext,'EdgeColor','k','Color','k','Margin',nc*0.01);
    title(cap); text(0,nc*1.18,info);
    plot(xpos(1,nswx),ypos(1,nswx),'g.','LineWidth',5);

```

```
hold off;
FMOutPicture;
end

%% clear variables created after exporting them to FlowManager
clear variables;
```